

Master Thesis

CFD Tool VSPAERO: Actuator Disk and Flow Visualization

Author: Maruxa Bayón Fernández

Supervisor: Prof. Dr.-Ing. Dieter Scholz, MSME

Submitted: 2023-10-20

*Faculty of Engineering and Computer Science
Department of Automotive and Aeronautical Engineering*

DOI:

<https://doi.org/10.15488/xxxxx>

URN:

<https://nbn-resolving.org/urn:nbn:de:gbv:18302-aero2023-10-20.015>

Associated URLs:

<https://nbn-resolving.org/html/urn:nbn:de:gbv:18302-aero2023-10-20.015>

© This work is protected by copyright

The work is licensed under a Creative Commons Attribution-NonCommercial-ShareAlike 4.0 International License: CC BY-NC-SA

<https://creativecommons.org/licenses/by-nc-sa/4.0>



Any further request may be directed to:

Prof. Dr.-Ing. Dieter Scholz, MSME

E-Mail see: <http://www.ProfScholz.de>

This work is part of:

Digital Library - Projects & Theses - Prof. Dr. Scholz

<http://library.ProfScholz.de>

Published by

Aircraft Design and Systems Group (AERO)

Department of Automotive and Aeronautical Engineering

Hamburg University of Applied Science

This report is deposited and archived:

- Deutsche Nationalbibliothek (<https://www.dnb.de>)
- Repository of Leibniz University Hannover (<https://www.repo.uni-hannover.de>)
- Internet Archive (<https://archive.org>)
Item: <https://archive.org/details/TextBayonFernandez.pdf>

This report has associated published data in Harvard Dataverse:

<https://doi.org/10.7910/DVN/HFCSQZ>

Abstract

Purpose – To show how VSPAERO as part of OpenVSP from NASA can be set up to visualize and analyze the flow around passenger aircraft lifting surfaces combined with jet engines. The actuator disk inside a duct is used to model this aero-propulsive interaction.

Methodology – Aerodynamic results obtained with VSPAERO for wing and tail are compared, considering different engine positions.

Findings – VSPAERO offers reliable results if the simulation is set up with care. The user must always keep an eye on model discretization and refinement, flow conditions, and actuator disk parameters. Depending on the purpose of the analysis, only a disk or rather a combination of a disk with a duct can be used. The combination of a disk with a duct shows the influence of jet engines on lifting surfaces in a more realistic way and improves the results of the calculation. Jet engines mounted on the wing disturb the flow around the wing. If engines would be mounted on the wing tip, their detrimental aerodynamic interference with the wing could be limited.

Research Limitations – To use the actuator disk to model propellers is difficult. No attempt has been made to show this in this thesis.

Practical Implications – VSPAERO can be used with ease, but substantial time is needed to get familiar with the program, although online help is available. This thesis may shorten the time to get results from calculations using the actuator disk to model jet engines in VSPAERO.

Originality – This thesis contributes to the didactics of integrating jet engines into VSPAERO. Results obtained for jet engine positions on an Airbus A320 geometry only illustrate the approach. Engine integration is multidisciplinary and not a question of aerodynamics alone.

CFD Tool VSPAERO: Actuator Disk and Flow Visualization

Task for a Master Thesis

Background

Conceptual aircraft design calculates approximately 50 fundamental parameters for the aircraft. To obtain a 3D representation of such a geometry, OpenVSP (<https://openVSP.org>) can be used. OpenVSP-Connect (<http://openVSP.Profscholz.de>) helps, converting the calculated design parameters into an OpenVSP model. OpenVSP is bundled with VSPAERO, which offers aerodynamic analysis capabilities using the Vortex Lattice Method (VLM) and the Panel Method. VSPAERO incorporates actuator disks that can be employed to include jets or propellers into the aerodynamic model. VSPAERO provides possibilities for visualization of results. For example, wakes and pressure coefficient changes can be displayed. In his [thesis](#), Floris Märien combines testing of VSPAERO with providing help to get started with the program. Real world aerodynamic questions are answered in example problems. The idea for this thesis is to continue along this path.

Task

Show how to use the actuator disk to integrate jets into aerodynamic analysis and flow visualization. Here are the detailed tasks:

- Literature review of the software OpenVSP.
- Literature review of the aerodynamic fundamentals of VSPAERO.
- Literature review of the actuator disk theory.
- Discretization studies to determine the balance between correct and reliable results and short simulation time.
- Discretization studies to determine the best disk parameters for aircraft jet engines.
- Comparison of aerodynamic results for different engine locations.
- Selection of the best engine location based on preliminary aerodynamic results only, using the Airbus A320 geometry as an example.

The report has to be written in English based on German or international standards on report writing.

Table of Contents

List of Figures	12
List of Tables	13
List of Symbols	14
List of Abbreviations	16
1 Introduction	17
1.1 Motivation	17
1.2 Title Terminology	17
1.3 Objectives	18
1.4 Previous Research	19
1.5 Structure of the Work	19
2 OpenVSP	20
2.1 History	20
2.2 OpenVSP Features	21
2.2.1 User Interface and Geometry Modelling	21
2.2.2 Analysis Tools	22
2.2.3 Compatibility	22
2.3 OpenVSP Tools	24
2.3.1 Hangar	24
2.3.2 Ground School and Workshops	24
2.3.3 Google Group	25
2.4 VSPAero	25
3 Theoretical Background	26
3.1 Aerodynamic Fundamentals	26
3.1.1 Potential Flow	26
3.1.2 Boundary Conditions	27
3.1.3 Biot-Savart Law	28
3.2 VLM and Panel Method	30
3.3 Actuator Disk	31
4 Simulation Settings	33
4.1 Geometry	33
4.1.1 Wing Geometry	33
4.1.2 Tail Geometry	35
4.1.3 Duct Geometry	36
4.2 Simulation Parameters	37
4.3 Tessellation	39
4.3.1 Wing Tessellation	40
4.3.2 Tail Tessellation	41
4.3.3 Duct Tessellation	42
4.4 Clustering	43
4.4.1 Wing and Tail Clustering	44
4.4.2 Duct Clustering	47
4.5 Disk Analysis	48

4.5.1	Performance and Design Parameters	48
4.5.2	Aerodynamic Analysis	49
5	Results	54
5.1	Base Case	54
5.2	Engines Above	58
5.3	More Engines	63
5.4	Tip Engines	69
5.5	A320	76
5.6	Best Distribution	80
6	Discussion	89
7	Summary and Conclusions	90
7.1	Summary	90
7.2	Conclusions	90
8	Recommendations	92
	List of References	93
	Appendix A - Graphical representations of the non-interpolated results	98

List of Figures

Figure 2.1	OpenVSP timeline (McDonald 2021).	21
Figure 2.2	OpenVSP Hangar (OpenVSPc).	24
Figure 3.1	Typical functions in a computational aerodynamics system (Liu 2007).	26
Figure 3.2	Decomposition of a general airfoil at certain incidence (Liu 2007).	27
Figure 3.3	Point vortex flow (Liu 2007).	28
Figure 3.4	Three dimensional vortex filament (Liu 2007).	29
Figure 3.5	Schematic of a lifting surface with horseshoe vortices (Anderson 1984).	30
Figure 3.6	Actuator disk diagram (Spalart 2003).	32
Figure 4.1	A320 wing geometry.	33
Figure 4.2	A320 tail geometry.	35
Figure 4.3	Cross section of the A320 ducts.	36
Figure 4.4	A320 ducts geometry.	37
Figure 4.5	"Overview" section of VSPAero.	37
Figure 4.6	"Advanced" section of VSPAero.	38
Figure 4.7	"Disk" section of VSPAero.	39
Figure 4.8	Tessellation examples in OpenVSP (Litherland 2021).	39
Figure 4.9	Final Wing Tessellation.	41
Figure 4.10	Final tail tessellation.	42
Figure 4.11	Final duct tessellation.	43
Figure 4.12	Chord wise clusterings of the wing. From top to bottom: LE = 0.25, TE = 0.25; LE = 0.25, TE = 1.00.	44
Figure 4.13	Span wise clusterings of the wing. From top to bottom: RT = 1.00, MID = 1.00, TIP = 1.00; RT = 1.00, MID = 1.00, TIP = 0.25; RT = 1.00, MID = 0.50, TIP = 0.25; RT = 1.00, MID = 0.25, TIP = 0.25.	46
Figure 4.14	Final clustering of the tail.	47
Figure 4.15	Chord wise clusterings of the ducts. From left to right: LE = 0.25, TE = 1.00; LE = 0.25, TE = 0.50; LE = 0.25, TE = 0.25.	47
Figure 4.16	Disk configurations for the One Disk analysis.	49
Figure 4.17	Aerodynamic results of the One Disk analysis with the disks in the front.	50
Figure 4.18	Aerodynamic results of the One Disk analysis with the disks in the back.	50
Figure 4.19	Disk configurations for the Two Disks analysis.	51
Figure 4.20	Aerodynamic results of the Two Disks analysis with both of the disks rotating in inwards up direction.	51
Figure 4.21	Aerodynamic results of the Two Disks analysis with the front disk rotating in inwards up direction and the back disk rotating in outwards up direction.	51
Figure 4.22	Aerodynamic results of the Two Disks analysis with the front disk rotating in outwards up direction and the back disk rotating in inwards up direction.	52

Figure 4.23	Aerodynamic results of the One Disk analysis with the disk in the front and the Two Disks analysis with the first disk rotating in outwards up direction and the second rotating in inwards up direction with isometric perspective.	52
Figure 4.24	Aerodynamic results of the One Disk analysis with the disk in the front and the Two Disks analysis with the first disk rotating in outwards up direction and the second rotating in inwards up direction with rear perspective.	53
Figure 5.1	A320 wing geometry.	54
Figure 5.2	Base Case geometries. From left to right: wing & disks case and wing, disks & ducts case.	55
Figure 5.3	Graphical representation of the drag coefficient results of the Base Case.	55
Figure 5.4	Graphical representation of the lift coefficient results of the Base Case.	56
Figure 5.5	Graphical representation of the pressure coefficient results of the Base Case.	57
Figure 5.6	Base Case aerodynamic results for the wing case.	57
Figure 5.7	Base Case aerodynamic results for the disks & wing case. . .	58
Figure 5.8	Base Case aerodynamic results for the disks, ducts & wing case.	58
Figure 5.9	VFW 614 (Jonsson 2000).	59
Figure 5.10	Engines Above geometries. From left to right: wing & disks case and wing, disks & ducts case.	59
Figure 5.11	Graphical representation of the drag coefficient results of the Engines Above for the disks & wing case.	60
Figure 5.12	Graphical representation of the drag coefficient results of the Engines Above for the disks, ducts & wing case.	60
Figure 5.13	Graphical representation of the lift coefficient results of the Engines Above for the disks & wing case.	61
Figure 5.14	Graphical representation of the lift coefficient results of the Engines Above for the disks, ducts & wing case.	61
Figure 5.15	Graphical representation of the pressure coefficient results of the Engines Above for the disks & wing case.	62
Figure 5.16	Graphical representation of the pressure coefficient results of the Engines Above for the disks, ducts & wing case.	62
Figure 5.17	Engines Above aerodynamic results for the disks & wing case.	63
Figure 5.18	Engines Above aerodynamic results for the disks, ducts & wing case.	63
Figure 5.19	From Left to Right: Airbus A380 (Modla 2023) & Antonov An-225 Mriya (Steven 2012).	64
Figure 5.20	Four engines geometries. From left to right: wing & disks case and wing, disks & ducts case.	64
Figure 5.21	Six engines geometries. From left to right: wing & disks case and wing, disks & ducts case.	65
Figure 5.22	Graphical representation of the drag coefficient results of the More Engines distributions for the disks & wing case. . .	65

Figure 5.23	Graphical representation of the drag coefficient results of the More Engines distributions for the disks, ducts & wing case.	66
Figure 5.24	Graphical representation of the lift coefficient results of the More Engines distributions for the disks & wing case.	66
Figure 5.25	Graphical representation of the lift coefficient results of the More Engines distributions for the disks, ducts & wing case.	67
Figure 5.26	Graphical representation of the pressure coefficient results of the More Engines distributions for the disks & wing case.	67
Figure 5.27	Graphical representation of the pressure coefficient results of the More Engines distributions for the disks, ducts & wing case.	68
Figure 5.28	Four engines aerodynamic results for the disks & wing case.	68
Figure 5.29	Four engines aerodynamic results for the disks, ducts & wing case.	68
Figure 5.30	Six engines aerodynamic results for the disks & wing case.	69
Figure 5.31	Six engines aerodynamic results for the disks, ducts & wing case.	69
Figure 5.32	From Left to Right: SNCASO SO.9000 Trident (Turner 2012) & Myasishchev M-50 (Wikipedia 2009).	70
Figure 5.33	Engines below the tips geometries. From left to right: wing & disks case and wing, disks & ducts case.	70
Figure 5.34	Engines in front of the tips geometries. From left to right: wing & disks case and wing, disks & ducts case.	71
Figure 5.35	Engines above the tips geometries. From left to right: wing & disks case and wing, disks & ducts case.	71
Figure 5.36	Graphical representation of the drag coefficient results of the Tip Engines distributions for the disks & wing case.	72
Figure 5.37	Graphical representation of the drag coefficient results of the Tip Engines distributions for the disks, ducts & wing case.	72
Figure 5.38	Graphical representation of the lift coefficient results of the Tip Engines distributions for the disks & wing case.	73
Figure 5.39	Graphical representation of the lift coefficient results of the Tip Engines distributions for the disks, ducts & wing case.	73
Figure 5.40	Engines below the tips aerodynamic results for the disks & wing case.	74
Figure 5.41	Engines below the tips aerodynamic results for the disks, ducts & wing case.	74
Figure 5.42	Engines in front of the tips aerodynamic results for the disks & wing case.	75
Figure 5.43	Engines in front of the tips aerodynamic results for the disks, ducts & wing case.	75
Figure 5.44	Engines above the tips aerodynamic results for the disks & wing case.	75
Figure 5.45	Engines above the tips aerodynamic results for the disks, ducts & wing case.	76
Figure 5.46	A320 wing and tail geometries.	76

Figure 5.47	Wing and tail geometries. From left to right: wing disks case and wing, disks ducts case.	77
Figure 5.48	Graphical representation of the drag coefficient results of the tail.	77
Figure 5.49	Graphical representation of the lift coefficient results of the tail.	78
Figure 5.50	Graphical representation of the pressure coefficient results of the tail.	78
Figure 5.51	Wing and tail aerodynamic results.	79
Figure 5.52	Wing and tail aerodynamic results for the disks, ducts & wing case.	79
Figure 5.53	Wing and tail aerodynamic results for the disks, ducts & wing case.	79
Figure 5.54	Engines above the tips and tail geometries. From left to right: wing & disks case and wing, disks & ducts case.	81
Figure 5.55	Engines above and tail geometries. From left to right: wing & disks case and wing, disks & ducts case.	81
Figure 5.56	Graphical representation of the drag coefficient wing results of the Best Results for the disks & wing case.	82
Figure 5.57	Graphical representation of the drag coefficient wing results of the Best Results for the disks, ducts & wing case.	82
Figure 5.58	Graphical representation of the lift coefficient wing results of the Best Results for the disks & wing case.	83
Figure 5.59	Graphical representation of the lift coefficient wing results of the Best Results for the disks, ducts & wing case.	83
Figure 5.60	Graphical representation of the drag coefficient tail results of the Best Results for the disks & wing case.	84
Figure 5.61	Graphical representation of the drag coefficient tail results of the Best Results for the disks, ducts & wing case.	84
Figure 5.62	Graphical representation of the lift coefficient tail results of the Best Results for the disks & wing case.	85
Figure 5.63	Graphical representation of the lift coefficient tail results of the Best Results for the disks, ducts & wing case.	85
Figure 5.64	Graphical representation of the pressure coefficient tail results of the Best Results for the disks & wing case.	86
Figure 5.65	Graphical representation of the pressure coefficient tail results of the Best Results for the disks, ducts & wing case.	86
Figure 5.66	Engines above the tips and tail aerodynamic results for the disks & wing case.	87
Figure 5.67	Engines above the tips and tail aerodynamic results for the disks, ducts & wing case.	87
Figure 5.68	Engines above and tail aerodynamic results for the disks & wing case.	87
Figure 5.69	Engines above and tail aerodynamic results for the disks, ducts & wing case.	88
Figure A.1	Graphical representation of the non-interpolated drag coefficient results of the Base Case.	98

Figure A.2	Graphical representation of the non-interpolated lift coefficient results of the Base Case.	98
Figure A.3	Graphical representation of the non-interpolated pressure coefficient results of the Base Case.	98
Figure A.4	Graphical representation of the non-interpolated drag coefficient results of the Engines Above for the disks & wing case.	99
Figure A.5	Graphical representation of the non-interpolated drag coefficient results of the Engines Above for the disks, ducts & wing case.	99
Figure A.6	Graphical representation of the non-interpolated lift coefficient results of the Engines Above for the disks & wing case.	99
Figure A.7	Graphical representation of the non-interpolated lift coefficient results of the Engines Above for the disks, ducts & wing case.	100
Figure A.8	Graphical representation of the non-interpolated pressure coefficient results of the Engines Above for the disks & wing case.	100
Figure A.9	Graphical representation of the non-interpolated pressure coefficient results of the Engines Above for the disks, ducts & wing case.	100
Figure A.10	Graphical representation of the non-interpolated drag coefficient results of the More Engines distributions for the disks & wing case.	101
Figure A.11	Graphical representation of the non-interpolated drag coefficient results of the More Engines distributions for the disks, ducts & wing case.	101
Figure A.12	Graphical representation of the non-interpolated lift coefficient results of the More Engines distributions for the disks & wing case.	101
Figure A.13	Graphical representation of the non-interpolated lift coefficient results of the More Engines distributions for the disks, ducts & wing case.	102
Figure A.14	Graphical representation of the non-interpolated pressure coefficient results of the More Engines distributions for the disks & wing case.	102
Figure A.15	Graphical representation of the non-interpolated pressure coefficient results of the More Engines distributions for the disks, ducts & wing case.	102
Figure A.16	Graphical representation of the non-interpolated drag coefficient results of the Tip Engines distributions for the disks & wing case.	103
Figure A.17	Graphical representation of the non-interpolated drag coefficient results of the Tip Engines distributions for the disks, ducts & wing case.	103

Figure A.18	Graphical representation of the non-interpolated lift coefficient results of the Tip Engines distributions for the disks & wing case.	103
Figure A.19	Graphical representation of the non-interpolated lift coefficient results of the Tip Engines distributions for the disks, ducts & wing case.	104
Figure A.20	Graphical representation of the non-interpolated drag coefficient results of the tail.	104
Figure A.21	Graphical representation of the non-interpolated lift coefficient results of the tail.	104
Figure A.22	Graphical representation of the non-interpolated pressure coefficient results of the tail.	105
Figure A.23	Graphical representation of the non-interpolated drag coefficient wing results of the Best Results for the disks & wing case.	105
Figure A.24	Graphical representation of the non-interpolated drag coefficient wing results of the Best Results for the disks, ducts & wing case.	105
Figure A.25	Graphical representation of the non-interpolated lift coefficient wing results of the Best Results for the disks & wing case.	106
Figure A.26	Graphical representation of the non-interpolated lift coefficient wing results of the Best Results for the disks, ducts & wing case.	106
Figure A.27	Graphical representation of the non-interpolated drag coefficient tail results of the Best Results for the disks & wing case.	106
Figure A.28	Graphical representation of the non-interpolated drag coefficient tail results of the Best Results for the disks, ducts & wing case.	107
Figure A.29	Graphical representation of the non-interpolated lift coefficient tail results of the Best Results for the disks & wing case.	107
Figure A.30	Graphical representation of the non-interpolated lift coefficient tail results of the Best Results for the disks, ducts & wing case.	107
Figure A.31	Graphical representation of the non-interpolated pressure coefficient tail results of the Best Results for the disks & wing case.	108
Figure A.32	Graphical representation of the non-interpolated pressure coefficient tail results of the Best Results for the disks, ducts & wing case.	108

List of Tables

Table 4.1	General parameters of the wing.	34
Table 4.2	General parameters of the sections of the wing.	34
Table 4.3	Parameters of the horizontal tail.	35
Table 4.4	Parameters of the vertical tail.	36
Table 4.5	Wing tessellation convergence.	41
Table 4.6	Duct tessellation convergence.	43
Table 4.7	Chord wise clustering results of the wing.	45
Table 4.8	Span wise clustering results of the wing.	46
Table 4.9	Clustering results of the ducts.	48

List of Symbols

A	Cross Sectional Area
AR	Wing Aspect Ratio
b	Wing Span
b_p	Projected Wing Span
c	Chord
C_{Di}	Integrated Induced Drag Coefficient
C_{D0}	Skin Friction Drag Coefficient (Estimated parasite drag)
C_{Dtot}	Total Drag Coefficient
C_D	Drag Coefficient
C_L	Lift Coefficient
C_p	Pressure Coefficient
CP	Coefficient of Power
CT	Coefficient of Thrust
D	Diameter of the Disk / Drag
e	Oswald Efficiency Factor (Span Efficiency)
i_w	Incidence Angle of the Wing
J	Advanced Ratio
L	Lift
M	Mach Number
n	Revolutions of the Engine
p	Pressure
Q	Free-stream Velocity
r	Radius
Re_{Cef}	Reynolds Number Along Reference Chord
S_w	Wing Area
T	Thrust
U	Separations Along the Wingspan
V	Velocity
V_{inf}	Freestream Velocity Through the Actuator Disk
W	Separations Along the Chordspan

Greek Symbols

α	Angle of Attack
Γ	Circulation
δ	Differential
Δ	Variation
ε_t	Wing Twist
λ	Taper Ratio
μ	Dynamic Viscosity
ν_w	Dihedral Angle
ξ	Vorticity
ρ	Air density
ϕ	Velocity Potential
φ	Sweep Angle
Φ	Velocity Potential Function
ω_b	Wing's Bound Vortices
ω_i	Wake

Subscripts

$s1$	Section 1
$s2$	Section 2
$Ts1$	Section 1 of the Vertical Tail
$Ts2$	Section 2 of the Vertical Tail
θ	Tangential Component

List of Abbreviations

AFRL	Air Force Research Laboratory
CFD	Computational Fluid Dynamics
eVTOL	Electrical Vertical Take-Off and Landing
FEA	Finite Element Analysis
GUI	Graphical User Interface
LE	Leading Edge
MID	Middle Section
NASA	National Aeronautics and Space Administration
NOSA	NASA Open Source Agreement
OpenVSP	Open Vehicle Sketch Pad
RAM	Rapid Aircraft Modeler
RT	Root
TE	Trailing Edge
TIP	Wingtip
UAV	Unmanned Aerial Vehicle
VLM	Vortex Lattice Method
VSP	Vehicle Sketch Pad

1 Introduction

1.1 Motivation

One of the first steps in the aircraft design process is to assess if the initial proposed characteristics for the initial concept of the project are viable or not. Once the objectives, specifications, and initial conceptual design are defined, it is necessary to perform, among other things, an aerodynamic analysis to evaluate the aircraft's performance. To do this, there is a wide variety of programs that can be used, depending on the type of analysis you want to perform, ranging from programs more focused in airfoil analysis like XFLR5 to more advanced and flexible programs like Matlab/Simulink which requires high knowledge of programming skills.

However, the ideal approach is to find a balance between the simplicity of the program and the accuracy of results within a reasonable computation time. This is where software like OpenVSP comes into play, which allows you to create 3D aircraft models and conduct basic aerodynamic analyzes to estimate parameters such as lift, drag, and stability characteristics within a reasonable computation time.

1.2 Title Terminology

"CFD Tool VSPAERO: Actuator Disk and Flow Visualization"

Flow

The Cambridge Dictionary defines the word *flow* as:

The movement of something in one direction (CUPA 2023a).

This thesis aims to analyze the flow of different Airbus A320 configurations.

Visualization

The Cambridge Dictionary defines the word *visualization* as:

The act or an example of creating an image, etc. to represent something (CUPA 2023c).

The flow of the different Airbus A320 configurations is going to be visualize in order to analyze the differences and possible different final configurations on it's design.

CFD

Wikipedia defines the word *CFD* as:

Computational fluid dynamics (CFD) is a branch of fluid mechanics that uses numerical analysis and data structures to analyze and solve problems that involve fluid flows (Wikipedia 2023d).

To obtain the results of the flow visualization a CFD software is going to be used.

Tool

The Cambridge Dictionary defines the word *tool* as:

Something that helps you to do a particular activity (CUPA 2023b).

Different types of tools are going to be used to analyze the different Airbus A320 configurations.

VSPAero

The OpenVSP website defines the word *VSPAero* as:

A fast, linear, vortex lattice solver which integrates actuator disks that can be accurately and easily described for aero-propulsive analysis (OpenVSP 2015).

This is the software that is going to be used for all of the analysis, testing how different tools of the program affects the final aerodynamic results.

1.3 Objectives

The main purpose of this thesis is to learn how to design and simulate different engine positions on the wing of the Airbus A320 using the software tools OpenVSP and VSPAero. This analysis will involve exploring the functionality of various tools within the programs to better understand their capabilities.

To achieve this, in the first step, the nacelles and ducts that will simulate the actual engines will be designed. Additionally, the parameters for the simulations will be defined and an analysis of the different geometries involved will be made, optimizing them as necessary. Furthermore, an analysis of the functioning of the nacelles and ducts will be performed.

The next step will be to analyze the performance of the original configuration of the Airbus A320. This involves examining the differences between the wing without engines, the wing with actuator disks representing the engines, and the wing with actuator disks and ducts simulating the aircraft's engines.

The same procedure will be carried out, but this time, the engines will be placed in different areas of the wing. The first distribution to be analyzed will involve placing the engines above the wing, the second will involve adding more engines to the original configuration and the third will involve positioning the engines at different heights on the wingtips.

Finally, the configurations that gives the best results will be analyzed, taking into account their influence on the tail of the Airbus A320 and, if it's necessary aircraft design improvements will be considered taking into account those results.

1.4 Previous Research

This thesis is based on the prior research conducted by Floris Mariën titled "Software Testing: VSPAERO" (Mariën 2021). This work is mainly focused on testing the aerodynamic results of VSPAero, comparing them to some theoretical results using the two available solvers of the software, the VLM and the Panel Method.

1.5 Structure of the Work

This thesis consists of six main chapters and one appendix. The structure of the thesis is as follows:

Chapter 2 In this chapter, the VSPAero software and its features will be discussed.

Chapter 3 The theory upon which the operation of the fundamental aerodynamics, the VLM, panel method and the actuator disks OpenVSP is based will be explained in this chapter.

Chapter 4 In this chapter, the preliminary steps before the analysis will be described. The simulation parameters will be configured, and the surfaces to be analyzed will be optimized. Furthermore, a performance analysis of the disks will be conducted.

Chapter 5 The results of the simulations of the different engine distributions are going to be shown and analyzed in this chapter to find the one that gives the best aerodynamic results.

Chapter 6 In this chapter is going to be chosen the engine distribution that provided the best results.

Appendix A In this appendix the non-interpolated graphs of the results of the analysis are shown.

2 OpenVSP

2.1 History

As explained in both Mariën's thesis (Mariën 2021), Wikipedia (Wikipedia 2023j) and the OpenVSP website (OpenVSP 2022a), OpenVSP, or Open Vehicle Sketch Pad, is an open-source parametric aircraft tool originally developed by NASA. The predecessors of this software, developed by J.R. Gloude-mans and others for NASA in the early 1990s, were VSP, or Vehicle Sketch Pad, and RAM, or Rapid Aircraft Modeler.

VSP which is a tool developed over the years before 2010 to assist conceptual aircraft designers in achieving a balance between productivity and accuracy. It addresses the challenge faced by designers when transitioning from coarse geometric parameterizations, historically used for analysis, to more precise and detailed geometry required by modern analysis methods (Hahn 2010).

The RAM was developed in 1996 to generate detailed 3D geometric models quickly and easily. The models allowed a visual inspection of the geometry parameters used in the conceptual aircraft design and optimization process (Gloude-mans 1996).

Later, on January 2012, OpenVSP v2.0 was released as open source under the NOSA license in January 2012 (NOSA). Development has been led by Rob McDonald since around 2012 and has been supported by NASA and AFRL among other contributions.

The final OpenVSP v2 (which traces lineage back to VSP and RAM) was version 2.3.0 released in December 2013. Several 2.9.X versions came later, but these were in fact alpha and beta versions for the v3 re-write. The first such version, 2.9.0 was released in February 2014 (McDonald 2021). In the Figure 2.1 is possible to see a representation of all the history of OpenVSP since 2010 to 2022, summarizing all the versions and OpenVSP Workshops during those years.

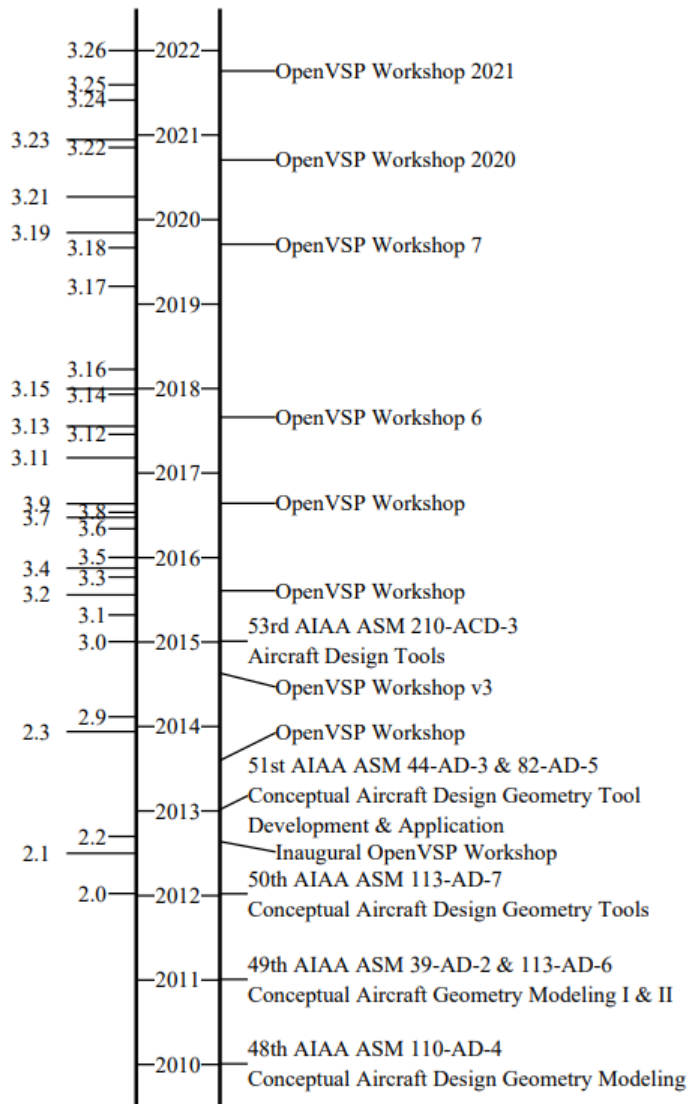


Figure 2.1 OpenVSP timeline (McDonald 2021).

2.2 OpenVSP Features

2.2.1 User Interface and Geometry Modelling

Once the program is opened, in OpenVSP, the GeomBrowser automatically opens. In this chapter is where you can add or remove various geometries available in the program, such as wings, the fuselage, disks, or ducts, among others. This is also where their characteristics are modified, although this process will be explained in more detail in Chapter 4.

Geometry modeling is indispensable in OpenVSP. With this tool, we can modify each parameter of the various geometries we intend to analyze. Clicking on each one of them opens a new window, displaying different tabs where you can adjust various properties depending on the geometry being analyzed. This is very useful and user-friendly, specially with the help of the OpenVSP Ground School which will be discussed later in Chapter 2.3.2.

2.2.2 Analysis Tools

OpenVSP offers a wide variety of tools that helps with the aerodynamic and structural analysis of the models. The tools available on the program are:

- CompGeom - Mesh generation tool that can handle model intersection and trimming.
- Mass Properties Analysis - Used to compute properties like centre of gravity and moment of inertia.
- Projected Area Analysis - Used to compute project area.
- CFD Mesh - Used to generate meshes that may be used in Computational fluid dynamics analysis software.
- FEA Mesh - Used to generate meshes that may be used in FEA analysis software.
- DegenGeom - Used to generate various simplified representations of geometry models like point, beam and camber surface models.
- VSPAERO - Used for vortex lattice or panel method based aerodynamic and flight dynamic analysis. This tool is explained in more detail in Chapter 2.4.
- Wave Drag Analysis - Used for estimating wave drag of geometries.
- Parasite Drag Analysis - Used for estimating parasite drag of geometries based on parameters like wetted area and skin friction coefficient.
- Surface fitting - Used for fitting a parametric surface to a point cloud.
- Texture Manager - Used for applying image textures to geometry for aiding visualization.

(Mariën 2021), (Wikipedia 2023j)

2.2.3 Compatibility

OpenVSP offers the capability to both read and write various types of data, often supporting multiple file formats for each data type. While certain types of data exchange may exclusively rely on the graphical user interface (GUI), many of these data formats can also be accessed and manipulated through command-line operations.

While this versatility empowers OpenVSP with significant functionality, it may initially appear complex to users new to the software. The following chapters aim to provide guidance to newcomers, offering insights into the types of data that OpenVSP can handle and facilitate both reading and writing processes.

In the next list all the input formats are shown:

- Parametric geometry (.vsp),
- Background image (.jpg),
- Surface textures (.tga, .jpg),
- Automation script (.txt),

- Airfoil definition (.af),
- Fuselage section definition (.fxs),
- Cabin definition (.cab),
- Wireframe as mesh (.hrm),
- Wireframe as surfaces (.hrm),
- Triangulated mesh (.stl, .NASCART),
- Vorlax case file (.cas).

In the next list all the output formats are shown:

- Parametric geometry (.vsp),
- Degenerate geometry (.csv, .m),
- Screen capture (.jpg),
- Automation script (.txt),
- Wetted area/volume report (.txt, .csv),
- Drag buildup report (.tsv),
- Area ruling report (.txt),
- Mass properties report (.txt),
- Wireframe (.hrm),
- X3D 3D Web model (.x3d),
- Felisa (.fel),
- Drawing (.dxf, .svg),
- Untrimmed surfaces (.3dm, .STEP, .IGES),
- Trimmed surfaces (.srf, .STEP, .IGES),
- Unintersected triangulated components (.tri, .facet, possibly others),
- Intersected triangulated components (.stl, .NASCART, .tri, .msh, .pov, .facet),
- Isotropic triangulated surface mesh (.stl, .poly, .tri, .obj, .msh, .NASCART),
- Structural mesh (.stl, .NASTRAN, .Calculix),
- Tagged, multi body structural mesh (.stl),
- Vorlax case file (.cas),
- Vorlax geometry & input (.inp).

(OpenVSP 2022b)

2.3 OpenVSP Tools

2.3.1 Hangar

A very useful tool available on the website of OpenVSP is the hangar. Here, a lot of different geometries made in OpenVSP are available. Here, you can find everything from aircraft geometries to engines or UAVs, and it features a search tool where you can filter the geometries based on what you're looking for. In the Figure 2.2 is possible to see an example of a search in the hangar.

Search Results

airbus

[Advanced Search](#)

Name	Source Quality	Manufacturer	Model	Downloads	Comments	Date
Airbus Beluga XL	1	Airbus	Beluga XL	624	1	2020-01-10
Roméo	2	Airbus	A380	949	0	2018-09-14
Roméo	4	Airbus Helicopters	Racer	277	0	2018-07-20
Roméo	2	Airbus Helicopters	AS-355	360	0	2018-07-20

Filter Results

VSP File Version

VSP 3.X (4)

Source Quality

1 - Definitive (1)

2 - Essentially Exact (2)

4 - Inaccurate (1)

Manufacturers

Airbus (2)

Airbus Helicopters (2)

Units

meters (4)

Tags

utility (2)

airliner (2)

airplane (2)

engine (2)

helicopter (1)

transport (1)

business (1)

Figure 2.2 OpenVSP Hangar (OpenVSPc).

2.3.2 Ground School and Workshops

In the ground school and the workshops it is possible to find a great variety of online tutorials. The tutorials of the ground school are divided in five Chapters. The first chapter is focused on the fundamentals of OpenVSP, the second one on the modeling and designing, the third one on the models of analysis, the fourth one in the capabilities to import and export files and the fifth one in advanced techniques. The workshops are interactive sessions that show you how to effectively use OpenVSP. These workshops typically cover a range of topics, from basic aircraft modeling and design concepts to advanced techniques and specific workflows (OpenVSPa).

2.3.3 Google Group

The OpenVSP Google group is an online forum where the OpenVSP user community gathers to discuss and share information related to the software. It's a space where users can ask questions, seek answers, share their experiences, and collaborate on OpenVSP-related projects. The Google group provides an efficient means to seek assistance, share knowledge, and stay updated on the latest news and developments related to OpenVSP. It is an active and vital part of the community surrounding this aircraft design software. The link to this group can be found by clicking [here](#):

OpenVSP Google Group

(OpenVSPb)

2.4 VSPAero

VSPAero is a potential flow aerodynamics tool developed by Dave Kinney at NASA Ames. It was initially a thin-surface tool using Vortex Lattice Methods (VLM) but with some formulation changes that differentiate it from classical VLM codes. VSPAERO was first released with OpenVSP 3.1.0. That version could calculate subsonic and supersonic flow utilizing a mesh agglomeration technique to accelerate the solution. The initial solver was multi threaded, included an actuator disk model, and could readily calculate steady stability derivatives. Today, the solver supports thick surfaces (in subsonic flow) as well as the original thin surface representation with control surface deflections supported in the thin surface mode (McDonald 2021).

The rapid pace of VSPAERO improvements has made it challenging for OpenVSP to keep up. What started as a meager wrapper is now a comprehensive GUI capable of managing cases and visualizing results. These improvements have been made by Nick Brake, Bryan Schmidt, and Justin Gravett. Forces and moment coefficients, load distributions, convergence histories, and pressure slices are automatically parsed and interactively visualized. OpenVSP provides a preview view of the degenerate form of the model. The GUI supports easy set up of cases with multiple sets of rotating blades making OpenVSP and VSPAERO an easy, fast, and powerful means of designing and analyzing advanced eVTOL concepts (McDonald 2021).

3 Theoretical Background

In this chapter all the theoretical background used in OpenVSP is going to be discussed. In the Figure 3.1 it is possible to see the general flowchart in a computational aerodynamics system. This process diagram is divided in three main parts: the geometry setup, the flow solver and the post-processing. Depending on the type of analysis that is going to be made there are also some general flow solver options, ordered from the most simplified model, which is the Linear Potential Model, to the complete flow model, which are the Navier-Stokes Equations (Liu 2007).

Considering inviscid, incompressible flow, the potential flow provides sufficient results over a wide range of conditions. The Laplace Equation is essentially an exact representation of this flow (Mariën 2021).

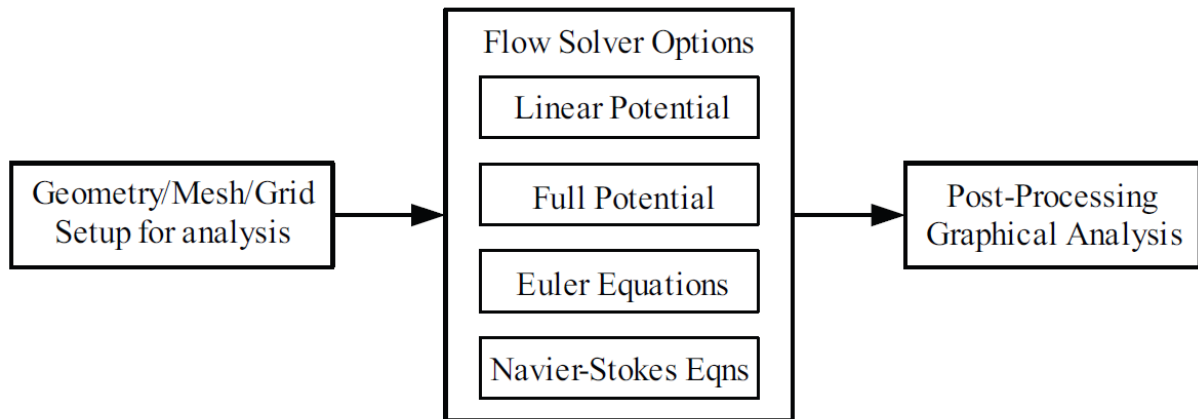


Figure 3.1 Typical functions in a computational aerodynamics system (Liu 2007).

3.1 Aerodynamic Fundamentals

3.1.1 Potential Flow

Beginning with the concept of irrotational flow, characterized by zero vorticity at every point

$$\xi = \nabla \times V = 0. \quad (3.1)$$

Being ϕ a scalar function and following the vector identity, we get

$$\nabla \times (\nabla \phi) = 0. \quad (3.2)$$

This implies that the curl of the gradient of a scalar function is consistently zero. When we compare equations 3.1 and 3.2, we can observe that

$$V = \nabla\phi. \quad (3.3)$$

The equation above states that in an irrotational flow, there is a scalar function ϕ that describes the velocity as the gradient of ϕ . This scalar function is referred to as the velocity potential. The principle of mass conservation in an incompressible flow leads to the following equation

$$\nabla \cdot V = 0. \quad (3.4)$$

With the definition of velocity potential ϕ , for a flow that is both incompressible and irrotational, equation 3.3 and 3.4 can be combined to yield

$$\nabla \cdot (\nabla\phi) = 0, \quad (3.5)$$

or

$$\nabla^2\phi = 0.$$

Equation 3.5 represents the well-known Laplace's equation, which governs irrotational, incompressible flow. Due to the linearity of Laplace's equation, (Anderson 1984) concludes that:

A complicated flow pattern for an irrotational, incompressible flow can be synthesized by adding together a number of elementary flows which are also irrotational and incompressible.

These different elementary flows include point/line source, point/line sink, point/line doublet and point/line vortex. The VLM method is based on the line vortices (Liu 2007).

3.1.2 Boundary Conditions

VLM employs the "thin airfoil boundary condition," which involves linearizing the boundary condition, transferring the boundary condition, as shown in the Figure 3.2, and making a linear approximation between velocity and pressure.

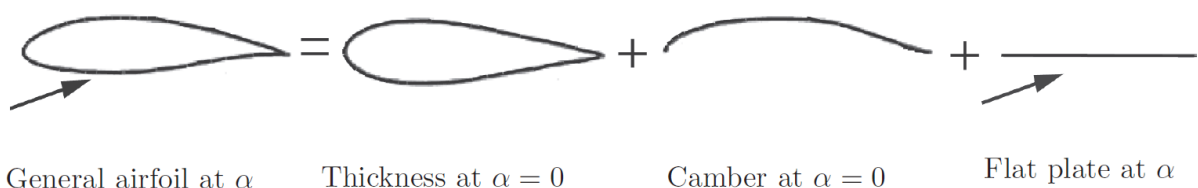


Figure 3.2 Decomposition of a general airfoil at certain incidence (Liu 2007).

Furthermore, after applying the linear approximation between velocity and pressure to the lower and upper surfaces of the airfoil, Mason (Mason 1998) obtained a very useful principle

For cases where the linearized pressure coefficients relation is valid, thickness does not contribute to lift to first order in the velocity disturbance!

The importance of this analysis is that the cambered surface boundary conditions can be applied on a flat coordinate surface and result in a much more easy way to apply boundary conditions (Liu 2007).

If the camber effect can also be neglected (symmetrical airfoil/wing), after applying this boundary condition to the linear partial differential equation (Laplace's equation) the problem can easily be solved by including the effect of angle of attack on a flat surface. In the following parts, the wing will be placed on the x-y plane. The boundary condition states that normal flow across the thin wing's solid surface is zero (Liu 2007):

$$\nabla(\Phi + \Phi_\infty) = 0. \quad (3.6)$$

It means the sum of the normal velocity component induced by the wing's bound vortices ω_b , by the wake ω_i and by the free-stream velocity Q_∞ will be zero (Liu 2007):

$$\omega_b + \omega_i + Q_\infty \alpha = 0. \quad (3.7)$$

3.1.3 Biot-Savart Law

As stated before, the two-dimensional vortex singularity is one of the solutions for Laplace's equation. The vortex flow is shown in the Figure 3.8.

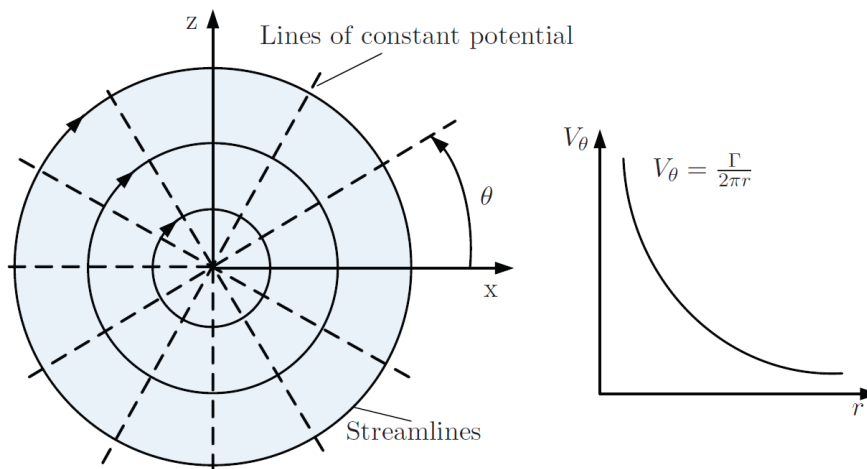


Figure 3.3 Point vortex flow (Liu 2007).

The induced tangential velocity by a vortex is (Liu 2007):

$$V_{\theta} = \frac{\Gamma}{2\phi r}. \quad (3.8)$$

where Γ is the field circulation strength and it is constant around the circle of radius r . Because the circulation has the same sign as the vorticity so it is positive in the clockwise direction. Here r is the radius to flow center.

The fundamental characteristics of a vortex filament are defined by the Kelvin and Helmholtz theorems. In connection with these theorems, a significant outcome can be obtained: A line (or sheet) of vortices can support a discontinuity in tangential velocity, resulting for example in a force, while the normal velocity remains continuous. This signifies that a vortex line or sheet can serve as a representation of a lifting line or surface (Liu 2007).

When the concept of a point vortex is extended to the case of a general three-dimensional vortex filament, the induced flow field created by the vortex filament can be observed in Figure 3.4.

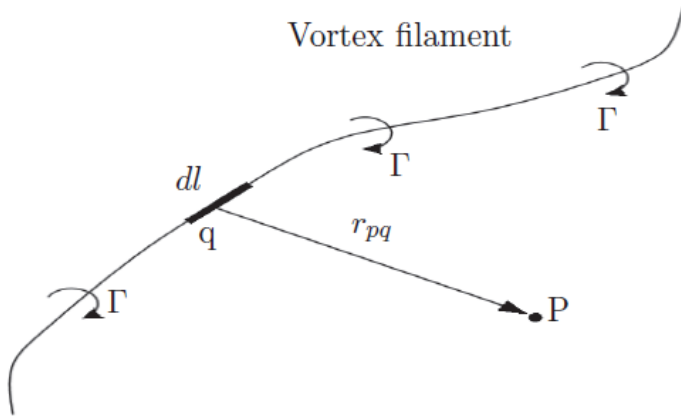


Figure 3.4 Three dimensional vortex filament (Liu 2007).

The mathematical representation of the flow induced by this filament is defined by the Biot-Savart law, which states that the incremental velocity dV at a point p , caused by a segment of a vortex filament dl at point q , is given by:

$$dV_p = \frac{\Gamma}{4\pi} \cdot \frac{dl \times r_{pq}}{|r_{pq}|^3}. \quad (3.9)$$

Which can be integrated over the entire length of the vortex filament to obtain the induced velocity

$$V_p = \frac{\Gamma}{4\pi} \int \frac{dl \times r_{pq}}{|r_{pq}|^3}. \quad (3.10)$$

3.2 VLM and Panel Method

The Vortex Lattice Method, is a numerical method, used in aerodynamic analysis, mainly in the early stages of aircraft design. The VLM models the lifting surfaces as a infinitely thin sheet of discrete vortices to compute lift L , induced drag D_i , lift curve slope, and lift distribution. Note that the influence of the thickness of the model and the viscosity of the fluid is neglected, so the VLM cannot compute viscous drag. In case of the VLM, the force distribution can be extracted to compute the aerodynamic coefficients and their derivatives important for aircraft's conceptual design (Mariën 2021).

For this kind of analysis a special form of vortex is used, the horseshoe vortex. It consists in four vortex filaments, two of them placed parallel to the direction of the free-stream velocity and starting at infinity, and the other two placed perpendicularly to the free-stream direction, with a finite longitude. The VLM represents the wing (or complete model) as a surface (or set of surfaces) on which a grid of horseshoe vortices are superimposed (see Figure 3.5). The velocities induced by each horseshoe vortex at a specified control point are calculated using the law of Biot-Savart (Mariën 2021).

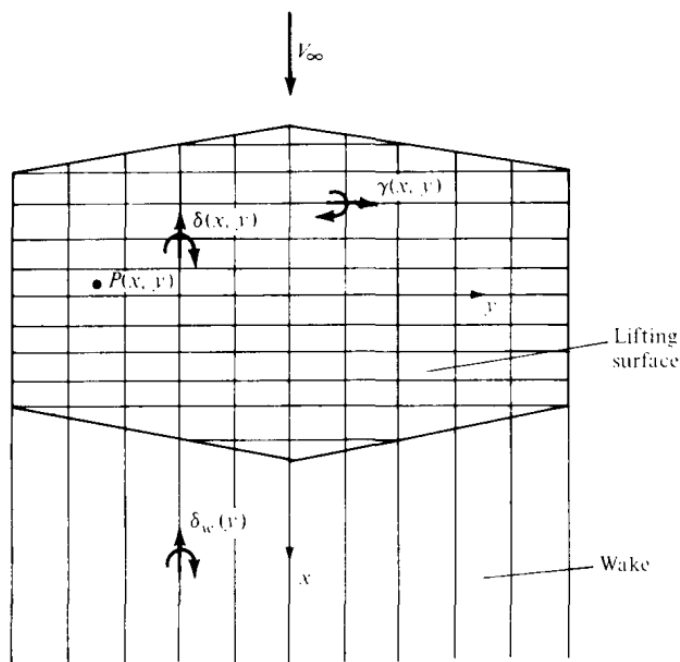


Figure 3.5 Schematic of a lifting surface with horseshoe vortices (Anderson 1984).

Panel methods are methods similar to the VLMs. They are numerical schemes for solving (the Prandtl-Glauert equation) for linear, inviscid, irrotational flow at subsonic or supersonic free-stream Mach numbers. There are fundamental analytic solutions to the Prandtl-Glauert equation known as source, doublet, and vorticity singularities. Panel methods are based on the principle of superimposing surface distributions of these singularities over small quadrilateral portions, called panels, of the aircraft surface, or to some approximation to the aircraft surface. The resulting distribution of superimposed singularities automatically satisfies the Prandtl-Glauert equation. To make the solution correspond to the desired geometry, boundary conditions are imposed at discrete points of the panels (Erickson 1990).

Once the panel discretization is done and the boundary conditions are setted in each one of the panels it is possible to calculate the potential flow in order to obtain the velocities in the domain of the body. Knowing the lift and drag equations, which are

$$L = \frac{1}{2} \cdot \rho \cdot V^2 \cdot S_W \cdot C_L \quad (3.11)$$

$$D = \frac{1}{2} \cdot \rho \cdot V^2 \cdot A \cdot C_D \quad (3.12)$$

where, in the equation 3.11 , L is the lift force, ρ is the air density, V is the velocity or true airspeed, S is the planform projected wing area and C_L the lift coefficient at the desired angle of attack, Mach number and Reynolds number (Wikipedia 2023h), and in the equation 3.12, F is the drag force, A is the cross sectional area and C_D the drag coefficient, also at the desired angle of attack, Mach number and Reynolds number (Wikipedia 2023c). With the velocity results, it is possible to obtain the aerodynamic forces and moments over the wing such as lift, drag or the pitching moment.

It is important to note that, the same as the VLM, in order to analyze the aerodynamics around a real case, the panel method has a series of limitations and assumptions that need the help of other kind of simulations or experiments in order to obtain more precise results. This is one of the main reasons OpenVSP is only used for preliminary analysis.

3.3 Actuator Disk

The actuator disk theory is used to model the airflow through a fan, rotor or any kind of advice in charge of moving a significant amount of air. To apply this theory it is necessary to assume a steady, inviscid, axisymmetric and incompressible flow (Chattot 2014).

Considering an actuator disk with radius R and pressure jump Δp in the x-direction. The disk is translating at a velocity $-U$ in the x-direction with respect to the ambient fluid. The quantities Δp or U may be of either sign. However it is assumed that the action of the disk creates a vortex tube that exits in the positive x-direction. This depends on the combination of Δp and U and the conditions under which it appears physical will be discussed later. In the reference frame of the disk the flow is steady, and the velocity in the far field is U , this is seen in Figure 3.6. Where "-" is equivalent to the disk, "- - -" to the streamtube not carrying out vorticity and ". - ." to the streamtube carrying vorticity. $U + u_2$ indicates the approximate local velocity with respect to the disk's reference frame (Spalart 2003).

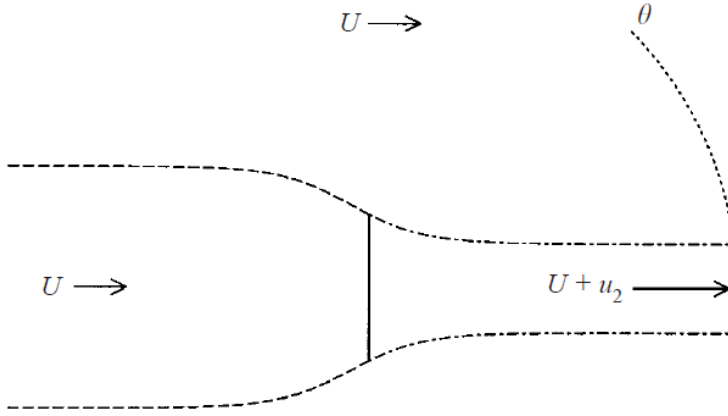


Figure 3.6 Actuator disk diagram (Spalart 2003).

For large positive x , the streamtube has radius R_2 , and the velocity inside it, with reference to the frame of the disk, is $U + u_2$. The velocity of the vorticity in the shear layer surrounding the streamtube is $U + u_2/2$. Therefore, a first-cut criterion for the model to be physical is $U + u_2/2 > 0$. The only assertion is that the edge of the actuator surface is the circle of radius R ; the surface could be a dome or cone, without changing the velocity field. This is because only the curl of the force field has any influence in an incompressible fluid, and this curl is concentrated on the rim (Spalart 2003).

The disk is aspirating fluid and expelling it through the tube at a rate $\pi R_2^2 u_2$ over the ambient U . Other than the tube surface, the fluid is irrotational. Therefore, the flow field induced by the disk at large distances is a sink, of magnitude $\pi R_2^2 u_2$, so that the velocity vector at a distance $r \gg R$ is

$$u = U e_x - u_2 \frac{R_2^2}{4r^2} e_r + O\left(\frac{1}{r^3}\right). \quad (3.13)$$

Here, e_x and e_r are the unit vectors in the x and r directions. The spherical coordinates place $\theta = 0$ as the direction in which the outflow tube points, so that $e_r \cdot e_x = \cos \theta$. To leading order, the sink term is what bends the streamline in Figure 3.6. The leading correction of order $1/r^3$ corresponds to an offset of the sink along the x -axis; it is centred at a distance of order R from the origin. The reason is that the shape of the streamtube is not known, and it represents the placement of a distribution of vortex rings in the vicinity of the origin, with a finite total circulation. The velocity induced by these vortex rings is of order $1/r^3$ for large r (Spalart 2003).

4 Simulation Settings

In the following chapter, the preliminary steps are described to carry out a series of simulations to be able to analyze the behavior of both the disks and the ducts in OpenVSP on the A320 wing. Two fundamental aspects will be discussed here: tessellation and clustering, and the methodology used to identify the optimal approach. In addition, the analysis of the disks will be deepened, evaluating their ideal location and distribution to guarantee an accurate examination. Lastly, we clarify the key parameters that will be used in our simulations.

4.1 Geometry

The geometry of the wing and tail that is going to be used on this analysis was obtained from the hangar available on the Scholz website (Scholz 2020). It is important to mention that the file available on this website is imported from the Version 2 of OpenVSP, and the version used for the analysis on this thesis is the Version 3. This means that the file `.vsp` needs to be saved as a `.vsp3` file. Knowing this we can proceed to the geometry itself. The ducts, however, have been created manually based on the Airbus A320 blueprints (Airbus 2005).

The fuselage has not been considered in this analysis because OpenVSP does not treat it as a lifting surface and only affects moment calculations instead of aerodynamics, which is the focus of study here.

4.1.1 Wing Geometry

The base geometry of the program, without performing any type of tessellation or clustering, is that of Figure 4.1. On it, a series of changes on its surface will be made to guarantee good results in the simulations. In the image is also easy to see the two different sections of the wing, being the first one the one that goes from the root to approximately 1/3 of the wing, where the geometry changes, and the second one from that section to the tips.

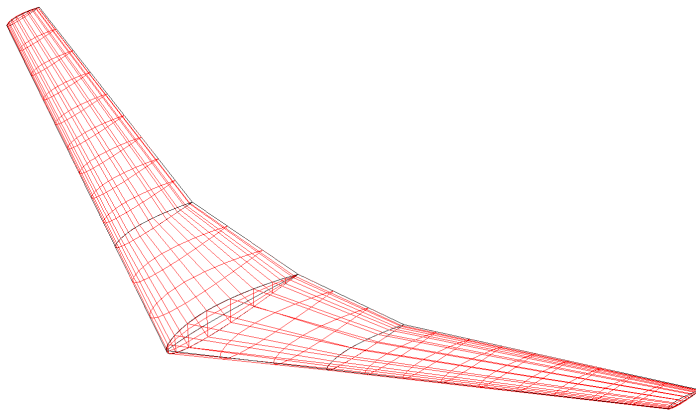


Figure 4.1 A320 wing geometry.

In the Table 4.1, the general parameters of the A320 wing can be observed. Nevertheless, it is crucial to consider that the wing's geometry is divided into two sections. The first section is closest to the wing's root, and the second section corresponds to the wingtip and the airfoil used is the NACA 2318. The characteristics of these sections are provided in the Table 4.2. It is also important to mention that the Span, Projected Span, Area and Aspect Ratio values in Table 4.2 are referred to the middle of the wing.

Table 4.1 General parameters of the wing.

Parameter	Symbol	Value	Unit
Span	b	33.940	[m]
Projected Span	b_p	33.806	[m]
Chord	c	4.007	[m]
Area	S_W	122.600	[m ²]
Aspect Ratio	AR	9.322	[/]
Incidence Angle	i_W	0	[°]

Dividing the wing in two sections makes it simpler to create a geometry as similar as the original one. Also, when we get to decide the tessellation parameters it will be important to take this into account because the setting parameters in both of the sections will be different, this will be discussed in the Chapter 4.3.1.

Table 4.2 General parameters of the sections of the wing.

Parameter	Symbol	Value Section 1	Value Section 2	Unit
Span	b	5.430	11.540	[m]
Projected Span	b_p	5.409	11.494	[m]
Area	S_W	29	32.300	[m ²]
Aspect Ratio	AR	1.017	4.123	[/]
Taper Ratio	λ	0.585	0.421	[/]
Sweep Angle	φ	0	27.282	[°]
Twist Angle	ε_t	0	0	[°]
Dihedral Angle	v_w	5.100	5.100	[°]

4.1.2 Tail Geometry

The tail of the A320 is separated in two, the vertical and the horizontal tail, the airfoil used in both of the wings is the NACA 0010. Starting with the vertical tail, it is possible to see in the Figure 4.2 that is divided in two sections that goes from the root to the middle of the wing and from there to the tip. However, the horizontal wing is only one section.

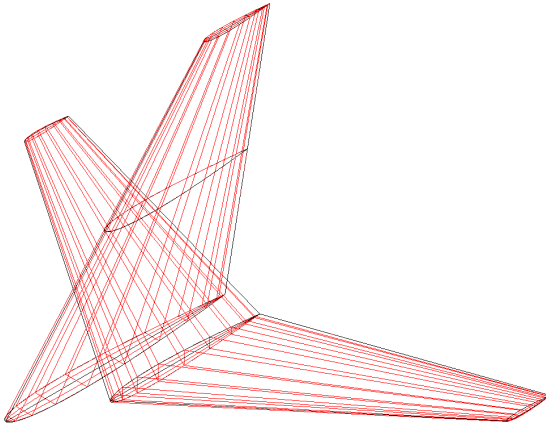


Figure 4.2 A320 tail geometry.

In the Tables 4.3 and 4.4 we can observe the parameters used for the design of the horizontal and vertical tail of the Airbus A320, respectively. The fact that both the vertical and horizontal tails have different sections will make the tessellation process on the Chapter 4.3.2 slightly different from each other.

Table 4.3 Parameters of the horizontal tail.

Parameter	Symbol	Value	Unit
Span	b	12.450	[m]
Projected Span	b_p	12.382	[m]
Chord	c	2.490	[m]
Area	S_W	31.000	[m ²]
Aspect Ratio	AR	4.945	[/]
Incidence Angle	i_W	0	[°]
Sweep Angle	φ	28.000	[°]
Twist Angle	ε_t	0	[°]
Dihedral Angle	ν_w	6.000	[°]

It is essential to note that the vertical tail will be only considered for wakes' visualization and not for reading coefficient results such as C_{Di} , C_{D0} , C_{Dtot} , C_L or C_p like on the main wing and the horizontal tail. This is because the vertical tail mainly influences aircraft directional stability instead of determining overall lift generation.

Table 4.4 Parameters of the vertical tail.

Parameter	Symbol	Value Section 1	Value Section 2	Unit
Span	b	2.935	2.935	[m]
Projected Span	b_p	2.935	2.935	[m]
Area	S_W	13.651	7.859	[m ²]
Aspect Ratio	AR	0.631	1.096	[/]
Taper Ratio	λ	0.650	0.462	[/]
Incidence Angle	i_W	0	0	[°]
Sweep Angle	φ	11.091	35.000	[°]
Twist Angle	ε_t	0	0	[°]
Dihedral Angle	v_w	0	0	[°]

4.1.3 Duct Geometry

As mentioned on the introduction of the Chapter 4.1, the ducts have been created manually using the blueprints of the Airbus A320 (Airbus 2005) and the characteristics of the engine IAE V2500, which is the one used as a reference for the analysis (Wikipedia 2023g). The tool of OpenVSP used for this was the "Body of Revolution" instead the "Duct" one available because it provides greater variety and fewer errors when creating new revolved geometries.

There are a few parameters that need to be setted to define the geometry. One of the most important ones is cross section. For this cross section we used the "EDIT_CURVE" where we will need to adjust the "Width" to 2.5, the "Height" to 0.380 and the "Depth" to 1.000, resulting in the duct section of the Figure 4.3.

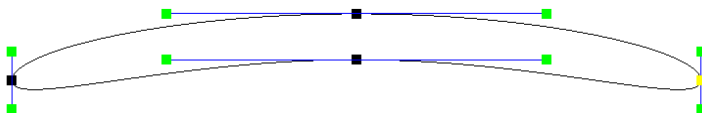


Figure 4.3 Cross section of the A320 ducts.

After having the cross section defined it is important to define the diameter of the duct, that following the characteristics of the engine is 1.682 m wide. The final result is the one showed on the Figure 4.4. For the tessellation analysis on the Chapter 4.3.3 the procedure is going to be slightly different from both the main wing and the tail.

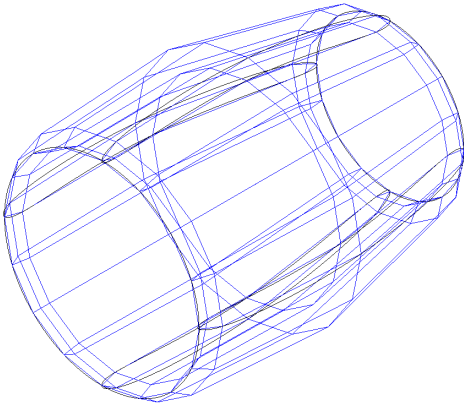


Figure 4.4 A320 ducts geometry.

4.2 Simulation Parameters

For all the simulations made in this document, the same settings have been used for all the simulations. In OpenVSP you can use any unit as you want as long as they are consistent. For example, if you want to use meters you must work with all the units related with the International System of Units, which is the one used on this thesis.

In the Figure 4.5 it is possible to appreciate the "Overview" of VSPAero, where you can set the principal parameters of all the simulations, such as the "Case Setup", the "Reference Area, Lengths", the center of gravity of the geometry in the "Moment Reference Position" section, that is automatically calculated by pressing the "Calc CG" button, and and the "Flow Condition".

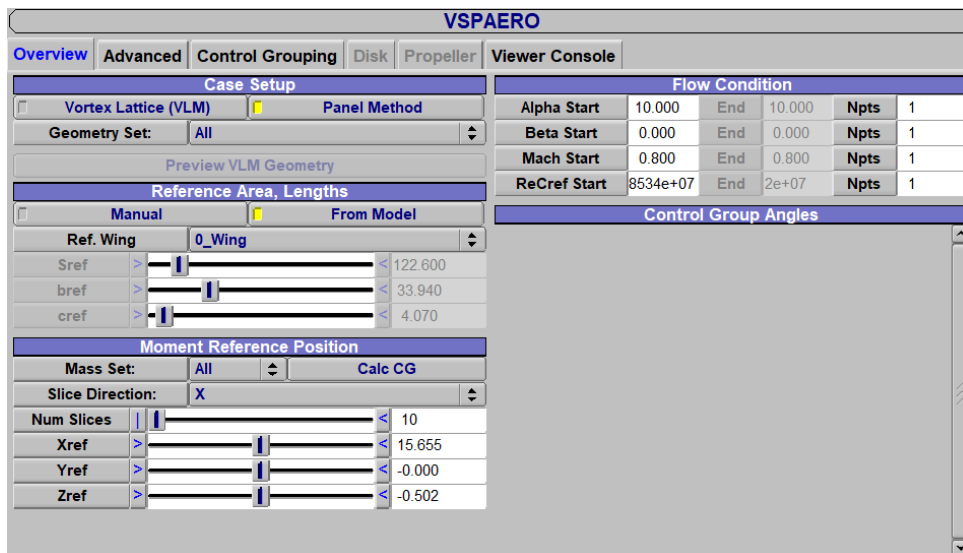


Figure 4.5 "Overview" section of VSPAero.

Following the steps of (Mariën 2021) carried out for the simulation of the Airbus A320, an α of 10° and a Mach of 0.8 have been established. In addition, the $ReCef$ (Wikipedia 2023k) used has been calculated taking into account the atmospheric conditions to which the aircraft will be

subjected at an average altitude of 12,000 meters and taking into account the maximum flight speed, in this case, 850 km/h, which is equivalent to 236.11 m/s. The density at this height is 0.31194 kg/m³ and the dynamic viscosity is 0.0000174 Pa s. With all these data and taking into account a chord of 6.741 m, the formula

$$Re_{Cef} = \frac{V \cdot \rho \cdot c}{\mu} \quad (4.1)$$

has been used resulting in a Re_{Cef} of 28,534,017.2, which is the parameter that will be used on the "Flow Condition" section. These are the only parameters that we need to set on the Tessellation (Chapter 4.3) and Clustering (Chapter 4.4) steps but for the disks we have to set also the "Advanced" and "Disk" parameters, which are displayed on the Figures 4.6 and 4.7, respectively.

Starting with the "Advanced" tab, the only parameters that has been changed are the "Propeller Representation", where you can activate or deactivate the influence of the disks, and the "Advanced Flow Conditions", setting the "Vinf" to 236.11 m/s and the density "Rho" to 0.31194 kg/m³ as we can see on the Figure 4.6. Also, depending on the different studies of the distribution of the engines on the wing we will add slices on the "Slicer" section to obtain more accurate results. The position of this slices will be discussed on the Chapter 5.

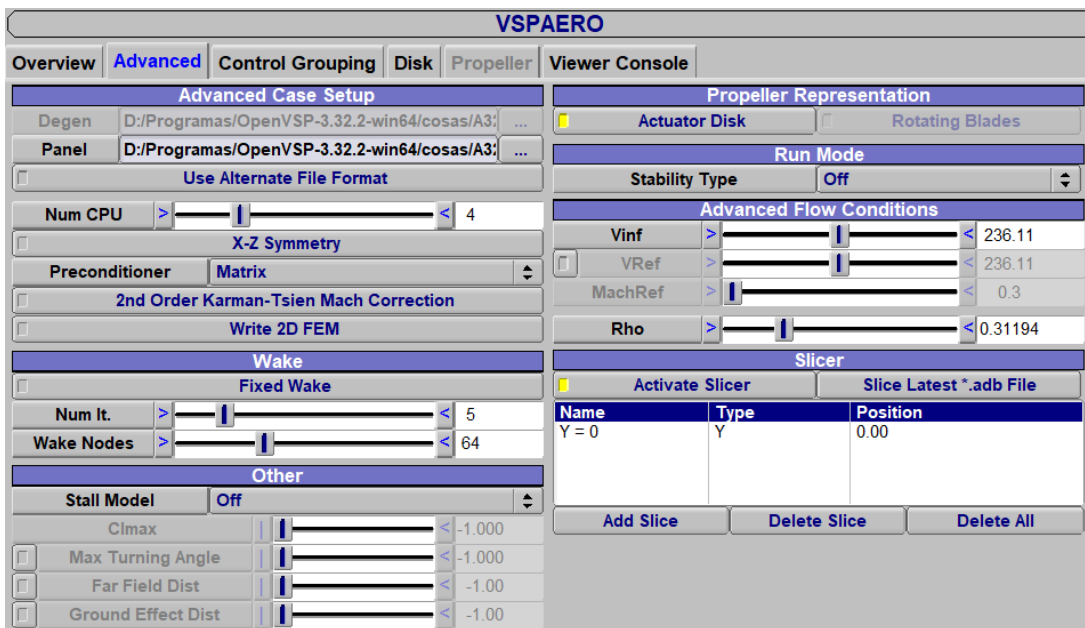


Figure 4.6 "Advanced" section of VSPAero.

Finally, on the "Disk" tab (see Figure 4.7), we can set the engine parameters such as the diameter "DIA", the revolutions of the engine "RPM", the coefficient of power "CP" and the coefficient of thrust "CT". The coefficient of thrust is calculated with the formula

$$CT = \frac{T}{\rho \cdot n^2 \cdot D^4} \quad (4.2)$$

And the coefficient of power is calculated with the formula

$$CP = CT \cdot \frac{V}{n \cdot D} = CT \cdot J \quad (4.3)$$

Where T is 140.56 kN, the ρ is 0.31194 kg/m³, the rpm are 14,950 and the D is 1.613 m. Then, CP is the result from the product of J times CT , where J is equivalent to 0.587. All this calculations result in a CT of 1.072 and a CP of 0.630 (Litherland 2021).

VSPAERO						
Overview	Advanced	Control Grouping	Disk	Propeller	Viewer Console	
Rotor Disk Element Settings						
INDX	NAME	DIA	HUB DIA	RPM	CP	CT
0	PropGeom_0	1.61	0.32	14950.0	0.63	1.07
1	PropGeom_1	1.61	0.32	14950.0	0.63	1.07

Dia.	1.613000
Auto Hub Dia.	< 0.323
RPM	< 14950.00
CT	< 1.072
CP	< 0.630

Figure 4.7 "Disk" section of VSPAero.

4.3 Tessellation

As the method used for the study is the panel method, having a good tessellation of the wing geometry is crucial. For this, two main parameters will be taken into account, W and U . Where W represents the number of separations along the chordspan of the wing and U the number of separations along the wingspan. Following the OpenVSP Workshops (Litherland 2021), on the distributions of the Figure 4.8 we can see in (A) and (B) that the relation between W/U is greater than 1, giving good but not optimal results, while in (C) and (D) is approximately 1. Even so, it is important to take into account the simulation time since, although having the cells as small as possible usually provides better results, there comes a point that if you keep increasing the tessellation where they end up converging with an unreasonable computation time, see case (D) on the Figure 4.8. In this chapter we will obtain the balance between results and computational time, which would be equal as the case (C) on the Figure 4.8.

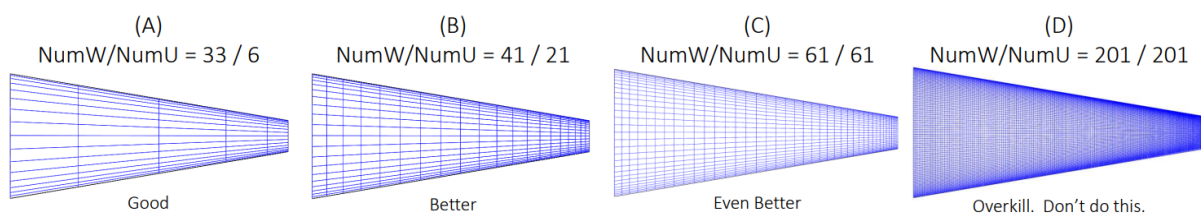


Figure 4.8 Tessellation examples in OpenVSP (Litherland 2021).

To choose the final tessellation, we will analyze the convergence of the results obtained from C_{Di} , C_{D0} , C_{Dtot} , C_L , e and the computational time where

$$C_{Dtot} = C_{Di} + C_{D0} \quad (4.4)$$

4.3.1 Wing Tessellation

As previously mentioned on the Chapter 4.1.1, the geometry consists of two parts and each one of them are going to have a different number of U , trying to maintain a total relation between W and U as close as 1 as possible. Since the ratio between W and U must be equal to or approximately 1 and it is known that section 1 and section 2 are approximately $1/3$ and $2/3$ of the total span of the wing, respectively, U_{s1} and U_{s2} must correspond to $1/3$ and $2/3$ of W . So that

$$\frac{W}{U} \approx 1 \rightarrow W \approx U = U_{s1} + U_{s2} \quad (4.5)$$

where U_{s1} and U_{s2} are, respectively

$$U_{s1} = \frac{1}{3} \cdot U \quad (4.6)$$

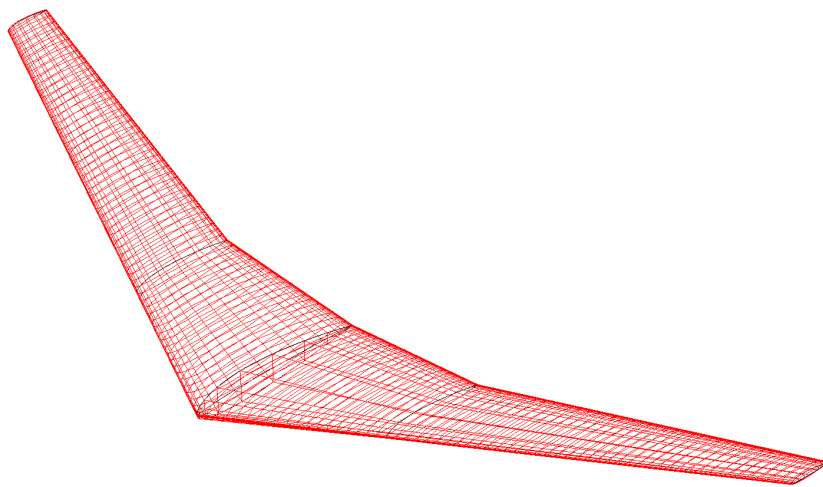
$$U_{s2} = \frac{2}{3} \cdot U \quad (4.7)$$

As can be observed in Table 4.5, all the compared coefficients converge as the tessellation is increased. However, as previously mentioned, there comes a point where the simulation time becomes unreasonably high, especially considering the minimal variation in results from one tessellation to another. For the main wing, a final tessellation of W equal to 61, U_{s1} equal to 20, and U_{s2} equal to 41 has been chosen. This is because it is the point where the values converge considerably well with a reasonable computation time.

Table 4.5 Wing tessellation convergence.

W	5	21	29	37	49	61	77	93
U_{S1}	2	7	9	12	16	20	25	30
U_{S2}	3	14	20	25	33	41	52	63
Time [s]	2.000	3.357	6.390	12.308	23.546	46.071	123.972	173.286
C_{Di}	-0.102	0.071	0.076	0.073	0.071	0.070	0.067	0.065
C_{D0}	0.012	0.015	0.016	0.015	0.015	0.015	0.015	0.014
C_{Dtot}	-0.091	0.086	0.092	0.088	0.086	0.084	0.082	0.080
C_L	1.075	1.380	1.383	1.347	1.327	1.32	1.318	1.297
e	-0.383	0.912	0.848	0.843	0.839	0.849	0.863	0.871

The final result after this step of the analysis is the one shown in the Figure 4.9. If you compare this with the panel distribution shown in the Figure 4.1 of the Chapter 4.1.1 it can be observed that the panels are more uniform, in addition to being smaller and well-defined. This remains in a better quality of results.

**Figure 4.9** Final Wing Tessellation.

4.3.2 Tail Tessellation

For the tail tessellation it was also considered a relation between W and U equal or close to 1. Then, for the vertical tail, the procedure to know how many U divisions are in each section is the same as the one followed on the main wing but changing the proportions occupied by each section such as U_{Ts1} and U_{Ts2} are

$$U_{Ts1} = U_{Ts2} = \frac{1}{2} \cdot U \quad (4.8)$$

While for the horizontal wing W and U are going to be the same. For this part of the tessellation process no analysis has been made. This is because knowing the best panel distribution of the wing and knowing that the tail shape is very similar as they are both wing-shaped, as long as you have consistency and define a tessellation which makes sense with the results you are looking for there is no need to overkill the simulation on surfaces which results that are not as important as the ones provided for the main wing.

The tessellation used for both the horizontal and vertical tail are $W = U = 25$ and $W = 25$, $U_{Ts1} = 12$ and $U_{Ts2} = 13$ due to its two sections, respectively. The panels on this part of the geometry are slightly bigger than the ones on the main wing as can be observed in the Figure 4.10.

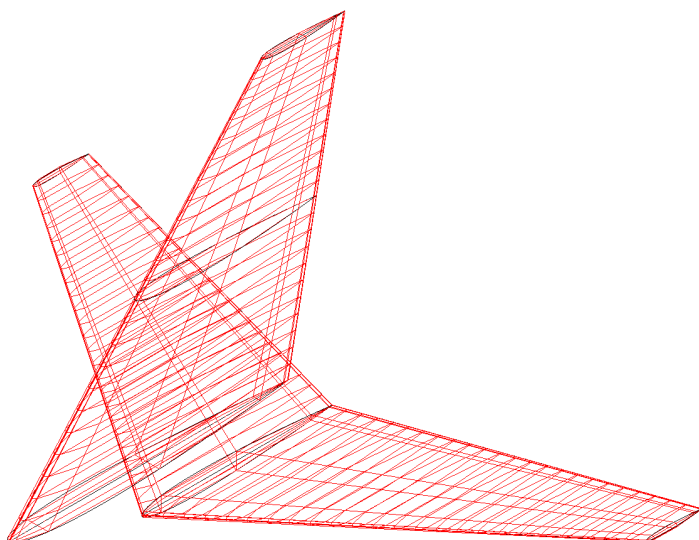


Figure 4.10 Final tail tessellation.

4.3.3 Duct Tessellation

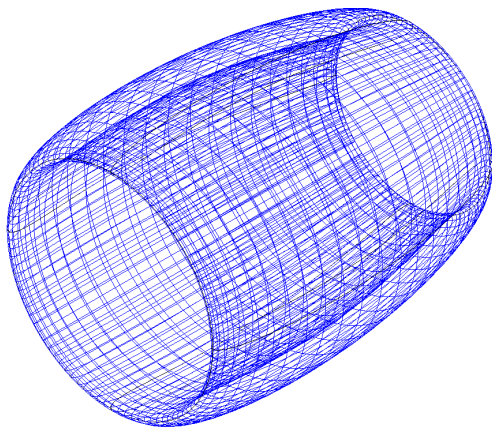
As explained in Chapter 4.1.3, the ducts have been defined as a "body of revolution." This implies that the ratio between W and U has to be twice that of the main wing. This is because the "body of revolution" functions like an airfoil rolled upon itself, so in order to maintain a similar distribution in the tessellation as in the main wing, the condition $W/U = 2$ must be satisfied.

In the convergence analysis shown in the Table 4.6 most of the values are extremely small so the main value that is going to be used to choose the tessellation of the ducts is the efficiency factor. There is a constant tendency on that value until we reach the configuration $W = 53$ and $U = 27$, where the values suddenly drop. This is why the final configuration used for the ducts is the previous one, which is $W = 49$ and $U = 25$.

Table 4.6 Duct tessellation convergence.

W	17	21	29	37	49	53	57
U	9	11	15	19	25	27	29
Time [s]	2.584	3.456	6.571	12.106	25.535	31.521	40.349
C_{Di}	0.000	0.000	0.000	0.001	0.001	0.001	0.001
C_{D0}	0.002	0.002	0.002	0.002	0.002	0.002	0.002
C_{Dtot}	0.001	0.002	0.002	0.003	0.003	0.003	0.003
C_L	0.004	0.005	0.005	0.006	0.006	0.006	0.006
e	-2.857	2.637	2.437	1.736	1.647	1.049	1.056

Resulting in the final tessellation shown in the Figure 4.11, with a considerable higher resolution when compared with the initial duct previously designed (see Figure 4.4).

**Figure 4.11** Final duct tessellation.

4.4 Clustering

Clustering is used to refine or coarsen the mesh of a given geometry. It consists in grouping or redistributing the control points or vertices of a surface to achieve a smoother surface, a more refined mesh with a higher level of detail in the most problematic areas and also computational efficiency, focusing more in those areas of the geometries and reducing resources and time required for the simulations.

The analysis in this part will be different depending on the geometry used. For the wing and the tail we will use the same clustering configuration, both span and chord wise, and for the ducts it's only going to be chord wise as the geometry is a body of revolution, this is based on the information from one of the OpenVSP Workshops (Litherland 2021).

4.4.1 Wing and Tail Clustering

Following the same hypothesis as the one in Chapter 4.3.2, an equivalent clustering setup is going to be used both for the wing and the tail even though the analysis is going to be made on the main wing.

Chord Wise Clustering

We will begin with clustering along the chord without any clustering along the wing span, where we are going to analyze two different configurations following the criteria shown in (Litherland 2021). Following these guidelines, clustering will be applied in two regions: the leading edge and the trailing edge to achieve a more accurate and efficient analysis of the aerodynamics. By concentrating more points in these critical regions, we can capture the flow behavior and pressure distribution more effectively, leading to improved accuracy in lift, drag, and other aerodynamic coefficients. Regarding to the configurations used for the analysis, we will maintain a constant value of 0.25 for clustering at the leading edge in both of them, and then vary the clustering at the trailing edge to 1 and 0.25, respectively, as shown in the Figure 4.12.

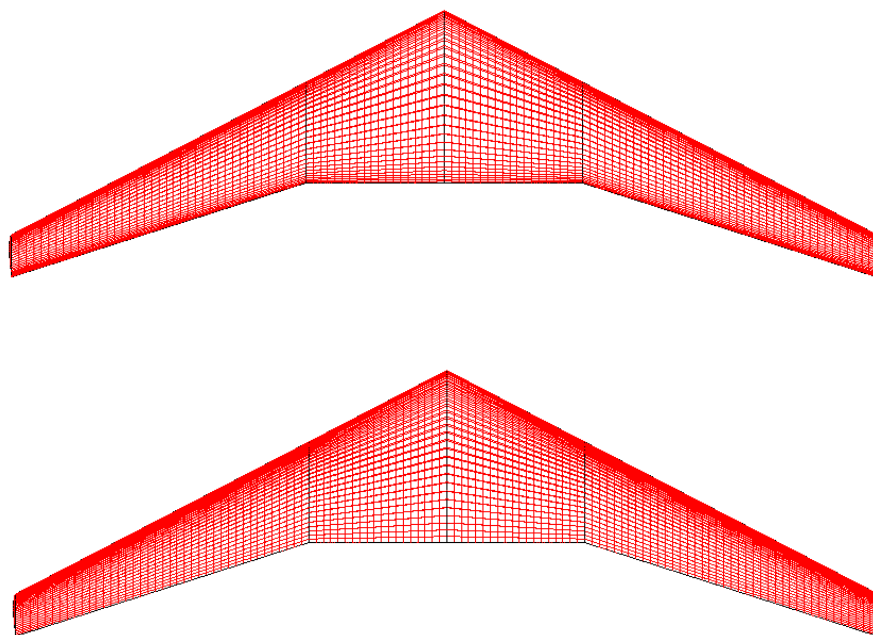


Figure 4.12 Chord wise clusterings of the wing. From top to bottom: $LE = 0.25$, $TE = 0.25$; $LE = 0.25$, $TE = 1.00$.

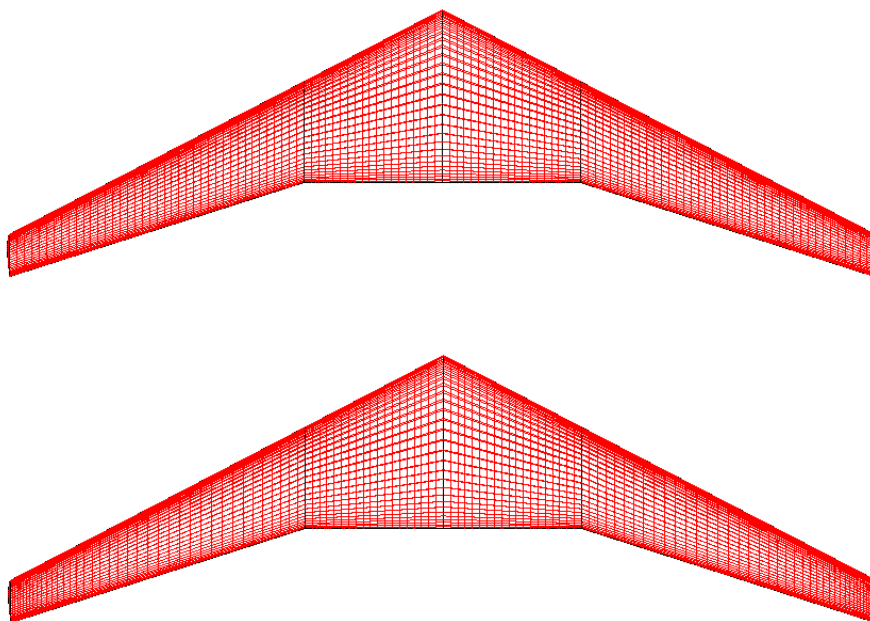
The results obtained from both simulations are very similar as can be observed in the Table 4.7. As the results obtained are very similar and the variations are negligible the final chord wise clustering configuration chosen is the more detailed one, which means $LE = TE = 0.25$, to assure a good calculus resolution.

Table 4.7 Chord wise clustering results of the wing.

LE	0.25	0.25
TE	1	0.25
Time [s]	47.492	46.071
C_{Di}	0.074	0.070
C_{D0}	0.015	0.015
C_{Dtot}	0.089	0.084
C_L	1.344	1.320
e	0.832	0.849

Span Wise Clustering

Now, using the chord wise clustering previously analyzed, we are going to see how the clustering along the wing affects it's results. Three main points are going to be considered: the root, the middle section of the wing where the geometry changes and the tip. In the case of the root clustering, it will be kept constant and equal to 1 because, in reality, the wing root is located at the fuselage, and it is not considered a region that requires analysis refinement. However, in the section change and wingtip regions, where the geometry varies significantly, a refinement will be performed. Similar to the chord-wise clustering, the refinement in this areas aims to ensure a higher resolution of the results in these critical areas (Litherland 2021). In the Figure 4.13 it is possible to see the different distributions in the clustering along the span of the wing, becoming more refined both in the middle section and the tip as we reduce the clustering.



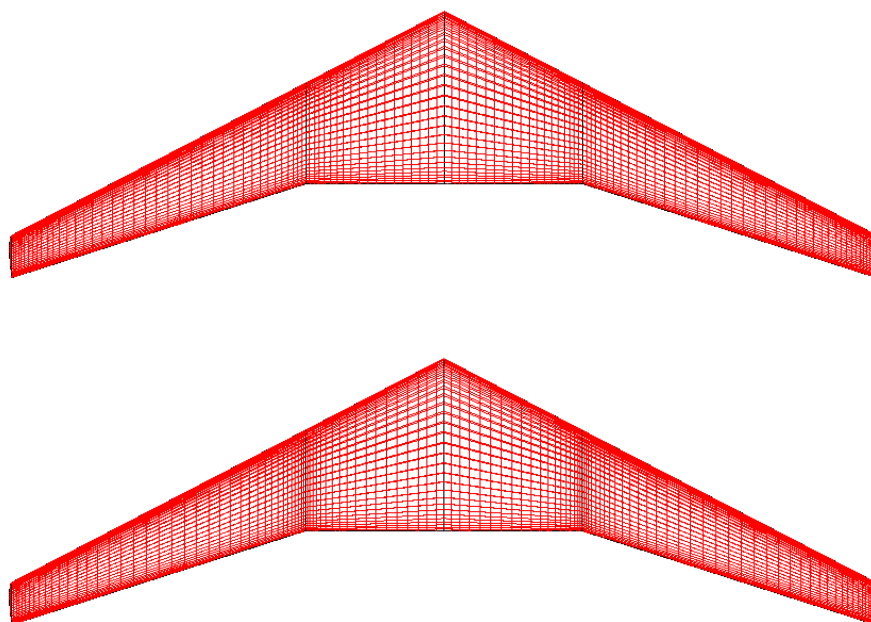


Figure 4.13 Span wise clusterings of the wing. From top to bottom: RT = 1.00, MID = 1.00, TIP = 1.00; RT = 1.00, MID = 1.00, TIP = 0.25; RT = 1.00, MID = 0.50, TIP = 0.25; RT = 1.00, MID = 0.25, TIP = 0.25.

Similar to the previous case, the results do not vary significantly from one another (see Table 4.8). However, in this instance, the option of the most refined sections (last one in Figure 4.13) has not been chosen. This decision was made because when analyzing the distribution along the wing of the coefficients presented in Table 4.8 for the last case, some peculiar fluctuations were observed in the section change area, likely resulting from excessive refinement in that region. Therefore, the final selected configuration for the main wing is root = 1, middle section = 0.50, and wingtip = 0.25, equivalent at the third configuration of the Figure 4.13.

Table 4.8 Span wise clustering results of the wing.

Root	1	1	1	1
Middle Section	1	1	0.5	0.25
Wingtip	1	0.25	0.25	0.25
Time [s]	46.071	41.82	44.964	44.777
C_{Di}	0.070	0.068	0.069	0.070
C_{D0}	0.015	0.015	0.015	0.015
C_{Dtot}	0.084	0.083	0.083	0.085
C_L	1.320	1.323	1.319	1.315
e	0.849	0.866	0.858	0.834

Finally, for the tail of the Airbus A320, the clustering chosen following the analysis realized of the main wing is, for the horizontal wing, a root clustering equal to 1 and a wingtip clustering equal to 0.25, and for the vertical wing, a root clustering equal to 1, a middle section clustering equal to 0.50 and a wingtip clustering equal to 0.25. The final panel tessellation of the tail is shown in the Figure 4.14.

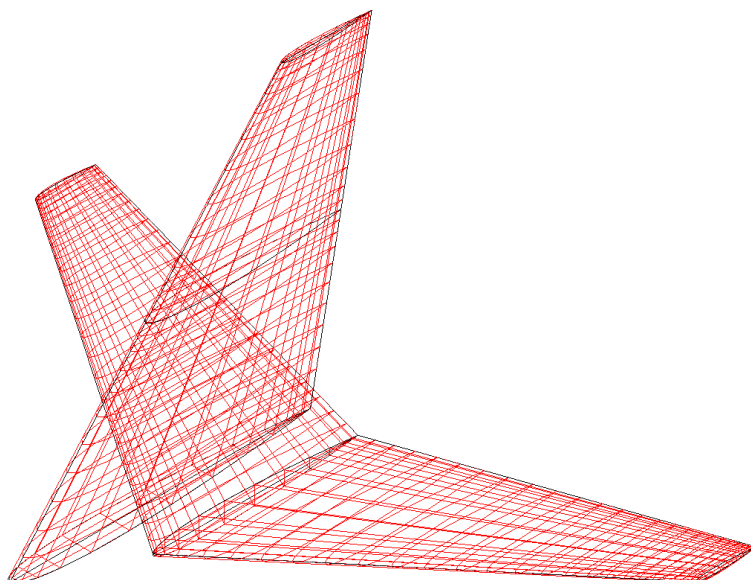


Figure 4.14 Final clustering of the tail.

4.4.2 Duct Clustering

The duct clustering analysis is only going to be made on its leading and trailing edges, following the advice from (Litherland 2021) given for wing clustering to ensure the best results as possible as those are the most conflicting areas in the geometry. The clustering of the leading edge will remain at 0.25 and only the trailing edge one is going to be changed but in this case three different trailing edge clustering are going to be analyzed, with a value of 1, 0.50 and 0.25. If you see closely, in the Figure 4.15 is possible to see how reducing the clustering on the trailing edge makes the panels around that area thinner and enlarging the neighbour panels.

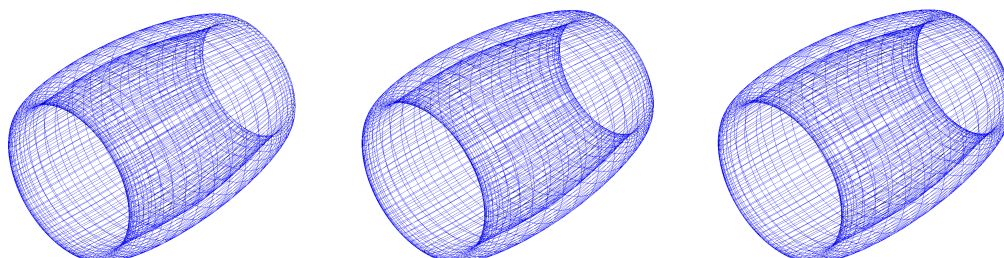


Figure 4.15 Chord wise clusterings of the ducts. From left to right: LE = 0.25, TE = 1.00; LE = 0.25, TE = 0.50; LE = 0.25, TE = 0.25.

As expected after the results obtained from the wing and the tail, the results obtained from the analysis of the ducts barely vary, this is shown in the Table 4.9. For this reason, the clustering chosen for the ducts is the more refined one, with $LE = TE = 0.25$.

Table 4.9 Clustering results of the ducts.

LE	0.25	0.25	0.25
TE	1	0.50	0.25
Time [s]	26.14	24.331	25.535
C_{Di}	0.001	0.001	0.001
C_{D0}	0.002	0.002	0.002
C_{Dtot}	0.003	0.003	0.003
C_L	0.006	0.006	0.006
e	1.647	1.647	1.647

4.5 Disk Analysis

In this chapter we are going to explain how the disks work and how we can set its main design parameters in OpenVSP. Also we are going to make an aerodynamic analysis of its influence inside the ducts, depending on the direction of rotation and on the number of disks used, to find the configuration that provides the most uniform wakes as possible.

4.5.1 Performance and Design Parameters

To fully understand how disks works, first we have to define what a disk is in terms of OpenVSP. Unlike geometries such as the wing or the ducts, disks are not physical objects, and its main objective is to provide an instantaneous "jump" in the local pressure which changes the flow through the disk (Litherland 2023). That is why we cannot analyze the performance of the disks on its own and we need to have a surface, like the wing or the ducts, in order to be able to study the wakes influenced by them on these surfaces.

It is also important to highlight that the direction of rotation of the disks is going to be very important in this section. Following the study from (Veldhuis 2004) and (Sinnige 2019) that explains that the best propeller rotation to obtain a higher lift is inboard up instead of outboard up, both for high and low speed flight simulations. This is why the disks are going to be mainly setted up taking into account this direction of rotation.

Regarding to the design of the disks, as they only represent the jump of the local pressure, there are not many things to take into account because most of the parameters were setted in the Chapter 4.2. The only three parameters that are going to be changed are the diameter, that is going to be 1.613 m according to the technical specifications of the engine (Wikipedia 2023g),

the direction of rotation and the position of the disks, which will be in the front, in the back and in both to find the one that induces the least perturbations in the flow while maintaining the flow rotating inwards up to achieve a higher lift.

4.5.2 Aerodynamic Analysis

For the aerodynamic analysis we are going to follow a couple of steps. First, we are going to analyze how only one disk affects the aerodynamics of the ducts, positioning it in the front and then in the back. Then, three different configurations of disks located both in the front and the back of the ducts are going to be analyzed by changing the direction of rotation of both disks. The first configuration will be with both disks rotating inwards up, the second one with the disk in the front rotating in an inwards up direction and with the one in the back in an outwards up direction and then, the third one that will be the opposite as the second one. To finish, we are going to compare the best results from the study with only one disk and with both of them to choose the one with better results.

One Disk

As mentioned before, in this first step only one disk in the ducts is going to be analyzed. In the Figure 4.16 is possible to see both of the configurations for this first analysis. In the disk configuration images, only the engine on the right wing side will be displayed to better observe the differences. However, in the simulations, both engines have been taken into account. Additionally, it is important to consider that the rotation direction will be opposite for the engine on the opposite side. In this chapter, only one rotation direction will be considered, which is inwards up. The direction of rotation can be seen in the figures and it is indicated by the circular arrows.

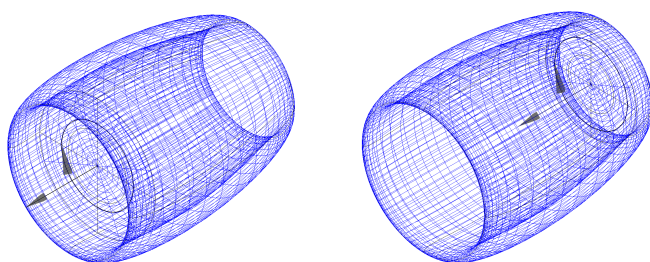


Figure 4.16 Disk configurations for the One Disk analysis.

In the Figures 4.17 and 4.18 we can observe the first results. Having the disks in the front increases heavily the pressures inside the duct compared with the disks in the back, but it is something to be expected since the flow inside the ducts is being accelerated. This is why that parameter is not going to be taken into account in this part of the analysis.

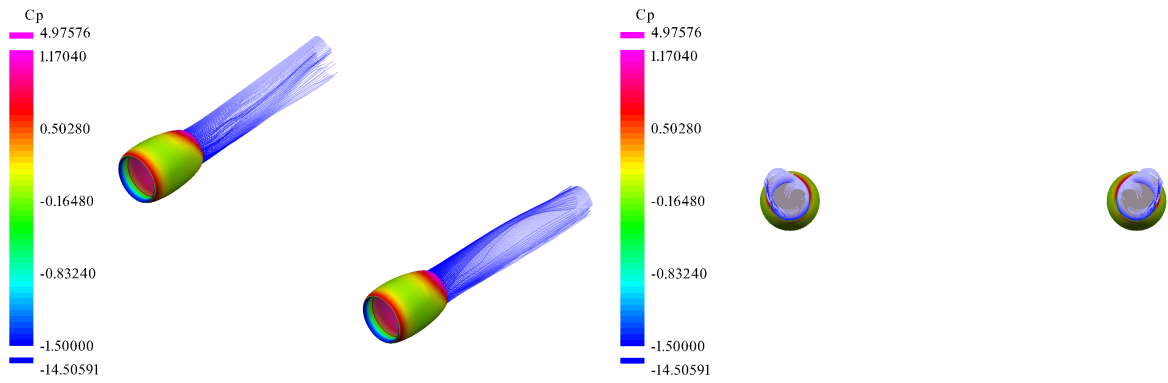


Figure 4.17 Aerodynamic results of the One Disk analysis with the disks in the front.

As for aerodynamics, notable differences can be observed between one simulation and another. In Figure 4.17, with the disks located at the front of the duct, the wakes appear much more uniform compared to the case in Figure 4.18, where the recirculation in an outwards up direction is significantly greater, and the wakes are considerably less uniform. For this reason, the disks in the front is the one that is going to be used to compare if its better to use only one or two disk configuration.

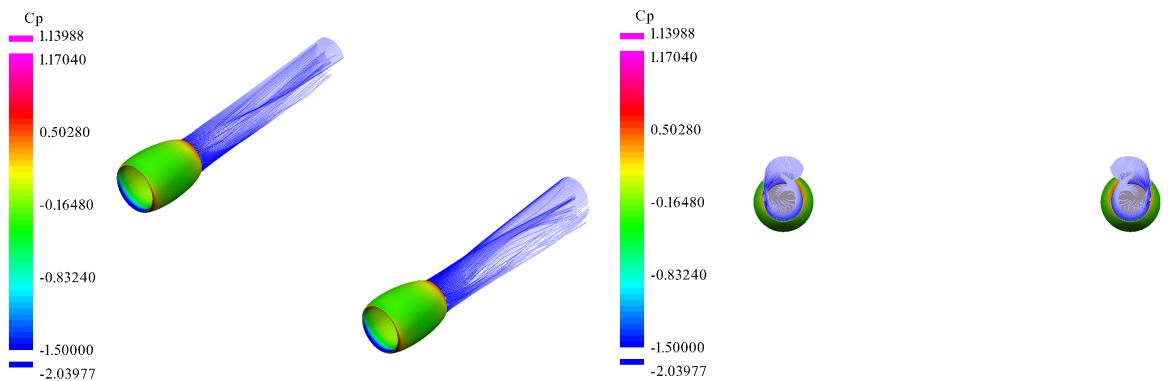


Figure 4.18 Aerodynamic results of the One Disk analysis with the disks in the back.

Two Disks

In Figure 4.19, you can see the three configurations that will be used for this analysis. As mentioned in the introduction of this chapter, the engine on the left has both disks rotating in an inwards up direction, the second one has the front rotating in the same direction while the rear rotates in an outwards up direction, and finally, the one on the right has the front disk rotating in an outwards up direction while the back one rotates in the opposite direction.

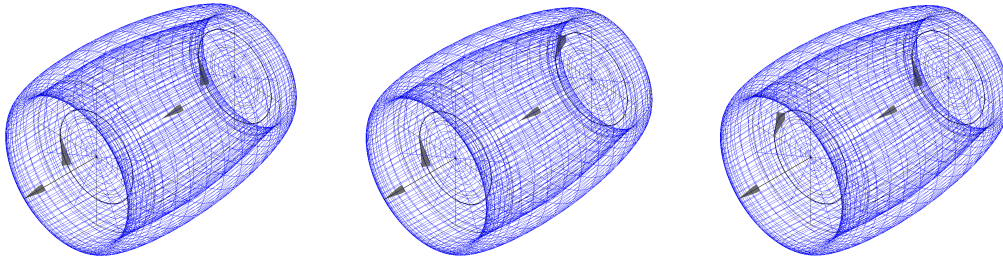


Figure 4.19 Disk configurations for the Two Disks analysis.

In the isometric view of the Figure 4.20, it can be observed that the outgoing flow from the engines is not very uniform. This is evident in the rear view on the right, where the flow, despite both disks rotating in an 'inwards up' direction, exhibits significant recirculation.

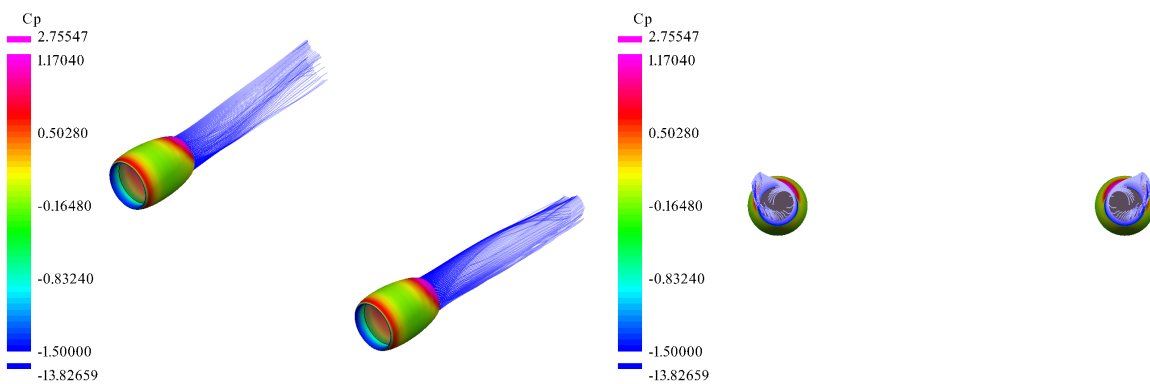


Figure 4.20 Aerodynamic results of the Two Disks analysis with both of the disks rotating inwards up direction.

In the configuration with the front disk rotating inwards up and the back one rotating outwards up of the Figure 4.21 is possible to notice that the flow is considerably more uniform than in the previous case. Anyways, in the rear view, it can be seen that the flow predominantly rotates in an outwards up direction, which is the opposite direction that we are trying to achieve, probably caused because the direction of the flow of the second disk is rotating in that direction.

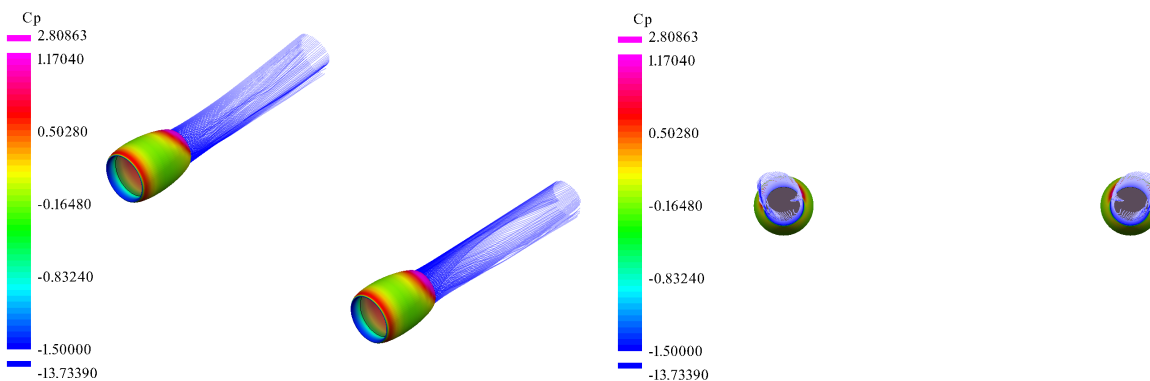


Figure 4.21 Aerodynamic results of the Two Disks analysis with the front disk rotating in inwards up direction and the back disk rotating in outwards up direction.

For the last simulation with the front disk rotating in outwards up and the back one rotating inwards up of the Figure 4.22 we can also see that the flow is smoother that in the first case but with the difference that the outgoing flow from the duct is rotating inwards up instead of outwards up like in the second simulation. This makes this configuration the best choice to take into account between this simulations.

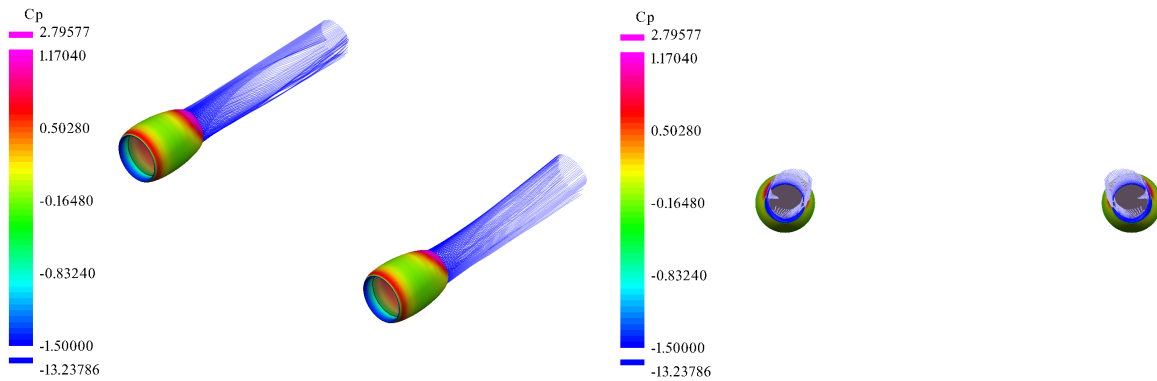


Figure 4.22 Aerodynamic results of the Two Disks analysis with the front disk rotating in outwards up direction and the back disk rotating in inwards up direction.

Final Choice

The two configurations that are going to be analyzed in this chapter are the one with the disks in the front rotating inwards up and the one with the disk in the front rotating outwards up and the one in the back rotating inwards up. In the Figures 4.23 and 4.24 we can easily observe the main differences between both wakes.

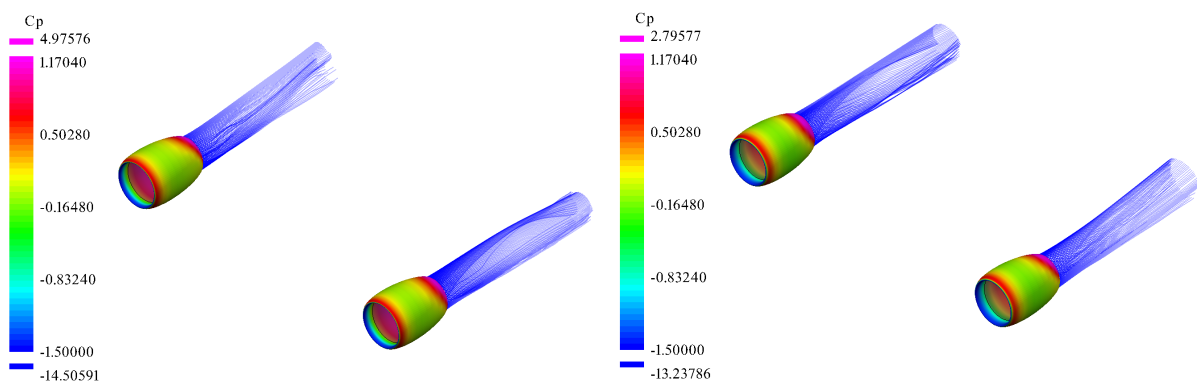


Figure 4.23 Aerodynamic results of the One Disk analysis with the disk in the front and the Two Disks analysis with the first disk rotating in outwards up direction and the second rotating in inwards up direction with isometric perspective.

The first difference that can be observed is that in the configuration with two disks, the wakes are considerably more uniform, implying that most of the flow rotates in an inwards up direction. Additionally, the pressures sustained within the duct with the two disks are slightly lower than with a single disk, resulting in lower stresses in the geometry. Lastly, the configuration with two

disks is more realistic than with one, as it takes into account both the inflow and outflow of the flow in the engine. Therefore, the two-disk configuration will be chosen as the final setup for the simulations in Chapter 5.

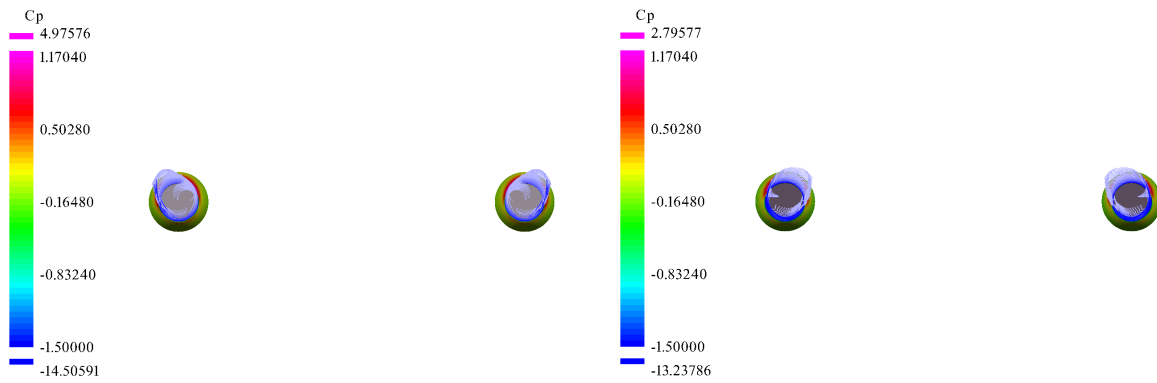


Figure 4.24 Aerodynamic results of the One Disk analysis with the disk in the front and the Two Disks analysis with the first disk rotating in outwards up direction and the second rotating in inwards up direction with rear perspective.

5 Results

In this section we will discuss the results obtained from a series of simulations, where different engine position configurations have been analyzed. Within each of the analyses the different geometries and the results, both numerical and aerodynamic, of the wing will be presented for the different cases studied. This studies will be divided in two: those that will consist of the wing only with the disks and the wing with the disks and the ducts in order to see the influence of the ducts.

5.1 Base Case

The base case is the one that will be used as a reference as it is the actual A320 case. In this case the tail has not been taken into account for the simulations to save computational time, therefore a separate analysis will be performed, where the tail will be taken into account (Section 5.5), which will be compared with the case that provides the best results of the geometries with the engines in other positions.

Geometries

In the Figures 5.1 and 5.2 are shown the three geometries that are going to be analyzed in this section. The first one is only the wing, without any disks or ducts, since it is necessary to know how the wing behaves by itself to be able to analyze the influence of the disks and ducts. In the other two cases, we will see how using only disks to simulate the engines and using both disks and ducts separately affect the general results of lift, drag and pressure coefficients of the wing.

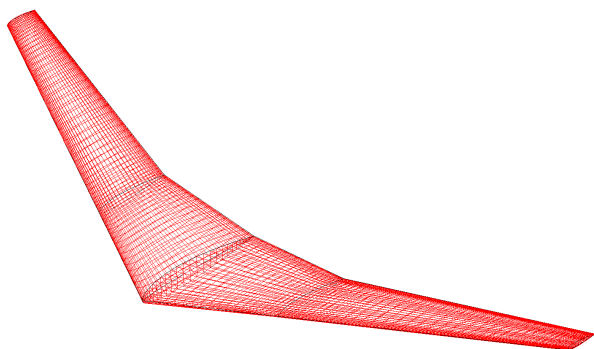


Figure 5.1 A320 wing geometry.

A detail that will be important in most of the simulations is the position of the engines. In this case, they are both situated below the wing and at a distance of 5.755 meters from the wing center, which according to the non-dimensional span is equivalent to the position located near ± 0.35 . This can be seen in the Figure 5.2.

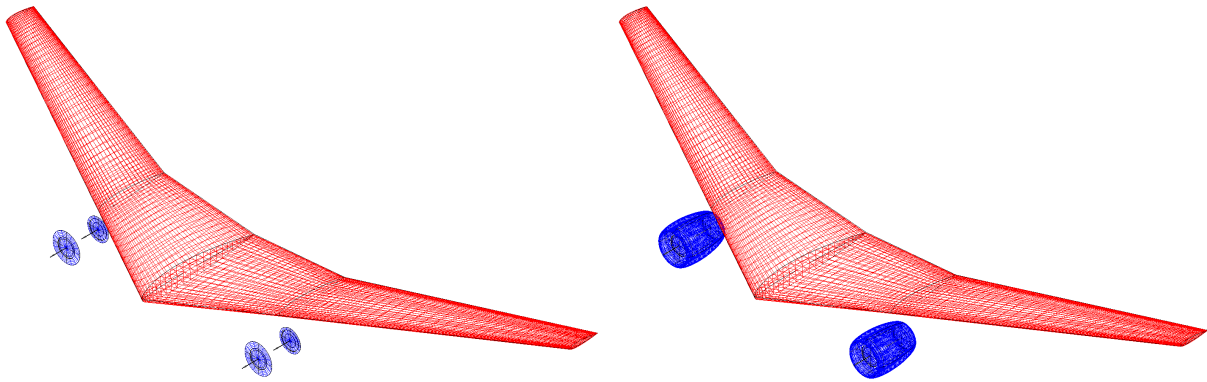


Figure 5.2 Base Case geometries. From left to right: wing & disks case and wing, disks & ducts case.

Numerical Results

Continuing with the results obtained from the simulations of the wing. We have in Figure 5.3 the comparison of the drag coefficient of the wing, the wing with the disks and the wing with the disks and the ducts. The one that offers better results in terms of drag is, as expected, the wing without any disks or ducts, followed by the wing and disk case and then the wing, disk and ducts case. When there are no ducts involved, the drag resulting from the airflow generated by the disks is lower than when the ducts are used. This is because the interference of the duct geometry itself causes the flow to be not as smooth as when only the disks are used, thus causing these drag peaks on the wing, as shown in the Figure 5.8.

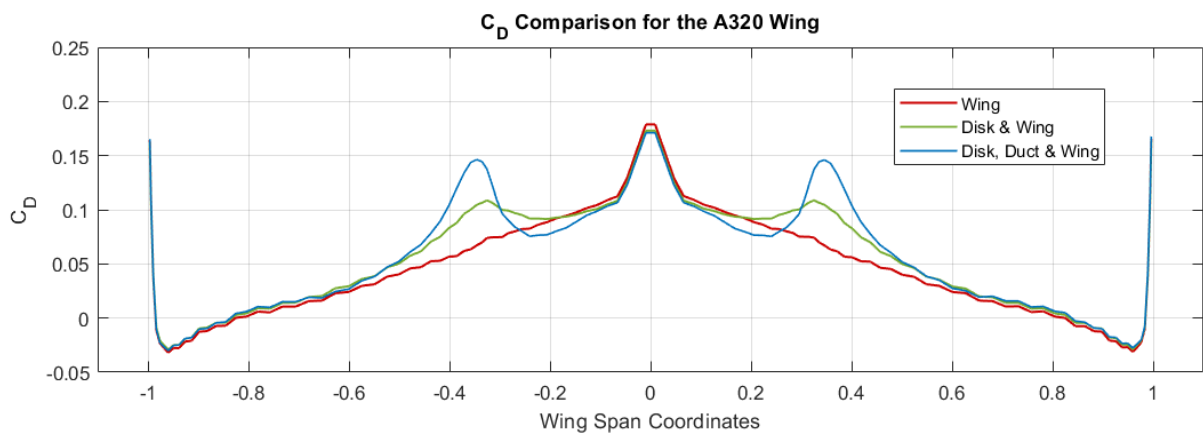


Figure 5.3 Graphical representation of the drag coefficient results of the Base Case.

When it comes to analyze the lift generated, the geometry without disks and ducts is the one that provides better results as shown in the Figure 5.4. It can be observed that, similar to the drag coefficient, the addition of disks or ducts leads to a reduction in lift. This decrease is a result of the impact of the flow generated across the wing, which subsequently elevates the pressure on the upper wing surface.

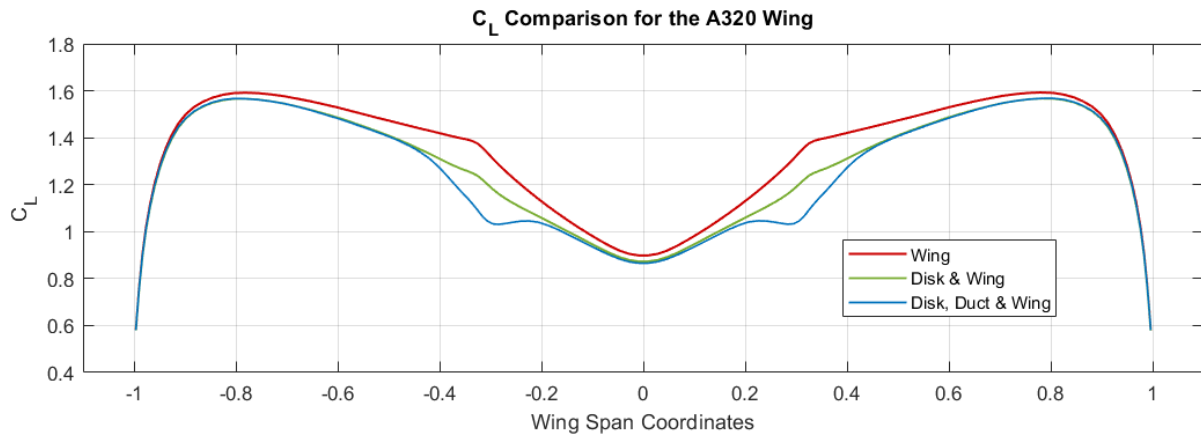


Figure 5.4 Graphical representation of the lift coefficient results of the Base Case.

The pressure coefficient has been analyzed for all the simulations in the section of the wing where the engines are situated to appreciate better the effects on it. The best results in this case are the ones for the wing itself, then the wing with the disks and finally the wing with the ducts.

In the Figure 5.5 the upper part of the graph is equivalent to the results of the bottom surface of the wing, as the pressures are higher and positive, and the lower part is equivalent to the upper part, as the pressures in that area are negative. Once this is clarified we can proceed to the analysis. The main differences are shown on the pressures of the higher part of the wing. We can see that the pressures of the wing without disks or ducts are lower than in the other cases. This is caused because when we add the disks the flow is deflected towards the lower surface of the wing, reducing the pressures on the upper surface. This effect becomes more evident when adding the ducts because the geometry helps redirect the flow through them, reducing even more the effect of the pressure on the upper part of the wing. Also, the pressures on the tip of the lower part of the wing are slightly higher both for the cases with only disks and disk and ducts. This is because despite the redirection of the flow reducing pressures above, the increase in flow underneath leads to slightly higher pressures in that area.

Also, when aiming to enhance the aerodynamic performance of a wing, the objective is to reduce pressure on the upper side while increasing it on the lower side, thereby boosting lift. However, in this scenario, lift in this area diminishes and drag increases significantly. This is likely attributed to the turbulence created at the trailing edge due to the disks and the drag generated by the ducts.

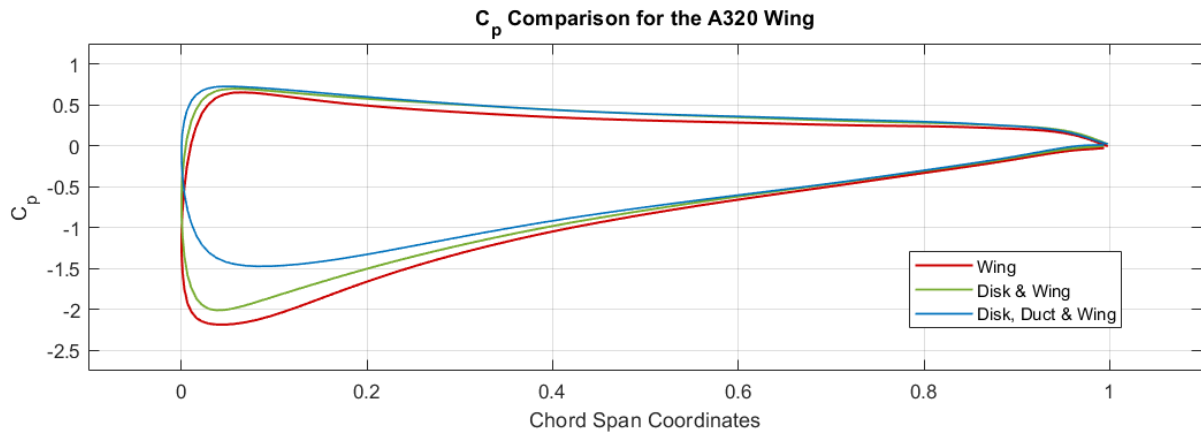


Figure 5.5 Graphical representation of the pressure coefficient results of the Base Case.

Aerodynamic Results

Respecting to the aerodynamic results, the wakes generated by the wing are the smoothest ones as expected since there is no element of any kind disturbing them such as the disks or the ducts (see Figure 5.6). It is possible to see the vortex generated in the tip of the wings, this happens because in this analysis no winglets to prevent it were used, causing a higher induced drag on this area.

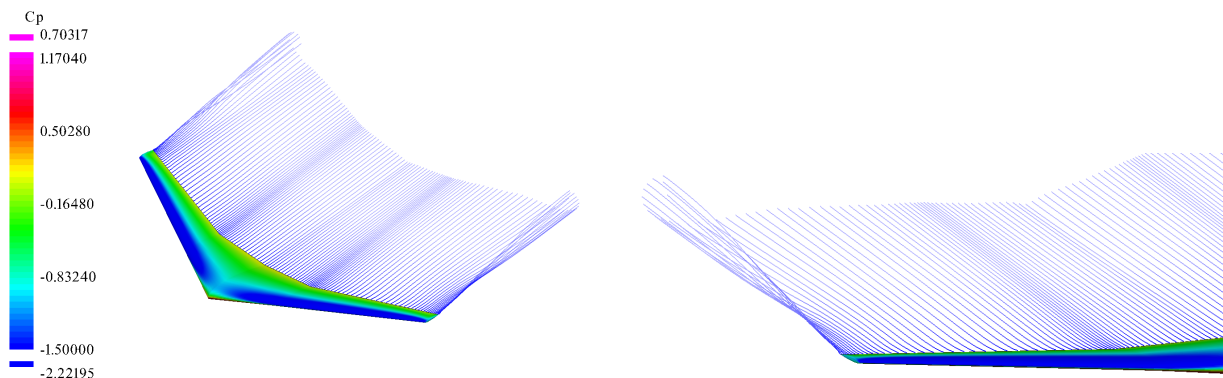


Figure 5.6 Base Case aerodynamic results for the wing case.

When adding the disks to the geometry it is possible to start seeing some perturbations on the wakes of the wing but not as many as the ones generated by the disk & duct distribution (see Figures 5.7 and 5.8). The effect of the tip vortex is going to be in almost all of the results obtained of this document.

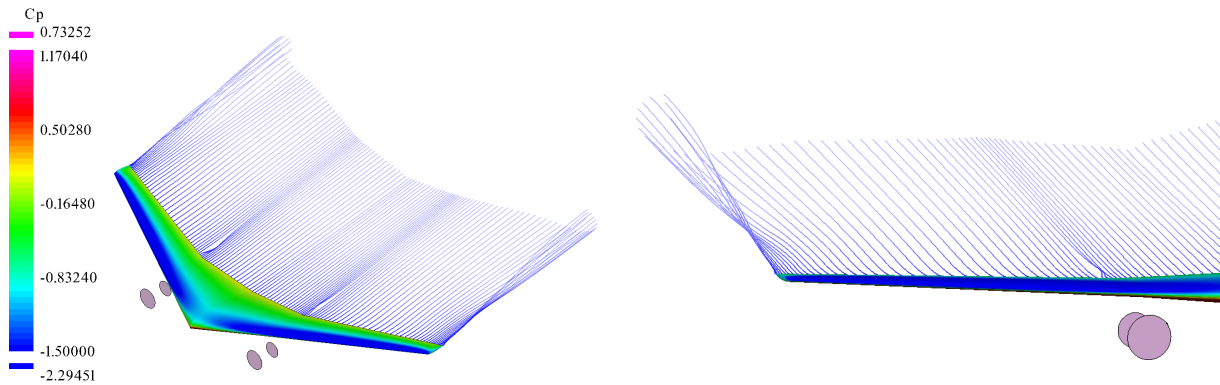


Figure 5.7 Base Case aerodynamic results for the disks & wing case.

The wakes generated by the ducts strongly affects the wakes generated by the wing, generating some vortices that rotates with the same direction as the disks. Figure 5.8 also shows the effect of the ducts on the pressure coefficient of the wing previously mentioned in the numerical results of this chapter, which is smaller in the upper surface than the other two cases.

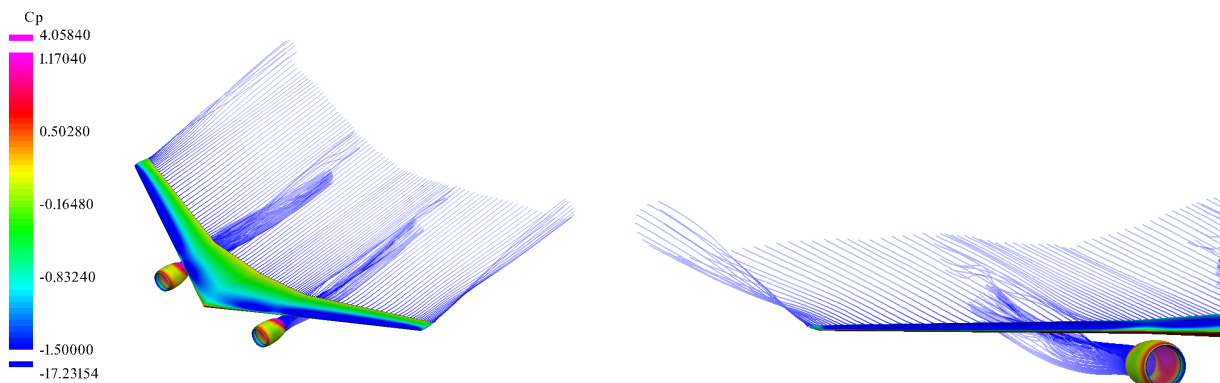


Figure 5.8 Base Case aerodynamic results for the disks, ducts & wing case.

5.2 Engines Above

The first engine distribution to analyze is the one with the engines above the wings. This kind of configuration has already been made, with models such as the HA-420 HondaJet (Wikipedia 2023f), which is a small corporate jet, the VFW 614 (Wikipedia 2023m), which was a regional airliner or the Beriev Be-200 (Wikipedia 2023c), which is a multirole amphibious aircraft. In this chapter we are going to analyze how having the engines in that position affects the aerodynamics of the A320.



Figure 5.9 VFW 614 (Jonsson 2000).

There are also some studies where this over-wing configuration is analyzed. In (Bolsunovski 2023) and (Bolsunovski 2019) it is possible to observe a couple of noise analysis where this configuration is used. Noise is one of the main issues when it comes to design an aircraft and with the actual tendency of creating engines with a higher bypass ratio it is more difficult to accommodate them under the wing. Using an over-wing-engine distribution to solve this problem is what has been analyzed in this studies.

Geometries

In the Figure 5.10 we can see the distribution for this case, where the engines are situated at the same distance of the center as the base case, which is 5.755 meters, but instead of being underneath the wing they are above it, maintaining all the other characteristics the same as the previous case.

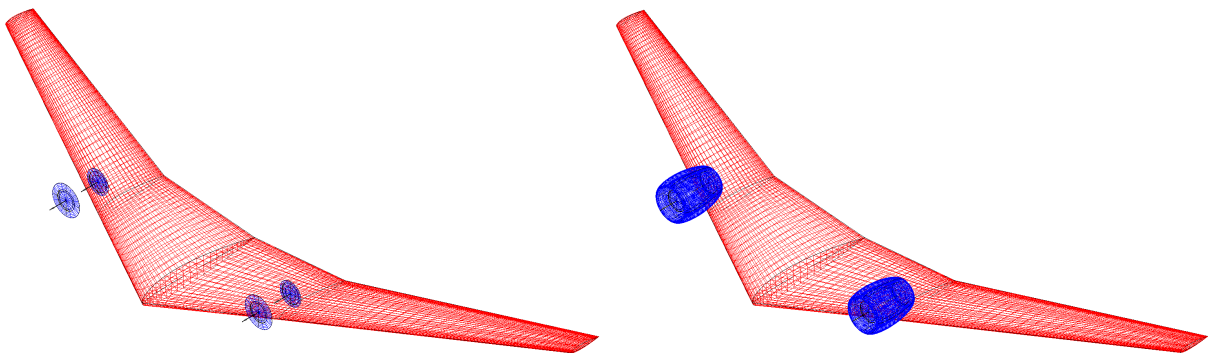


Figure 5.10 Engines Above geometries. From left to right: wing & disks case and wing, disks & ducts case.

Numerical Results

Continuing with the numerical results, in the Figures 5.11 and 5.12 the drag coefficient of the disks and the disks and ducts, respectively, for the engines above case compared with the base case results are shown. Starting with the wing and disk, we can observe that having the disks above the wing generates less drag than having them below it (see Figure 5.11). This is probably caused by the fact that when the disks are situated on the upper part of the wing of the wing, they help accelerate the flow on that surface, causing wakes to adhere to it, which delays flux shedding at high angles of attack, reducing this way the induced drag.

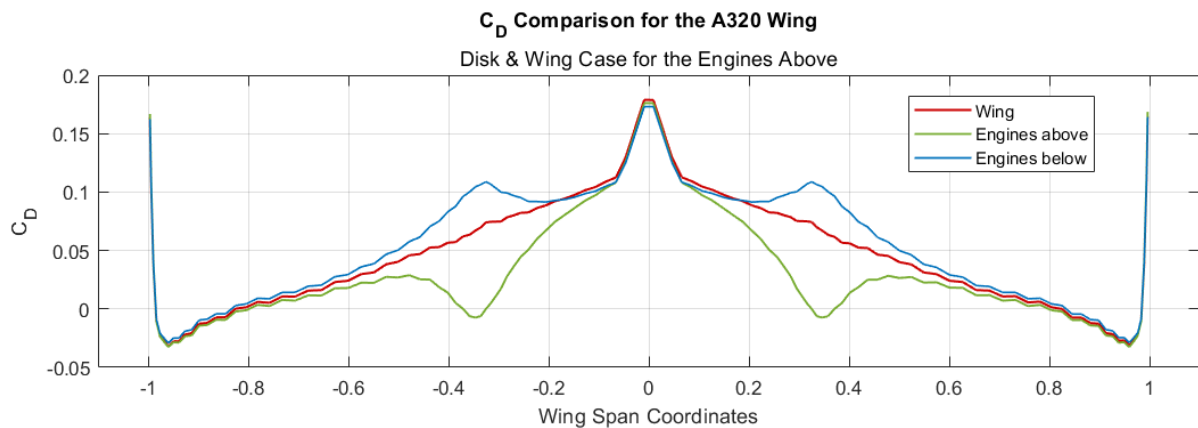


Figure 5.11 Graphical representation of the drag coefficient results of the Engines Above for the disks & wing case.

When analysing the ducts something similar to the disk and wing case happens. In the Figure 5.12 we can see that having the engines above the wing also helps with the drag when compared with having the engines below the wing, although the values are higher than in the previous case because the geometry of the ducts generates induced drag.

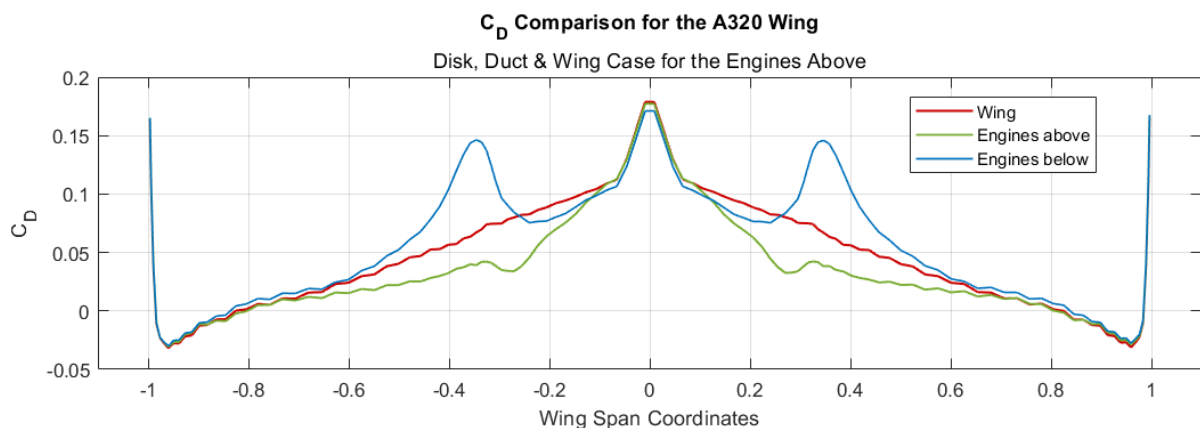


Figure 5.12 Graphical representation of the drag coefficient results of the Engines Above for the disks, ducts & wing case.

In the case of the lift distribution using only disks, the results of the engines above the wing are still better than the ones given by the engines below the wing, providing a higher lift in all of the wingspan, as shown in the Figure 5.13.

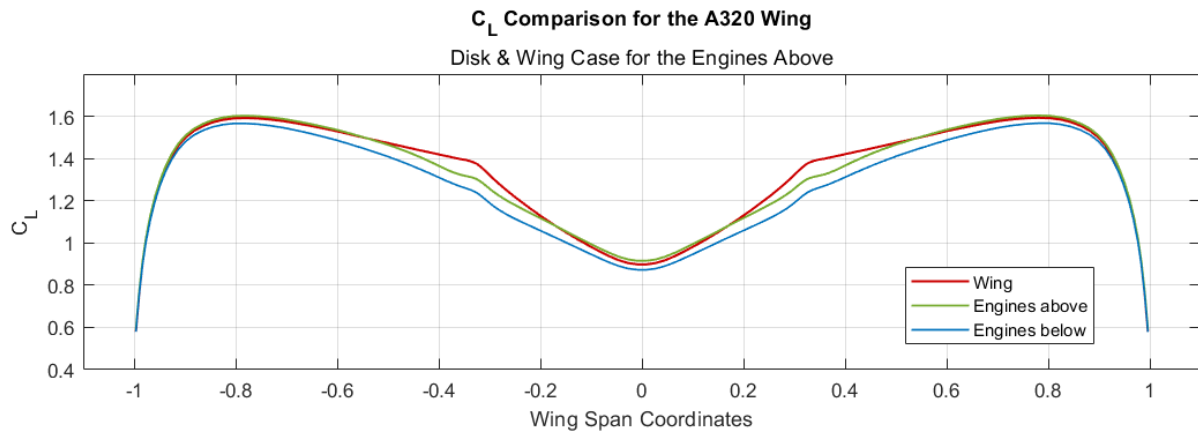


Figure 5.13 Graphical representation of the lift coefficient results of the Engines Above for the disks & wing case.

However, for the results when using ducts, even though the performance is not as efficient as the previous case, it still presents advantages. In the outer area of the wing, the lift is slightly lower than in the case of just disks, nonetheless, in the inner area, it is even greater than the case of the wing alone due to the influence of the wakes generated by the ducts as shown in the Figure 5.14.

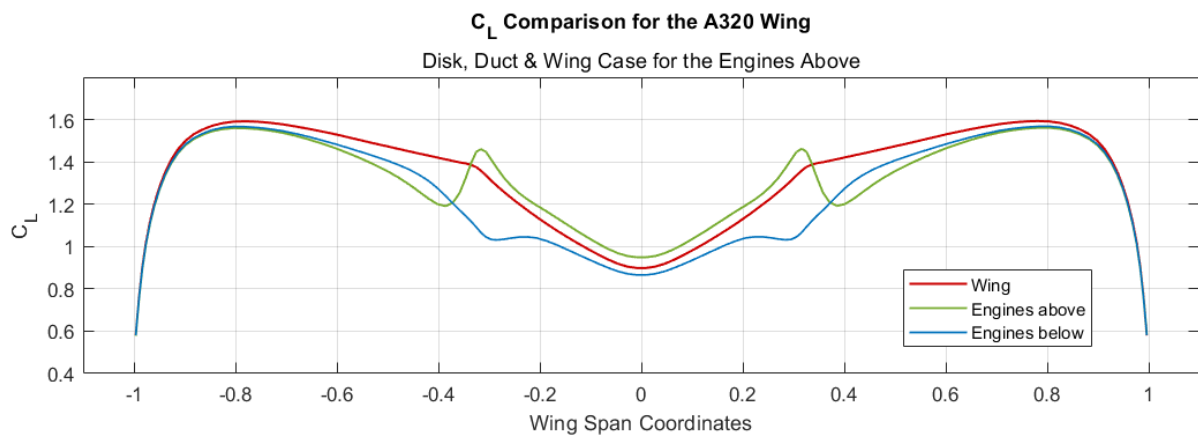


Figure 5.14 Graphical representation of the lift coefficient results of the Engines Above for the disks, ducts & wing case.

Moving on to the results of the pressure coefficient distribution, in the case of just wing and disks, there are hardly any variations. It can be observed from Figure 5.15 that on the wing's upper side, the pressures for the engines above are slightly higher than in the other case. As explained in Chapter 5.1, with the disks positioned beneath the wing, the flow is diverted, increasing the pressures in the upper side of the wing, meanwhile when the disks are situated on the top the flow is not diverted and the turbulence generated in that area due to the high angle of attack of the analysis is delayed, thus resulting in lower pressures.

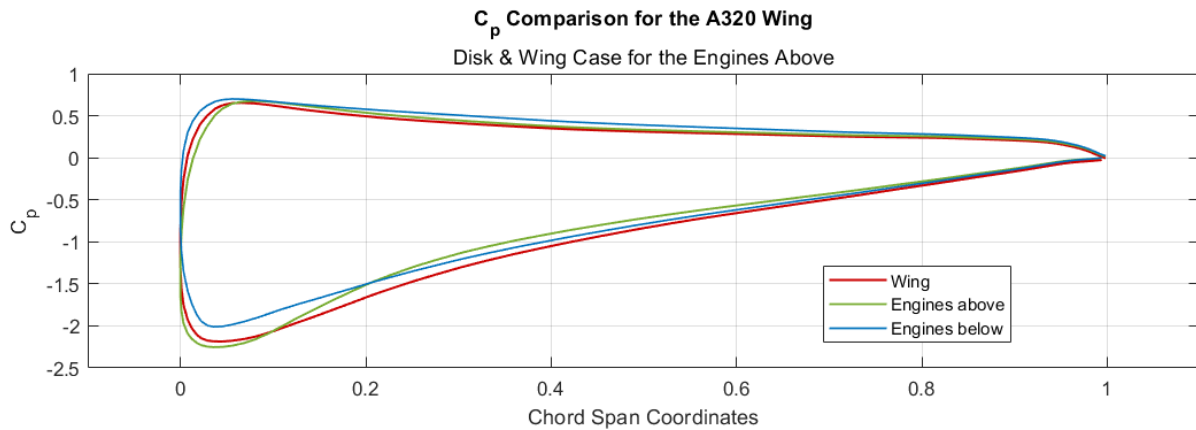


Figure 5.15 Graphical representation of the pressure coefficient results of the Engines Above for the disks & wing case.

When the ducts are added, the results change drastically, as shown in the Figure 5.16. The main difference observed when we compare this results with the ones obtained from the only disks case is that we can see that the numbers from the wing and the engines above are very similar, with the difference that when we have an accelerated flow in that area, the pressures in the center of the chord are slightly reduced. The wakes generated by the geometry of the ducts affects a lot more on the aerodynamics than when only the disks are used, this can be seen in the Figure 5.18 from the aerodynamic results chapter.

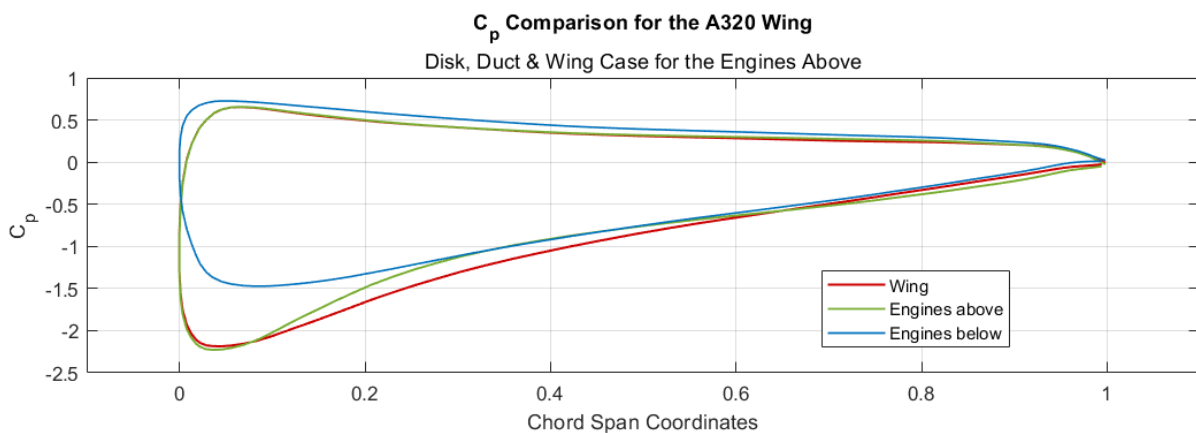


Figure 5.16 Graphical representation of the pressure coefficient results of the Engines Above for the disks, ducts & wing case.

Aerodynamic Results

In the aerodynamic results of the Figures 5.17 and 5.18 is possible to see the influence of the wakes generated by the disks and the duct geometries. While the disks only create a jump in the flow conditions where they are placed, the ducts, being treated as surfaces in the program, generate wakes derived from them, also considering that jump in the flow conditions generated by the disks. In this way, a result more closely resembling what would occur in reality is obtained.

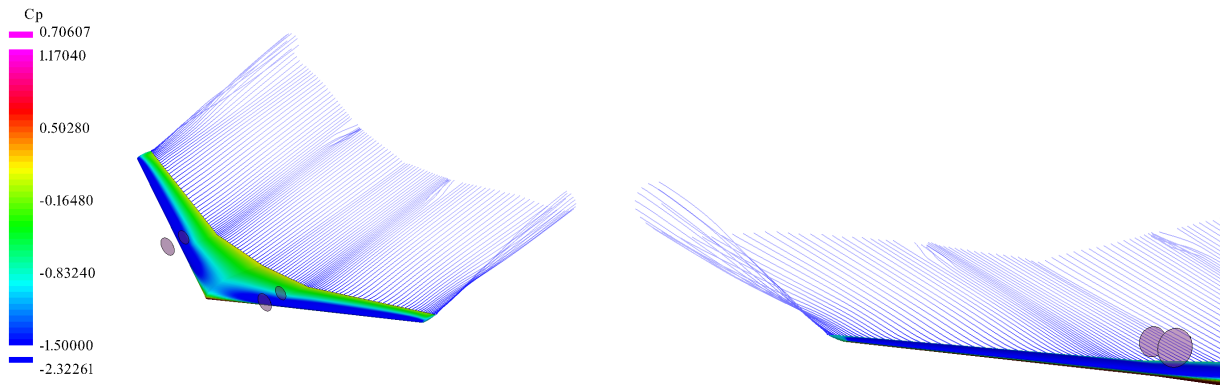


Figure 5.17 Engines Above aerodynamic results for the disks & wing case.

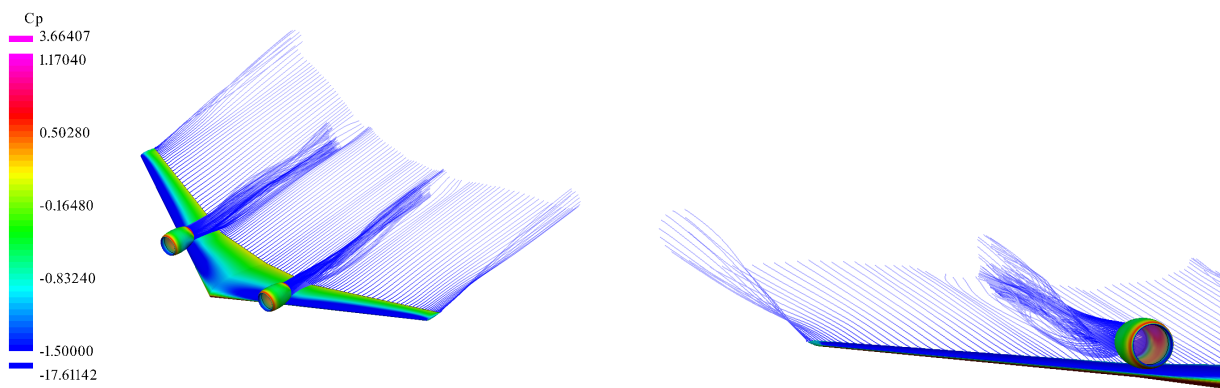


Figure 5.18 Engines Above aerodynamic results for the disks, ducts & wing case.

5.3 More Engines

In this chapter we are going to analyze two different distributions, one with four engines and another one with six engines distributed along the wingspan. Just like in the previous case, this type of distribution has been previously used in other types of aircraft. In the case of aircraft with four engines, there are the Airbus A380, a sibling model of the one being analyzed (Wikipedia 2023a), and the Boeing KC-135, an American military aerial refueling tanker aircraft. When talking about aircraft with six engines, there aren't too many precedents. Nevertheless, the Antonov An-225 Mriya (Wikipedia 2023b) existed, which was originally developed during the 1980s as an enlarged derivative of the Antonov An-124 airlifter for the express purpose of transporting Buran-class orbiters.



Figure 5.19 From Left to Right: Airbus A380 (Modla 2023) & Antonov An-225 Mriya (Steven 2012).

In the work by (de Vries 2021) an experimental investigation of the aerodynamic interaction that occurs between distributed propellers in forward flight is described. Here, different positions between the different propellers and its interaction is analyzed in order to study their performance, flow-field characteristics and noise production.

Geometries

The geometries analyzed in this chapter are shown in the Figures 5.20 and 5.21. A feature to know before going into detail is the position on the engines. In both the four and six engine distributions the first pair is situated at the same position as the base case. Then, the second pair of the four engine distribution is situated at 11.414 meters from the center of the wing while for the six engine distribution the second and third pairs are on the sections situated at 9.572 and 13.300 meters from the center of the wing.

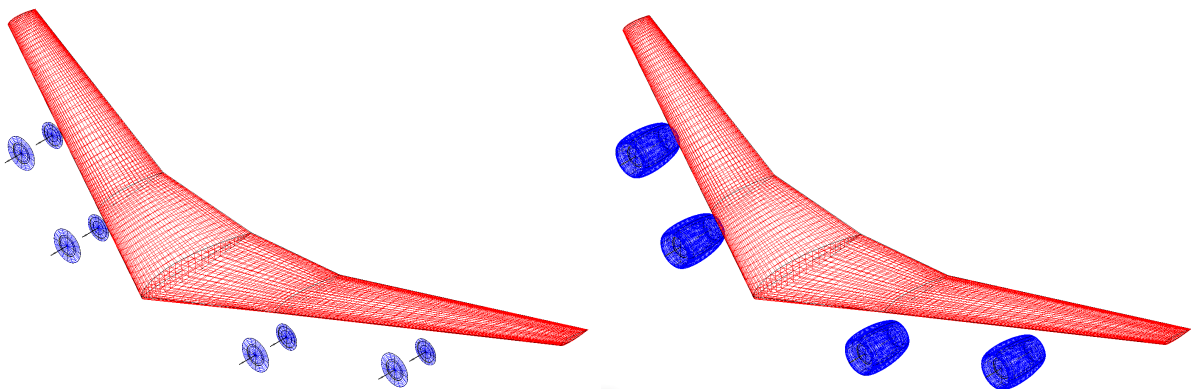


Figure 5.20 Four engines geometries. From left to right: wing & disks case and wing, disks & ducts case.

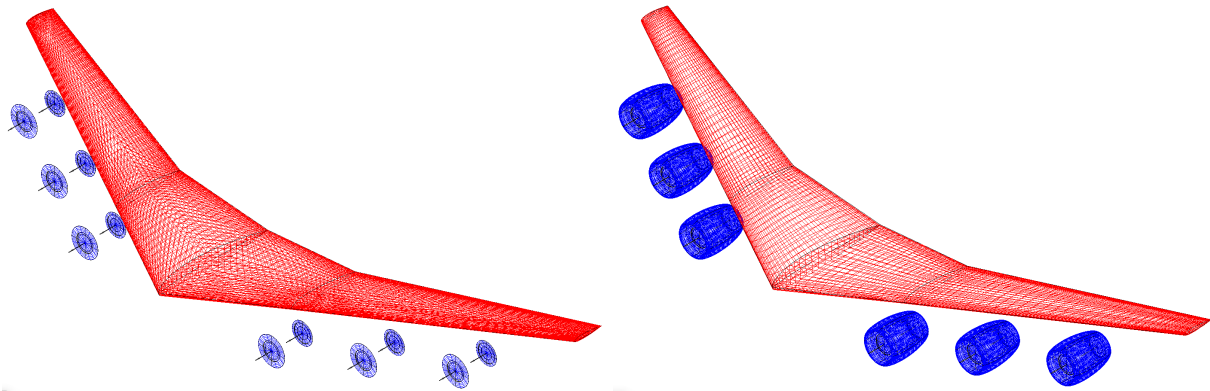


Figure 5.21 Six engines geometries. From left to right: wing & disks case and wing, disks & ducts case.

Numerical Results

After analyzing the results obtained from the base case of the Chapter 5.1 with two engines beneath the wing, it is easy to deduce the outcomes of this analysis. Nonetheless, the influences of adding more engines will be examined and assessed anyways when using VSPAero. Beginning with the drag distribution for the case with the wing and the disks (see Figure 5.22), it is very clear how the disks influence the appearance of drag in the positions where they are situated because of the flow distortion generated on the wakes of the wing, which increases the induced drag.

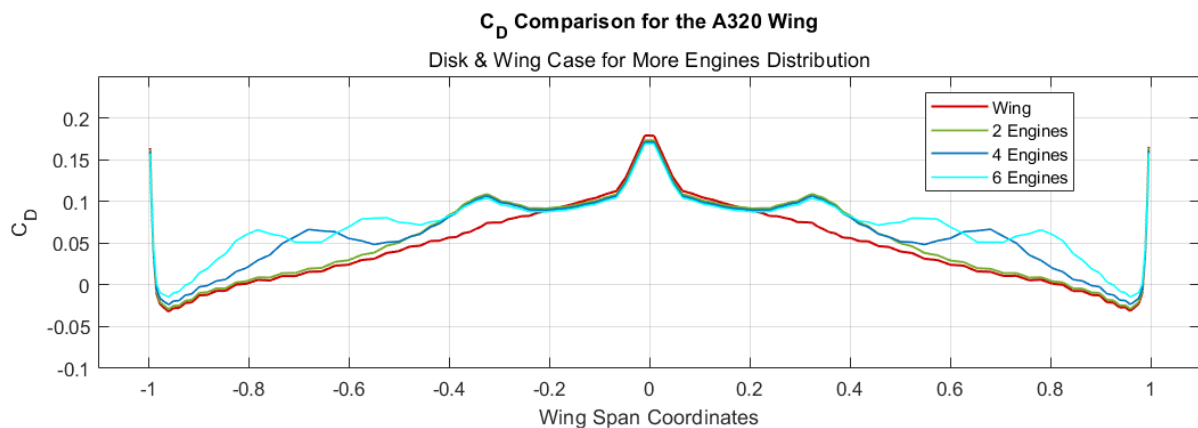


Figure 5.22 Graphical representation of the drag coefficient results of the More Engines distributions for the disks & wing case.

In the results of the duct analysis shown in Figure 5.23, the same phenomenon but increased is observed in the area where the ducts are located as in the base case. In each of the sections where the engines are situated, whether it's two, four, or six engines, there are drag peaks caused by the influence of the wakes generated by the ducts on the wing. A notable difference in the geometry with six engines is that, due to the engines being positioned closer together, the flows generated by them interact with each other, causing an increase in the induced drag not only in the engine sections but across the entire wingspan as well.

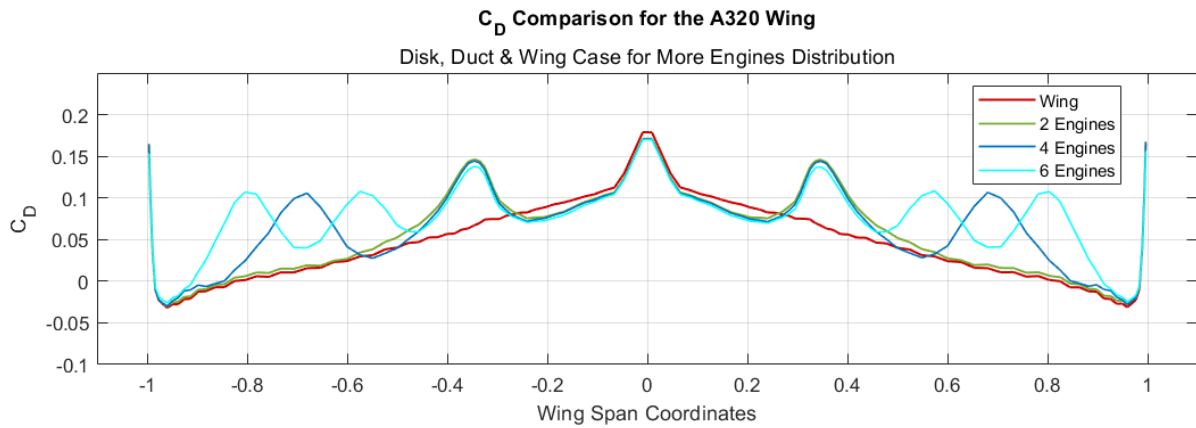


Figure 5.23 Graphical representation of the drag coefficient results of the More Engines distributions for the disks, ducts & wing case.

Regarding the lift coefficient distribution without ducts shown in Figure 5.24, up to the zone where the first engine is located the lift conditions remain constant from one case to another. However, as more engines are added, the lift decreases considerably as expected, having this small drops in the sections where the engines are positioned.

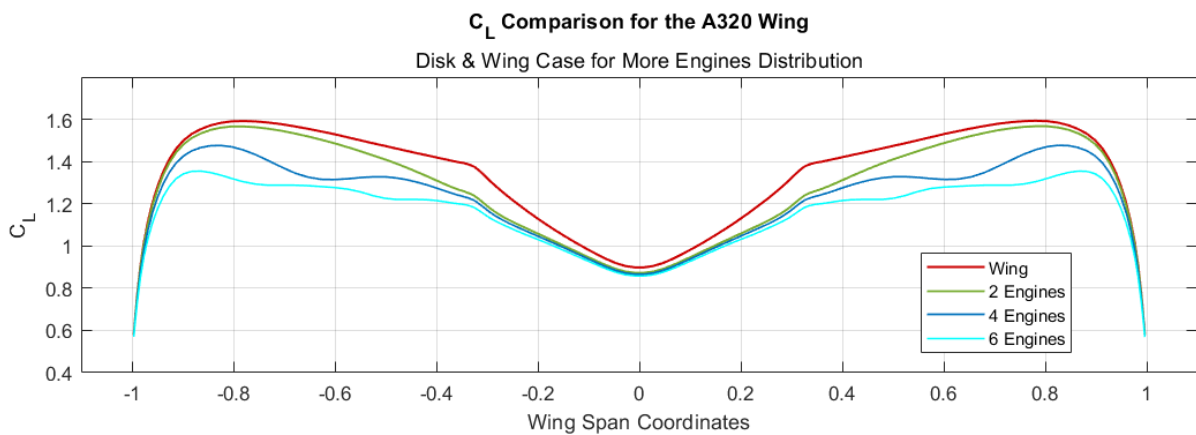


Figure 5.24 Graphical representation of the lift coefficient results of the More Engines distributions for the disks & wing case.

In Figure 5.25, the lift coefficient results for the case with ducts are depicted. Similar to the drag observations, downward peaks appear at the locations where the engines are positioned. Furthermore, as anticipated, the lift significantly decreases across the rest of the wing as more engines are introduced. This behavior is consistent with the expected impact of additional engines on the overall lift distribution.

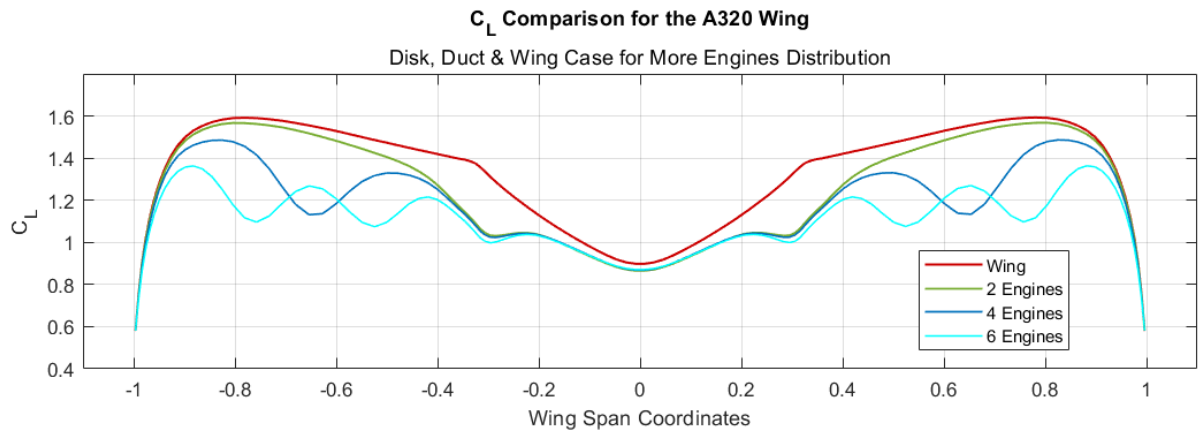


Figure 5.25 Graphical representation of the lift coefficient results of the More Engines distributions for the disks, ducts & wing case.

The pressure distribution results are the ones relative to the section ± 0.35 and they are nearly identical to those of the base case (see Figures 5.5 and 5.26). Since all engines have the same geometric and configuration characteristics, and there is minimal interaction between the wakes generated by the other engines with the first one (as observed in Figures 5.22 and 5.24 for drag and lift coefficients), it is anticipated that the results would exhibit a high similarity among them. The same effect of having a reduced pressure on the upper side of the wing caused by the deflection of the flow and the appearance of higher values of turbulence develops.

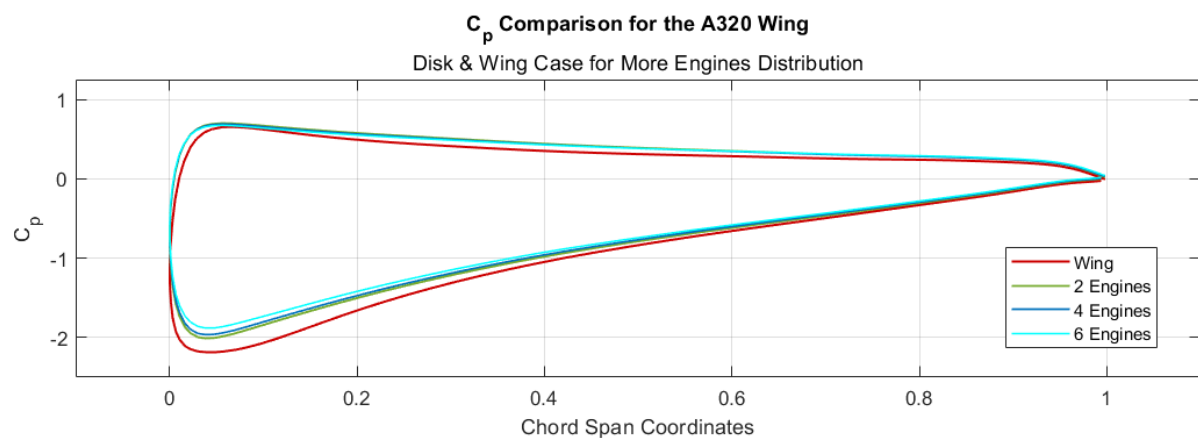


Figure 5.26 Graphical representation of the pressure coefficient results of the More Engines distributions for the disks & wing case.

The same scenario unfolds when the ducts are added to the geometry (see Figures 5.5 and 5.27). The pressure distribution in the area remains nearly the same, whether there are two, four, or six engines, as the base case when considering the ducts. Placing the engines beneath the wing reduces the pressure generated on the upper side at high angles of attack due to the high turbulences created by the wakes of the ducts.

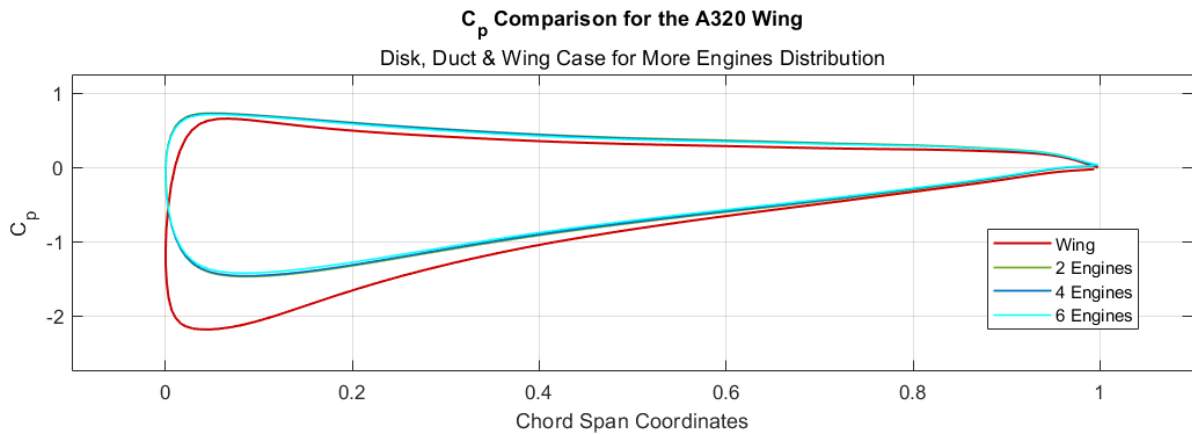


Figure 5.27 Graphical representation of the pressure coefficient results of the More Engines distributions for the disks, ducts & wing case.

Aerodynamic Results

Turning to the aerodynamic results, when there are four engines, as seen in the cases presented in Figures 5.28 and 5.29, distortions in the wing wakes understandably intensify. When only the disks are present, not many disturbances can be observed, but when we introduce the ducts, comparable to the preceding cases, the wakes generated by them produce a significantly greater influence on the wing wakes. This interaction results in the generation of vortices, increasing drag and thus reducing lift.

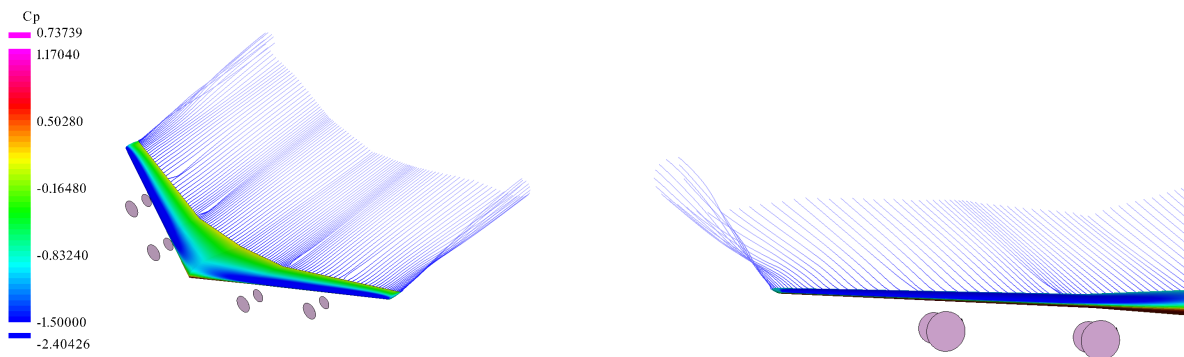


Figure 5.28 Four engines aerodynamic results for the disks & wing case.

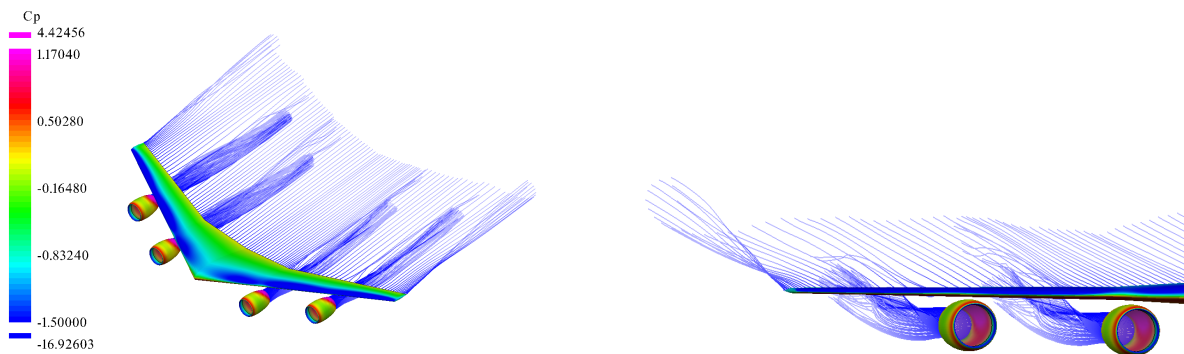


Figure 5.29 Four engines aerodynamic results for the disks, ducts & wing case.

A similar scenario appears when employing six engines. In Figures 5.30 and 5.31, it becomes evident that when only the disks are in use, the disturbances in the wing's flow are minimal. However, with the introduction of the ducts, these disturbances significantly increases. Moreover, in this case, a greater distortion in the wing's wakes is observable due to the presence of these geometries. This effect is also reflected in the drag and lift coefficient results showed in the previously mentioned Figures 5.23 and 5.25, respectively.

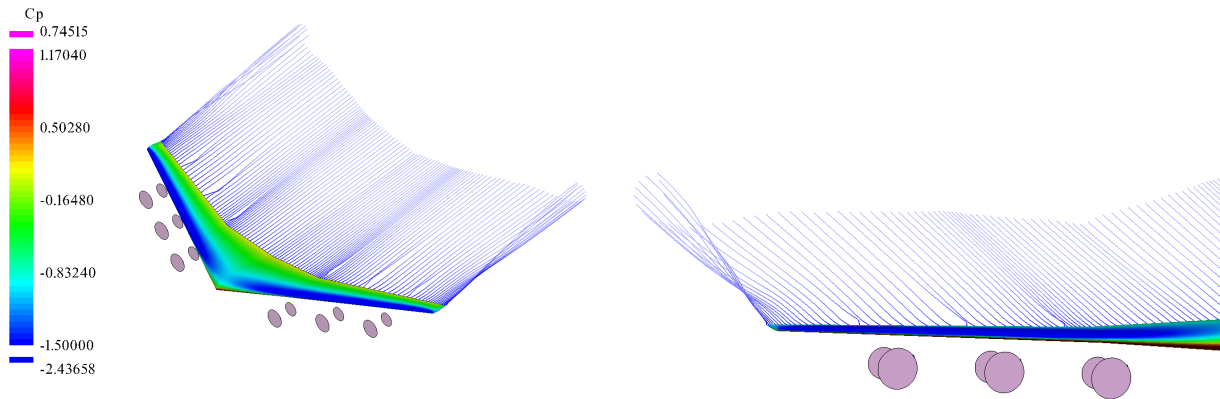


Figure 5.30 Six engines aerodynamic results for the disks & wing case.

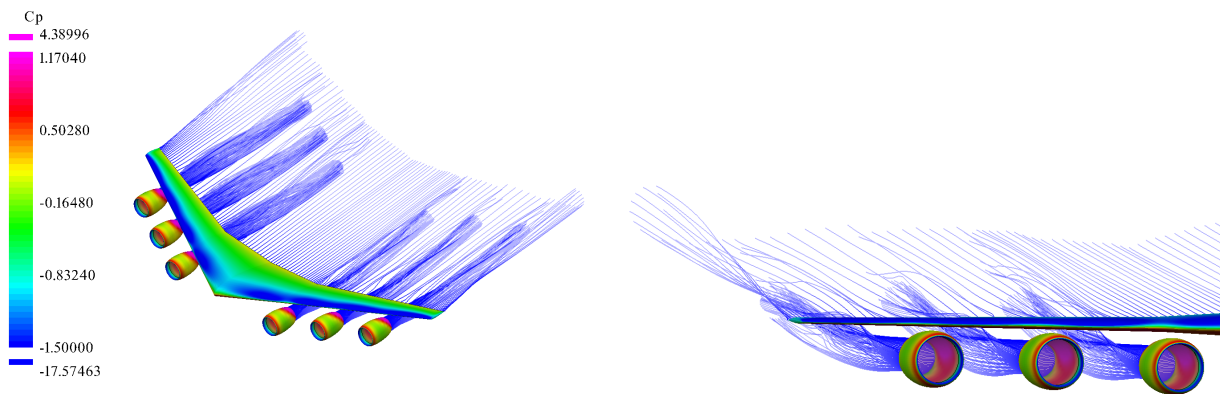


Figure 5.31 Six engines aerodynamic results for the disks, ducts & wing case.

5.4 Tip Engines

In this chapter, we will talk about three distinct engine distribution configurations in the wing-tips. The first geometry has the engines below the wingtips (see Figure 5.33), the second one has the engines in front of the wingtips (see Figure 5.34), and the last one has the engines above of the wingtips (see Figure 5.33). Just as in the previous case, some of these engine distributions have been adopted in various aircraft designs, some examples with engines in that area are the SNCASO SO.9000 Trident (Wikipedia 2023i), mixed-power interceptor aircraft, and the Tsybin RSR (Wikipedia 2021), a strategic reconnaissance aircraft. Another special aircraft not only with engines above of the tips but with four engines is the Myasishchev M-50, a strategic bomber prototype from the Soviet Union (Wikipedia 2023i).

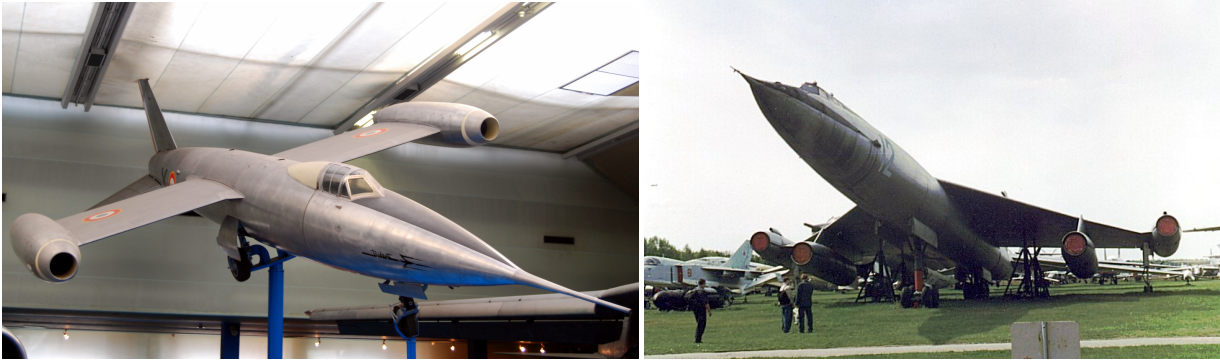


Figure 5.32 From Left to Right: SNCASO SO.9000 Trident (Turner 2012) & Myasishchev M-50 (Wikipedia 2009).

In the paper by (Sinnige 2019) presents an aerodynamic analysis of the propeller–wing interaction effects for the wingtip-mounted propeller configuration, including a comparison with a conventional configuration with the propeller mounted on the inboard part of the wing. The main purpose is to analyze if this configuration decreases the induced drag by attenuating the wingtip vortex by the propeller slipstream.

Geometries

As mentioned before, in this case we are going to analyze the geometries from the Figures 5.33, 5.34 and 5.35, with the engines on the tips of the wing. All the engines in this section are positioned at the wingtips, at a distance of 16.970 meters from the center of the wing, but at different heights relative to it. The case with engines in front of the wing will serve as the reference for defining the heights, given that its center is located at the wingtip itself. With this in mind, both the case with engines beneath and above the wingtips will be positioned at a distance of 1.100 meters, respectively.

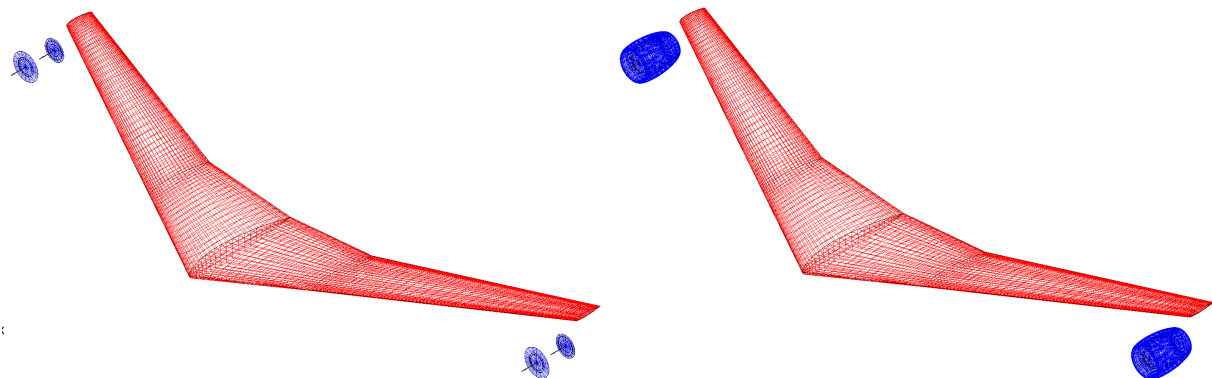


Figure 5.33 Engines below the tips geometries. From left to right: wing & disks case and wing, disks & ducts case.

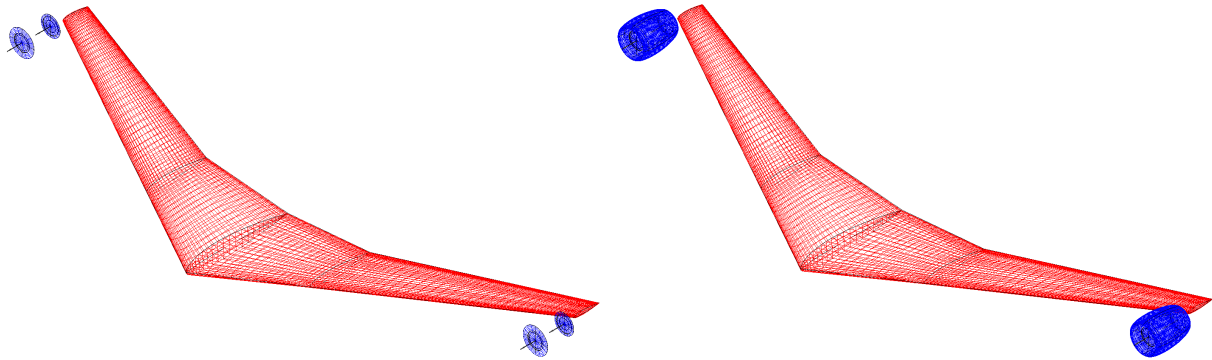


Figure 5.34 Engines in front of the tips geometries. From left to right: wing & disks case and wing, disks & ducts case.

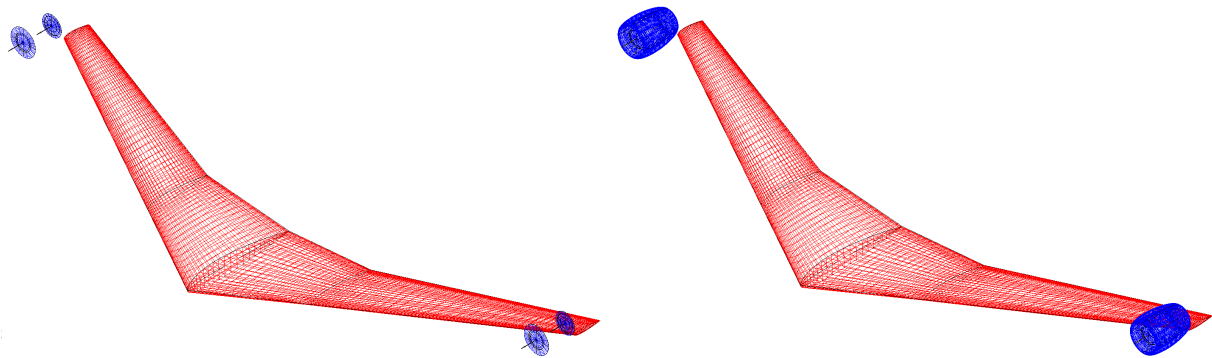


Figure 5.35 Engines above the tips geometries. From left to right: wing & disks case and wing, disks & ducts case.

Numerical Results

This case is particularly interesting because as we are going to examine how the wingtip vortices of the wing are going to be affected by having the engines in those positions. Furthermore, it's important to highlight that in this section it won't be possible to make an analysis of the pressure coefficient distribution. The engines being positioned precisely at the wingtip causes issues for VSPAero to interpret results in that area, leading to inconclusive outcomes as the section is almost a line and analyzing the same section as the previous results doesn't make sense as it doesn't give any relevant information about how the engines affect the wing.

In the Figure 5.36 we can see the initial results of this analysis, focusing on the drag coefficient distribution when only the disks are present. A notable observation from the graph is the high drag peak at the wingtips when the engines are placed directly in front. This happens because the wings are suffering the direct impact of the airflow generated by the disks, increasing the drag in that area. Continuing with the configuration with the engines underneath, the induced drag decreases, reaching a point where it becomes negative at its minimum, favoring thrust. In this case, the distorted flow of the disks due to its rotational direction promotes the dispersion of the wingtip vortices, reducing the induced drag in that area. Nevertheless, this effect is punctual since there's a slight increase in the induced drag again at the wingtip because the pressures at that point are still very high due to the airflow hitting the wing (see Figure 5.40) . In the case of engines positioned above, the results are very similar to those of the wing without engines,

although slightly better in terms of drag generation. Despite the same rotational direction, being located above the wing delays the generation of these vortices, thereby reducing drag.

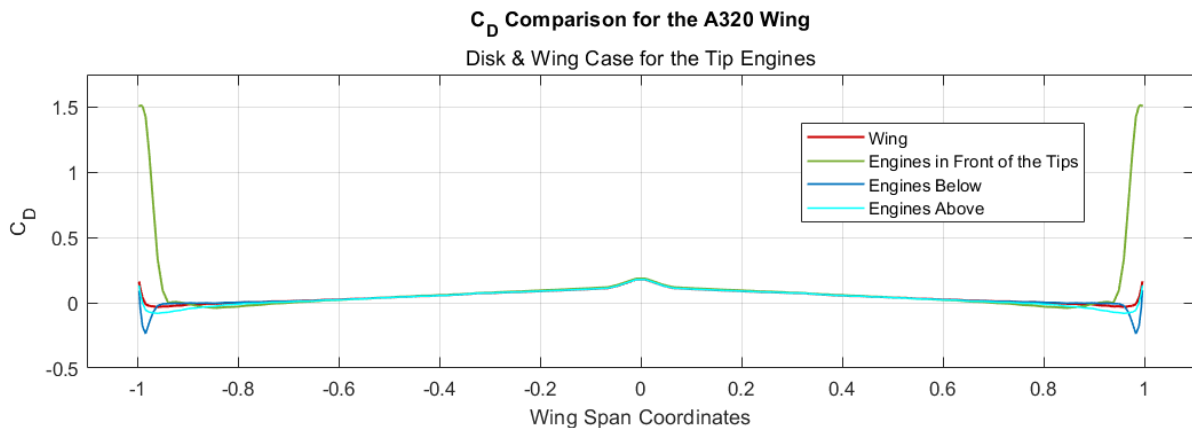


Figure 5.36 Graphical representation of the drag coefficient results of the Tip Engines distributions for the disks & wing case.

When introducing the ducts, the results remain quite similar to the previous cases, even though they're not identical. The first noticeable difference that can be seen in the Figure 5.37 is that all geometries have a slightly lower drag just in the area before the engine, particularly in the case of engines positioned in front. Furthermore, the engines in front of the wing cause a higher drag peak compared to the previous scenario, yet this drag decreases more rapidly than in the previous case in the area closest to the wingtip. In both the engines below and above configurations, the distribution closely resembles the case without ducts.



Figure 5.37 Graphical representation of the drag coefficient results of the Tip Engines distributions for the disks, ducts & wing case.

In the Figure 5.38 we can see the lift coefficient distribution when using only the disks. Just like the drag distribution graph, there is a heavy peak in the lift of the tips of the wing when the engines are placed in front of it. When the engines are placed directly in front of the wingtips, the appearance of vortices in that area is delayed. In the case of lift distribution this results in a reduction of the recirculation from the wing's underside to its upper side at the tips, leading to an increase in lift. For the engines below we find a drop in the lift values at the same position

where the drag starts to increase due to the high pressure of the flow hitting the wing, causing a heavy lift loss at that point. Again, for the case with the engines above, the results are almost the same to the ones given by the base wing, also probably caused by the delay of the creation of the wingtip vortex coupled with the fact that, in this scenario, the flow generated by the engines doesn't directly impact the wing as in the other cases, resulting in less elevated pressures, consequently increasing lift at high angles of attack.

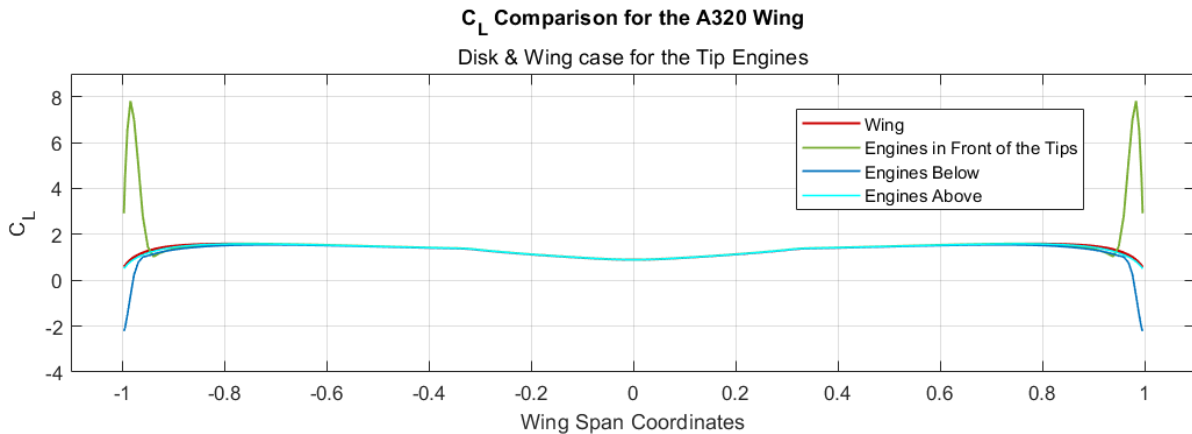


Figure 5.38 Graphical representation of the lift coefficient results of the Tip Engines distributions for the disks & wing case.

As seen in Figure 5.39, the most significant differences when using the ducts compared to the case with only disks are found in the peak values. For engines placed in front of the wing, the influence of the wakes of the ducts reduces this peak value by almost a 25%, while for engines positioned below, it slightly decreases at the tips. However, in the case of engines above, the values remain quite similar to those of the base case wing, and they are even slightly better in terms of lift.

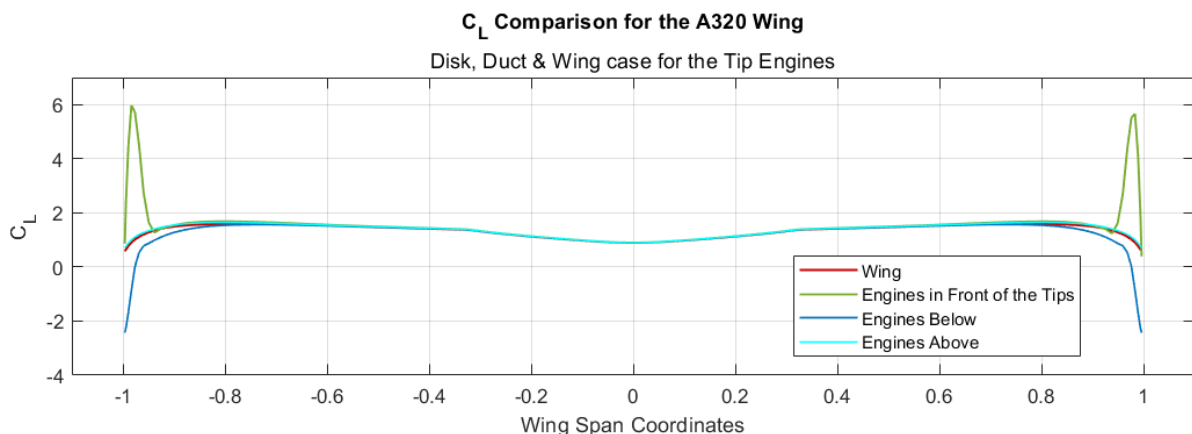


Figure 5.39 Graphical representation of the lift coefficient results of the Tip Engines distributions for the disks, ducts & wing case.

Aerodynamic Results

All these previously mentioned effects in the numerical results chapter regarding the wingtip vortices are exemplified in the images of this chapter. Starting with the case of engines positioned beneath the wing, in Figures 5.40 and 5.41, it is evident how, although the appearance of the vortex is delayed, the pressures on the lower side of the trailing edge are quite high due to the influence of the flow on that surface, caused by the angle of attack to which the wing is subjected.

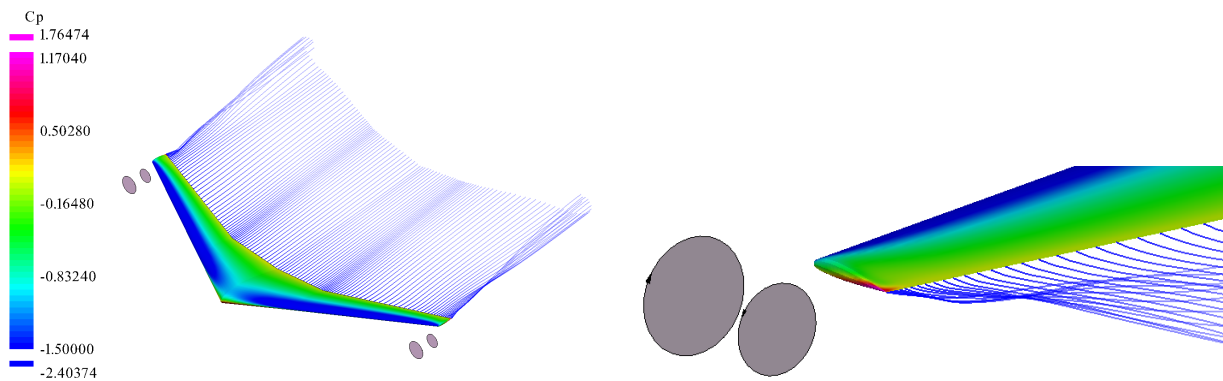


Figure 5.40 Engines below the tips aerodynamic results for the disks & wing case.

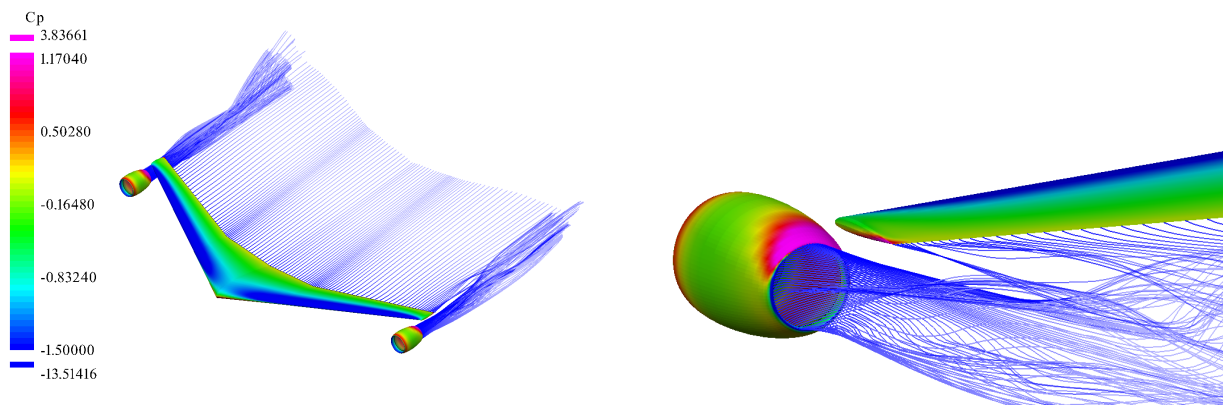


Figure 5.41 Engines below the tips aerodynamic results for the disks, ducts & wing case.

Moving on to the configuration with engines in front of the wingtips in Figures 5.42 and 5.43, it can be observed that the pressures in that wing region are very high due to the direct impact of the flow on the wing, leading to a considerable increase in the induced drag, as verified in the previous chapter.

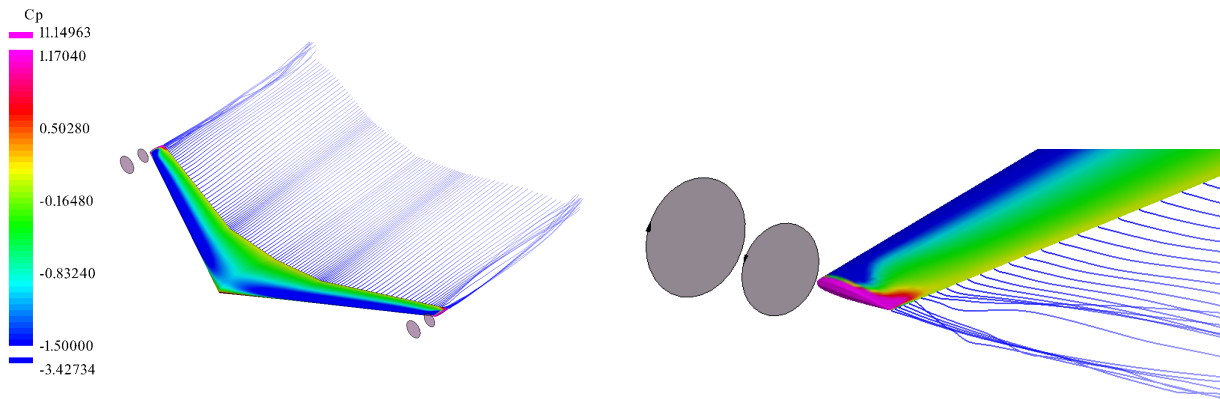


Figure 5.42 Engines in front of the tips aerodynamic results for the disks & wing case.

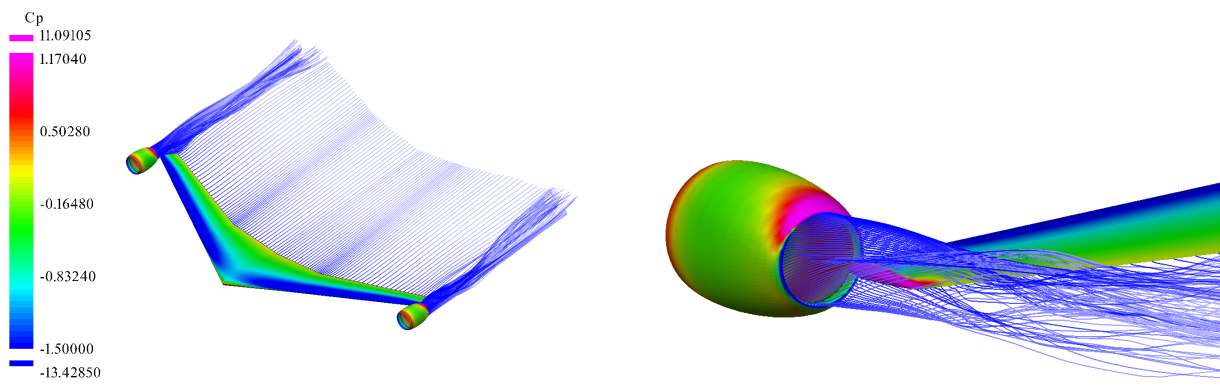


Figure 5.43 Engines in front of the tips aerodynamic results for the disks, ducts & wing case.

Lastly, in the case of engines above the wing in Figures 5.44 and 5.45, it can be seen that, for the chosen angle of attack in the simulation, these kinds of pressures at the wingtip do not happen as the flow does not directly hit the wing. However, it still influences the flow sufficiently to help delay the onset of wingtip vortices, thus improving lift in that area.

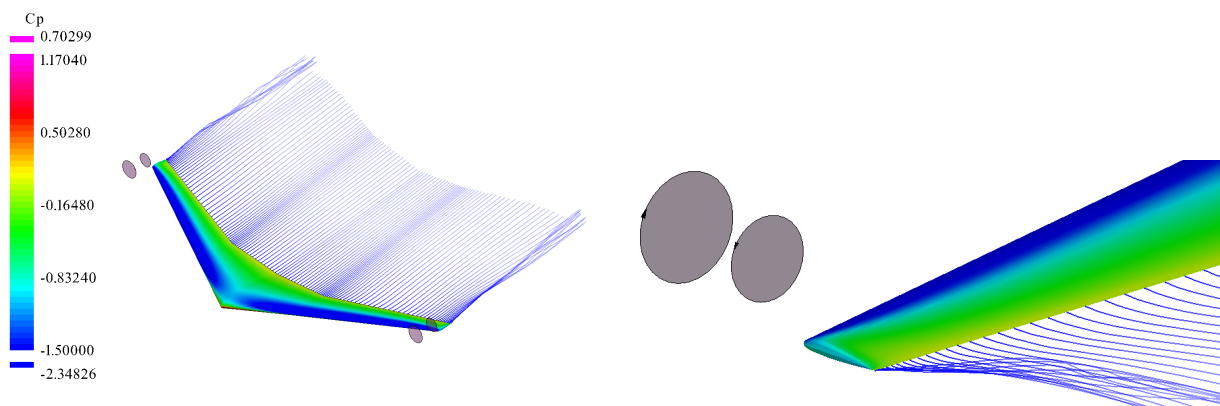


Figure 5.44 Engines above the tips aerodynamic results for the disks & wing case.

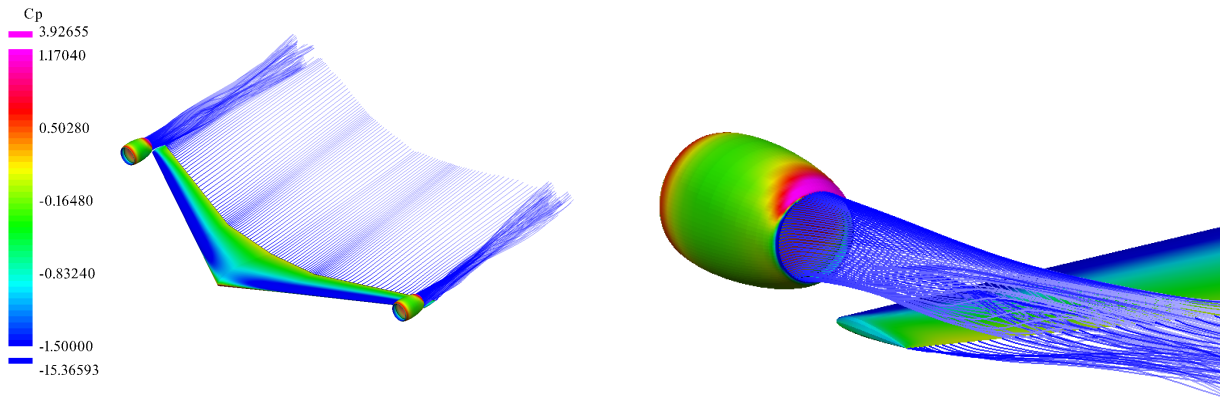


Figure 5.45 Engines above the tips aerodynamic results for the disks, ducts & wing case.

5.5 A320

In this chapter, we will explore how the wakes generated by the wing interact with the A320's tail, following the same approach as in the previous chapters. However, the focus will be only on the tail, as the results for the wing don't change and they were previously analyzed.

Geometries

Figures 5.46 and 5.47 display the complete geometries of the Airbus A320 with the base case configuration. The properties of the tail geometry are shown in the Tables 4.3 and 4.4 of the Chapter 4.1.2. The tail is positioned approximately 16 meters from the main wing. Moreover, since we are exclusively analyzing the effects on the horizontal tail, pressure coefficient calculations will be conducted at the section located 5.000 meters from its center, which when translated into a dimensionless position, it would be equivalent to ± 0.8 .

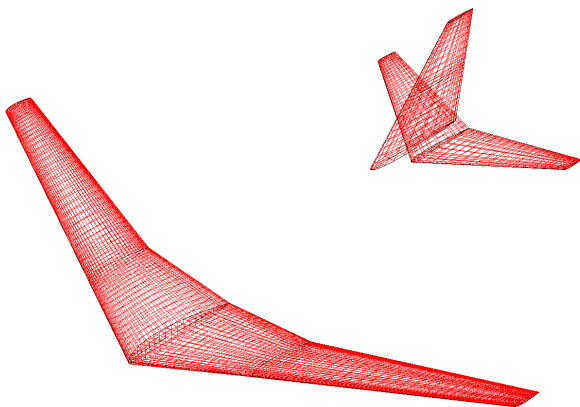


Figure 5.46 A320 wing and tail geometries.

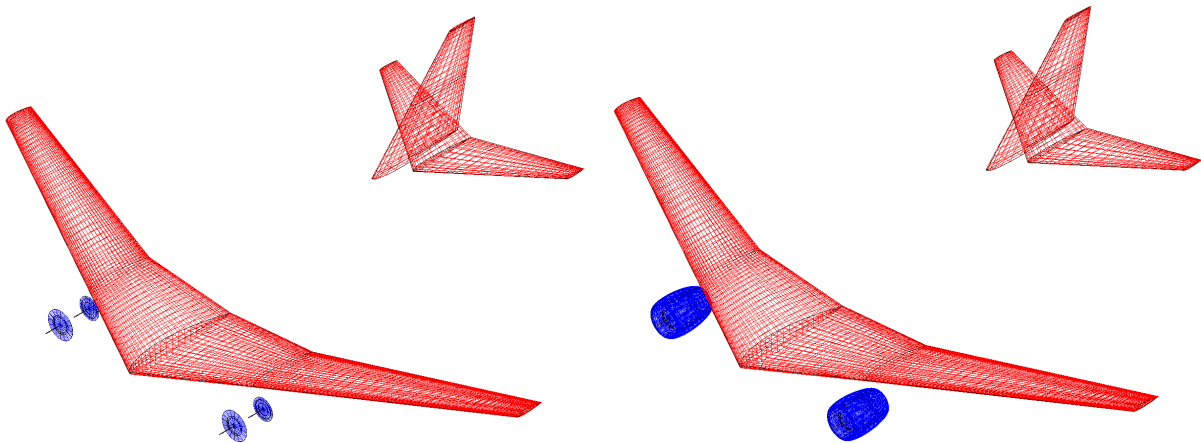


Figure 5.47 Wing and tail geometries. From left to right: wing disks case and wing, disks ducts case.

Numerical Results

Continuing with the numerical results of the tail, in the Figure 5.48 we have the drag coefficient distribution results over the surface. It can be observed that the distributions of both the case with disks and the case with disks and ducts presents a lot of irregularities. These are attributed to the turbulence generated by the disks and ducts. In contrast, in the case of the wing without disks or ducts, these irregularities in the results are not absent as we still have a flow changing the conditions of the tail, but they are considerably lower. The configuration that produces more drag is the one with the ducts since, if the punctual peaks are disregarded, it's the distribution that has the highest values along the tail span due to the high influence of the wakes generated by the ducts. However, it's necessary to emphasize that the distribution that appears to offer the least drag is the one with just the disks, especially at the tail tip. This might be due to the flow interacting with the wingtip vortices of the tail.

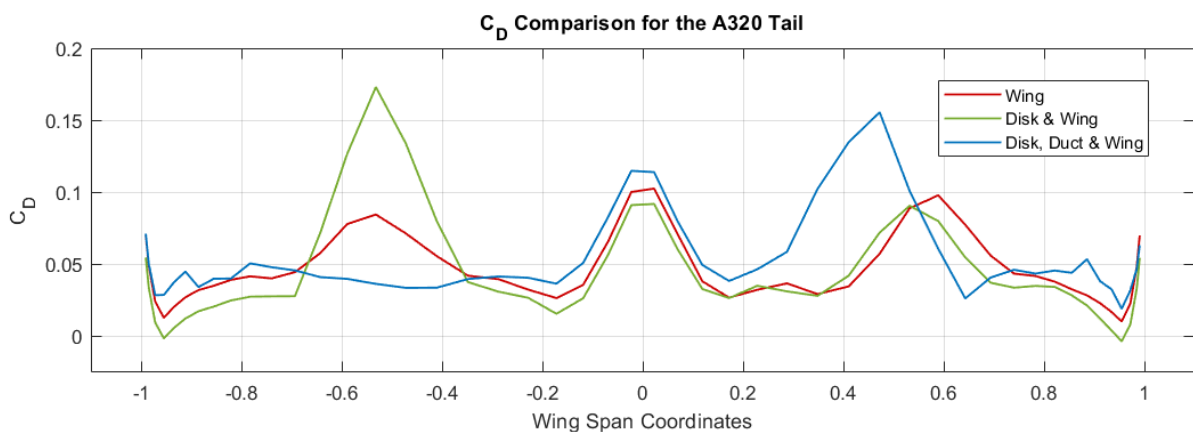


Figure 5.48 Graphical representation of the drag coefficient results of the tail.

The lift coefficient distribution also presents some irregularities but not as heavy as the ones resulted from the drag coefficient distribution as we can see in the Figure 5.49. The distribution that provides the best results is the one with both disks and ducts, followed by the case with only disks. This is likely due to the increased pressures caused by the turbulence generated by the disks and ducts on the underside of the tail leading into an increase of the lift.

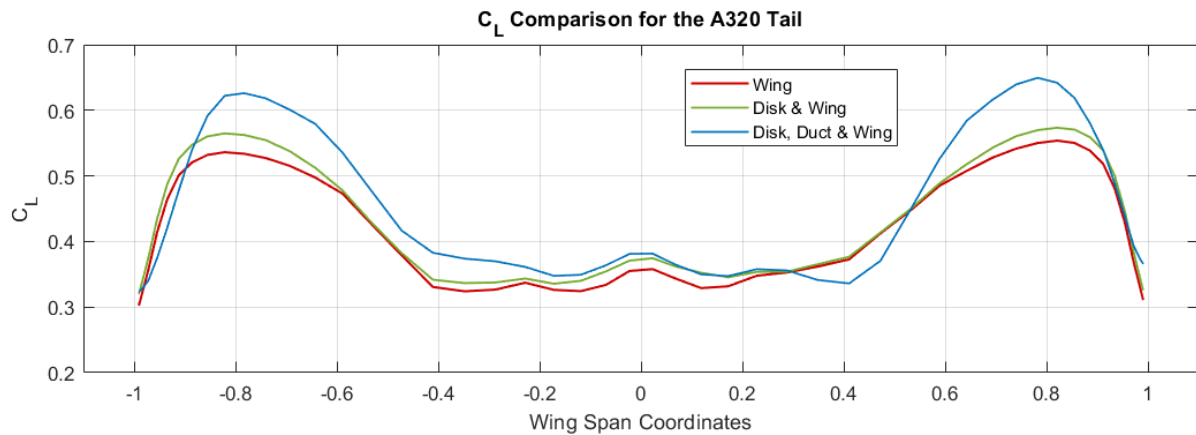


Figure 5.49 Graphical representation of the lift coefficient results of the tail.

Finally, in the Figure 5.50 we have the pressure coefficient distribution. It can be observed that in the case of the configuration with both disks and ducts, the pressures are higher, both on the upper and lower surfaces, followed by the case with only disks. These results align with the previously mentioned outcomes for lift and drag.

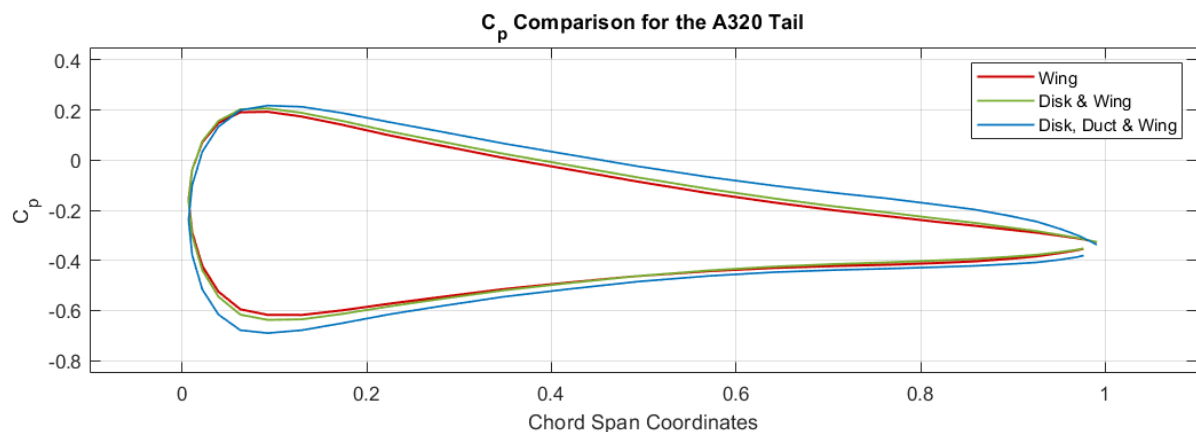


Figure 5.50 Graphical representation of the pressure coefficient results of the tail.

Aerodynamic Results

In the Figure 5.51 we have the aerodynamic results of the wing without any disks or ducts. In the image of the right we can observe better how the main wing affects the horizontal tail, generating small turbulences on it.

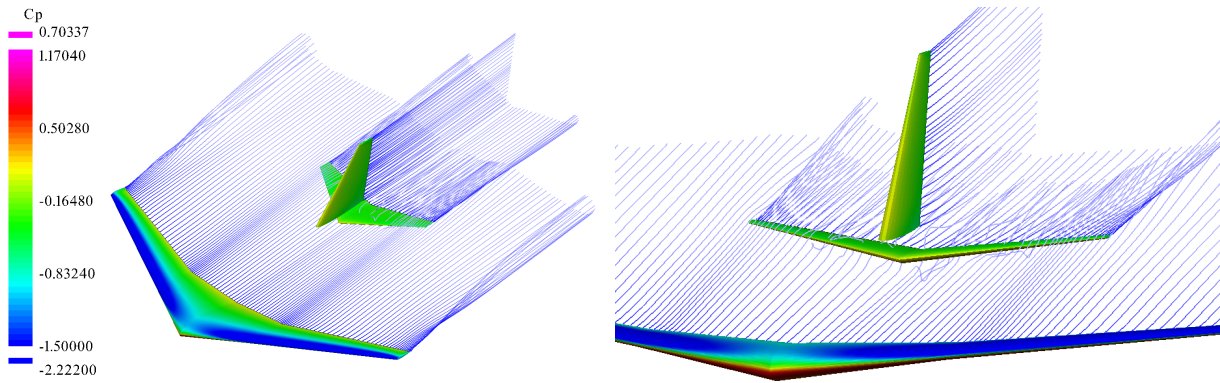


Figure 5.51 Wing and tail aerodynamic results.

Continuing with the case with only disks, in the Figure 5.52 we can observe very similar results to the previous case, with slightly higher visible perturbations of the flow, specially on the lower part of the tail, caused by the main wing.

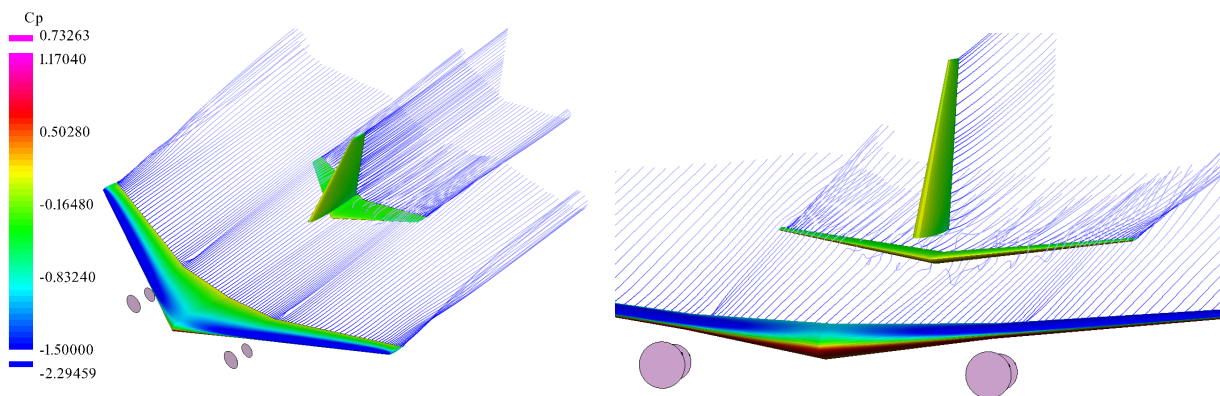


Figure 5.52 Wing and tail aerodynamic results for the disks, ducts & wing case.

Lastly, in Figure 5.53, we have the results for the case with ducts. Here, the flow's influence on the tail is considerably greater, especially at the tail tips, as it's the area where the wakes generated by the engines impact most directly.

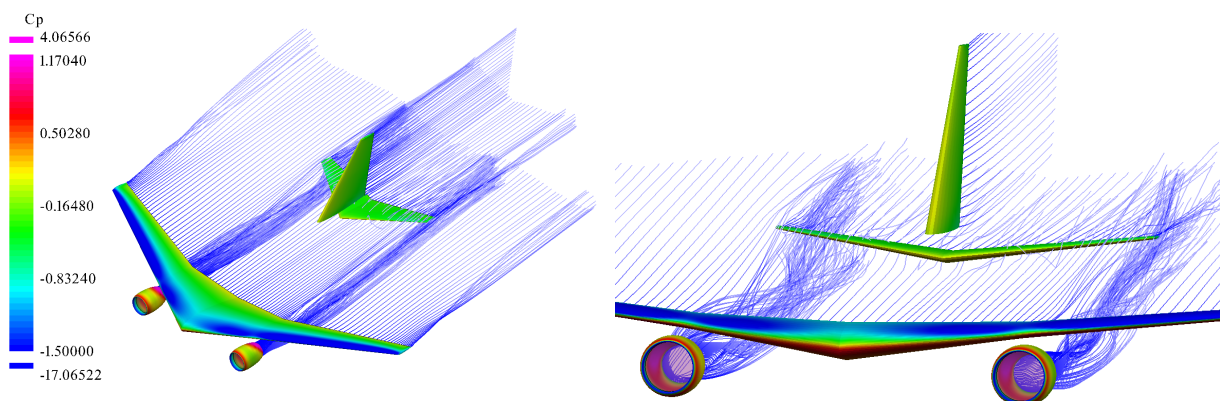


Figure 5.53 Wing and tail aerodynamic results for the disks, ducts & wing case.

5.6 Best Distribution

In this chapter we are going to compare the two distributions that gave the best results in order to analyze if there's a possible better distribution for the Airbus A320. The two configurations chosen are the one with the engines above the wing and the one with the engines situated above the tips of the wing. These two configurations have been chosen primarily based on the numerical results obtained in each chapter.

Starting with the case of engines above the wing of the Chapter 5.2, for the scenarios with only disks and with disks and ducts, the drag gives better results, exhibiting lower values than the base case with engines below. Furthermore, regarding the lift coefficient distribution, for the case with only disks, the resulting lift is higher across the entire wing than in the scenario with engines beneath, and in the case of disks and ducts, the lift in the inner wing area is considerably higher. Lastly, concerning the pressure coefficients, the results are slightly less favorable, especially for the case with ducts, particularly on the upper surface. Nevertheless, these differences are not excessive or problematic, as they still outperform the wing's performance without engines so that's the reason this was one of the configurations chosen.

Moving to the configurations with engines at the wingtips of the Chapter 5.4 and starting with the analysis of the drag coefficient, the case that provides the lowest drag and therefore, better results, is the one with engines below the wingtips, and the one that provides the most is the case with engines in front of them. But the opposite effect happens with the lift distribution, where the configuration with the engines below provides very low values of lift on the wingtips and the configuration with the engines in the front gives very high values. It might be that the case with engines above the tips doesn't offer the best results in terms of drag and lift when analyzed separately. However, it is the configuration that yields more reliable and consistent outcomes, being these very similar to the ones offered by the wing without any engine.

Finally, none of the distributions involving more engines were selected for the best distribution analysis. In Chapter 5.3, the results of this analysis demonstrated that, in all cases, the drag and lift distributions didn't provide better outcomes compared to the base case, with higher drag values and lower lift values along the entire wingspan.

Geometries

In Figures 5.54 and 5.55, we can observe the before mentioned configurations with the tails. By examining their positions relative to the engines and before delving into the numerical results, it can be hypothesized that the engines on the tail might likely have the least impact on the tail's aerodynamics. However, it will only be after analyzing all the results that a determination can be made regarding the most optimal configuration.

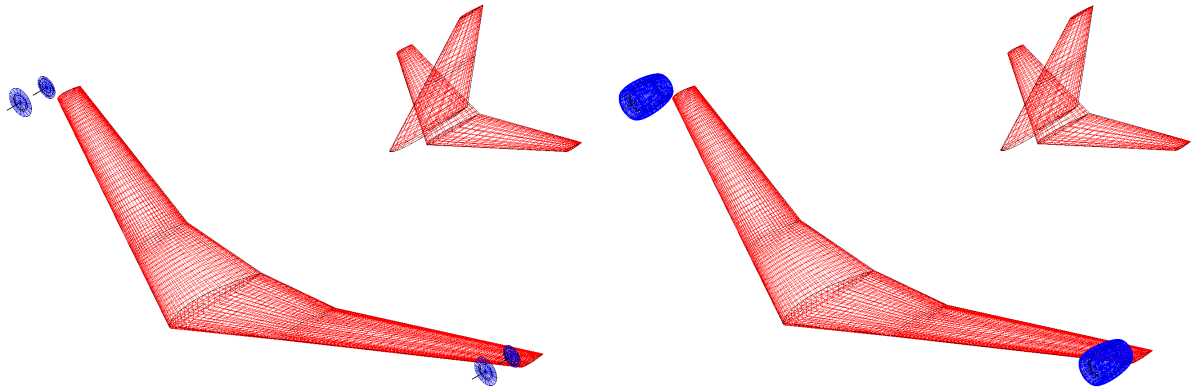


Figure 5.54 Engines above the tips and tail geometries. From left to right: wing & disks case and wing, disks & ducts case.

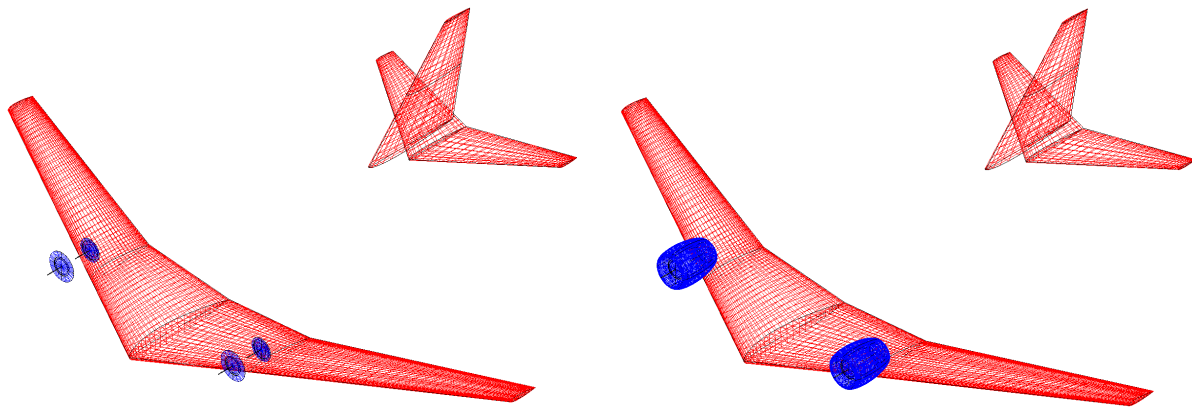


Figure 5.55 Engines above and tail geometries. From left to right: wing & disks case and wing, disks & ducts case.

Best Numerical Results of the Wing

In this chapter, the same as the section where we analyzed the results of the tip engines (see Chapter 5.4), the pressure coefficient is not going to be analyzed. The reason behind this is that, just as in the wingtip analysis, the sections where the engines influence the wing when they are located in this area are not possible to analyze correctly and also, if it was possible, it wouldn't make any sense as the sections would be completely different.

Starting with the results for the drag coefficient for the disk & wing case of the Figure 5.56 we have that the distribution that produces more drag is the base case with the engines below the wing. Moreover, in the other two cases, the results are better than in the base case, but in different areas. Depending on where the engines are positioned, whether at the wingtips or above the wing, the drag generated for the analyzed angle of attack is significantly reduced in that respective areas.

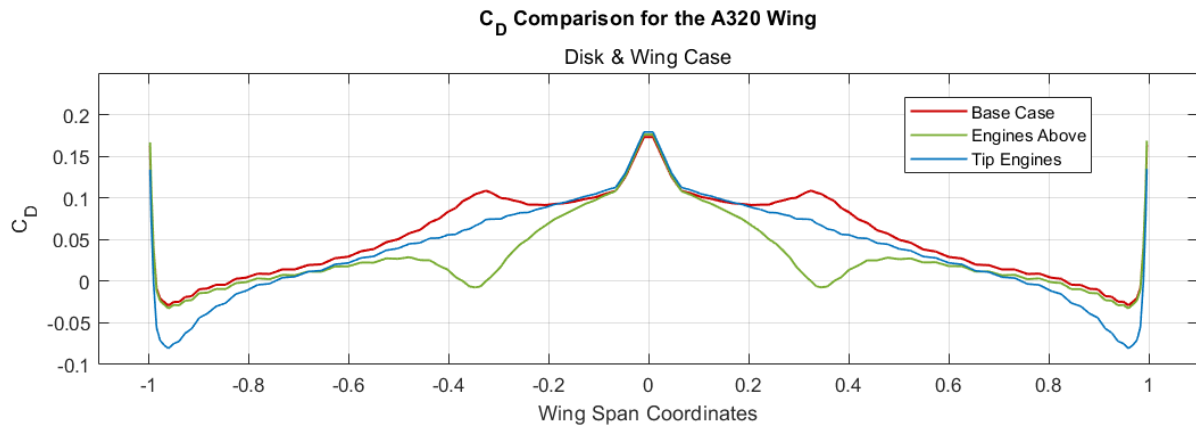


Figure 5.56 Graphical representation of the drag coefficient wing results of the Best Results for the disks & wing case.

Continuing with the case of disks and ducts, as we can see in the Figure 5.57 the results are quite similar. The base case still yields the highest drag values. In the scenario of engines above the wing, the generated drag is also higher than in the case with only disks, whereas in the case with added ducts, this value decreases.

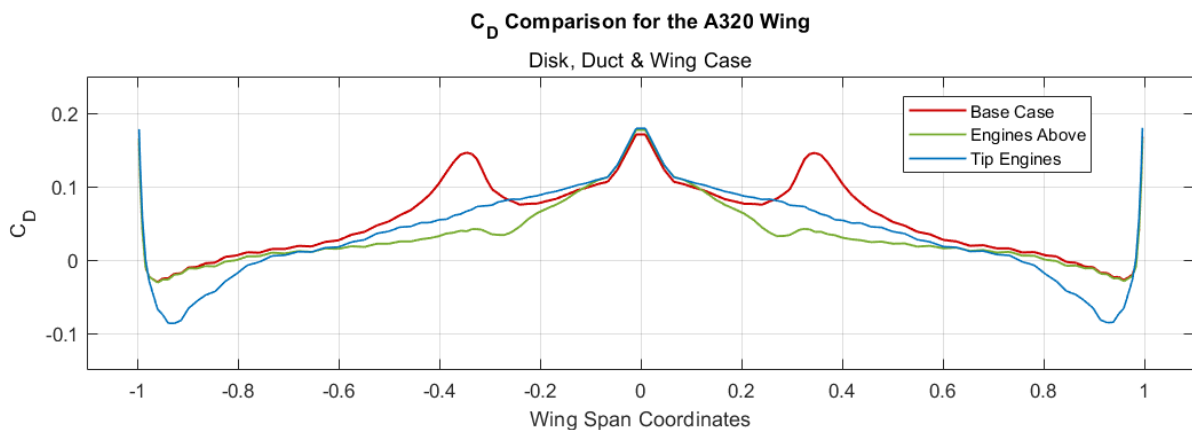


Figure 5.57 Graphical representation of the drag coefficient wing results of the Best Results for the disks, ducts & wing case.

Next, in Figure 5.58, we can observe the lift distribution results for the case with only disks. Similar to the drag distribution, the base case gives the lowest and consequently, the poorest lift results. The configuration that provides the highest lift is the one with engines at the wingtips.

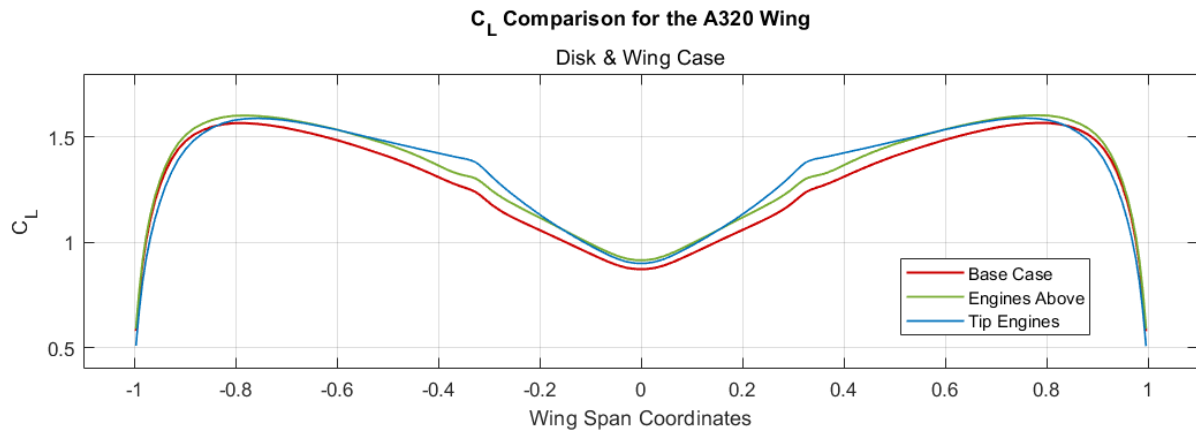


Figure 5.58 Graphical representation of the lift coefficient wing results of the Best Results for the disks & wing case.

Lastly, within the wing analysis, Figure 5.59 shows the results when the ducts are considered. The configuration that stands out the most is the one with the engines above the wing, which exhibits the highest lift in the wing region between the engines but yields the least favorable outcomes in the outer region. Considering the overall wing performance, the distribution that generates the most lift is the one with engines at the wingtips, as the distribution is higher, more uniform, and doesn't exhibit drastic variations.

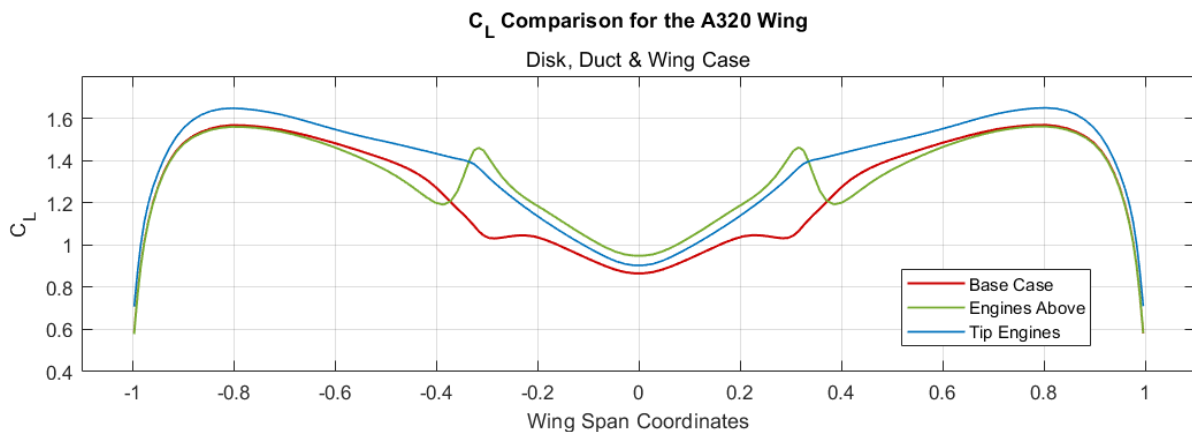


Figure 5.59 Graphical representation of the lift coefficient wing results of the Best Results for the disks, ducts & wing case.

Best Numerical Results of the Tail

In the case of the tail study, the pressure coefficient distribution will be analyzed. This analysis will be conducted for all cases in the same section, aiming to observe how the combination of the different configurations of the wing with the engines impacts its aerodynamics. This section will be positioned at 5.000 meters from the center of the tail, equivalent to the position ± 0.8 in dimensionless coordinates.

Starting with the case of drag coefficient distribution over the tail when only the disks are used (see Figure 5.60), it can be observed that, excluding the peaks, the base case on average generates the least drag, although the difference with the other two configurations is minimal. All of the three distributions have a higher drag both in the tips and near the section ± 0.5 of the horizontal wing.

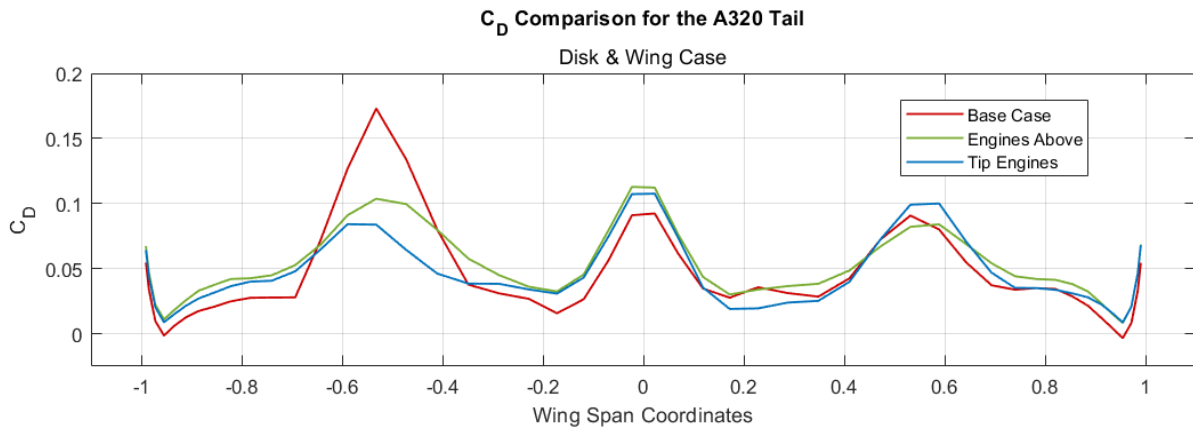


Figure 5.60 Graphical representation of the drag coefficient tail results of the Best Results for the disks & wing case.

When analyzing the case with ducts, the results vary considerably, as shown in Figure 5.61. The drag distributions for the base case and the engines at the wingtips become more linear, with fewer peaks. In contrast, in the case of engines above the wing, irregularities form at the tail tips appear due to the influence of wakes generated by the ducts.

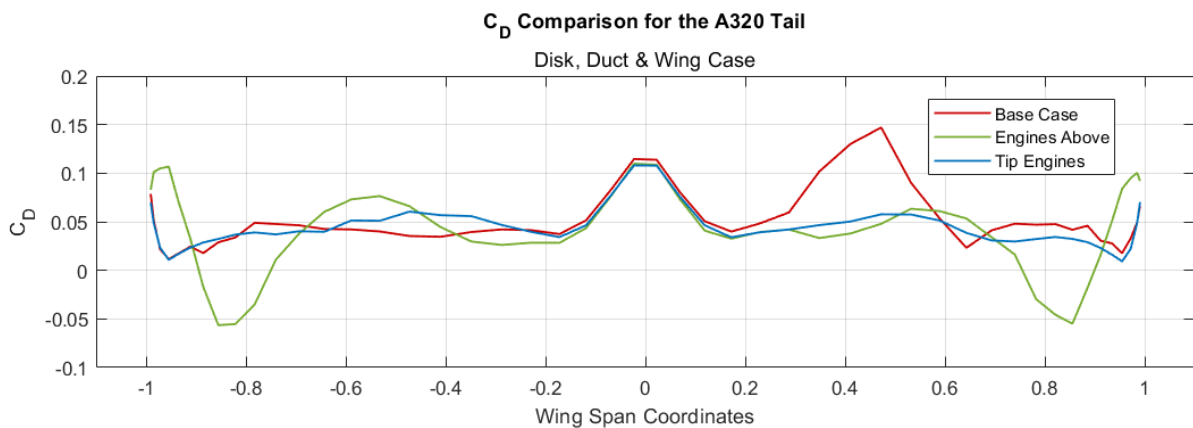


Figure 5.61 Graphical representation of the drag coefficient tail results of the Best Results for the disks, ducts & wing case.

Regarding the lift coefficient distribution for the disks in Figure 5.62, it's shown that the base case generates the most lift in the tail, while the distributions of the other two cases are quite similar. This is likely due to increased pressure generated on the lower surface and a decrease in pressure on the upper surface caused by the flow deflection resulting from the engines positioned under the wing.

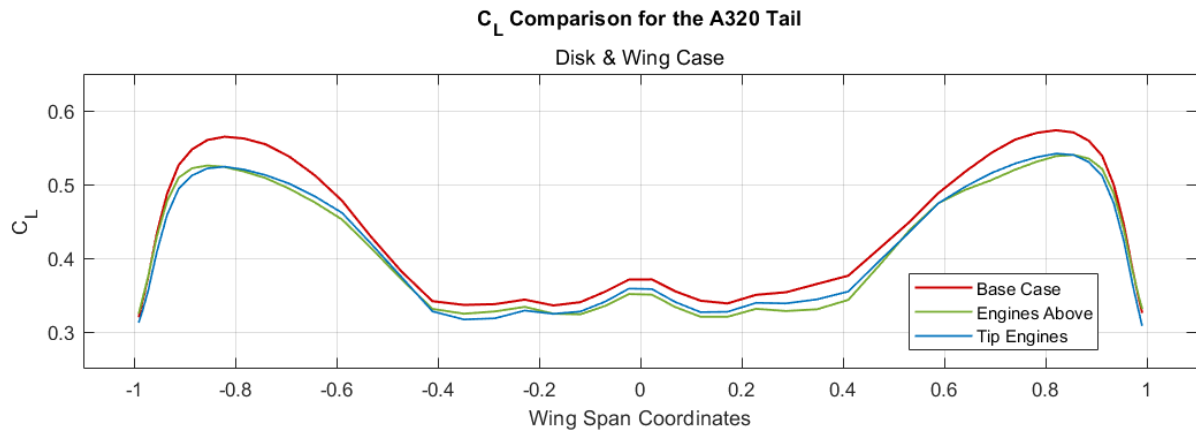


Figure 5.62 Graphical representation of the lift coefficient tail results of the Best Results for the disks & wing case.

For the case when the ducts are added shown in Figure 5.63, the base case continues to give the best results, but differences are noticeable between the cases with the engines above and the engines at the wingtips. In the last one, the generated lift is higher because the wakes generated by the engines barely affect the tail, unlike the case with engines above, where the wakes directly impact the tail, causing turbulence and reducing lift.

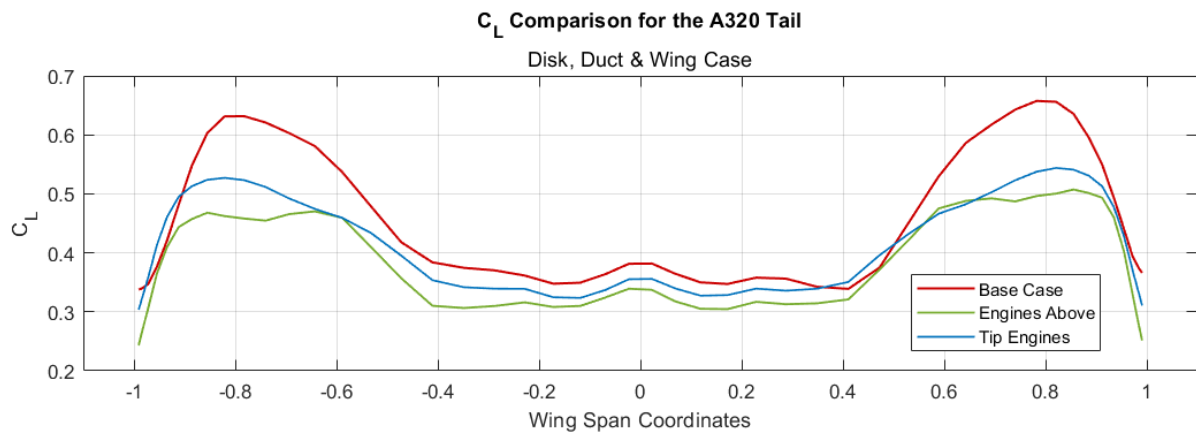


Figure 5.63 Graphical representation of the lift coefficient tail results of the Best Results for the disks, ducts & wing case.

For the pressure distribution when using disks (see Figure 5.64) the results are quite similar in the lower surface but we can see that the upper surface pressure of the base case is lower than the other two cases. This is mainly translated in a higher lift result, just as the results shown in the Figure 5.62.

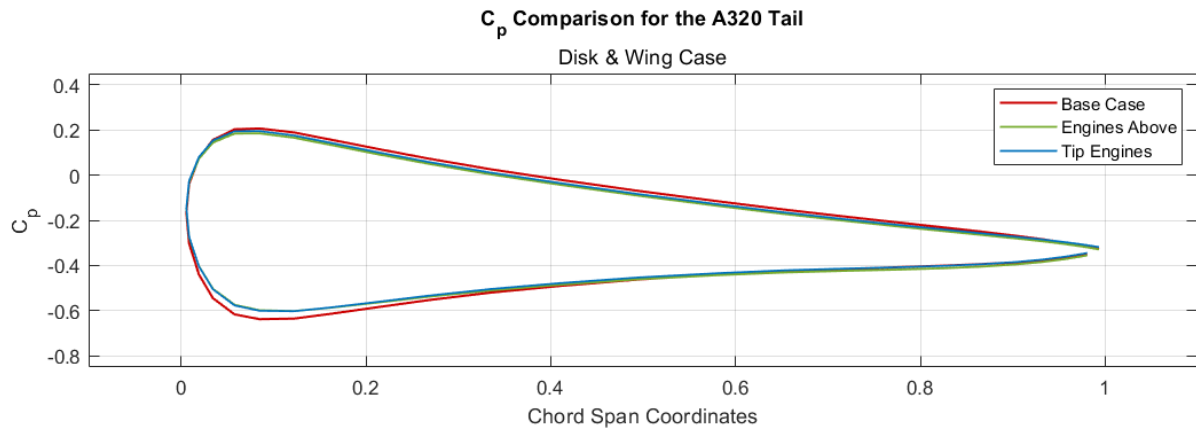


Figure 5.64 Graphical representation of the pressure coefficient tail results of the Best Results for the disks & wing case.

In the Figure 5.65 we can see the influence of the pressure change caused by the ducts on the different surfaces on the lift coefficient distribution. The engines above configuration shows a higher pressure on the upper surface of the tail, leading to a reduction in lift. In the case for the tip engines the pressure on the lower surface is slightly smaller than the one with the engines above. However, when we move to the lower surface of the tail, we observe that the pressures are considerably lower in comparison, resulting in an increased lift as demonstrated in Figure 5.63.

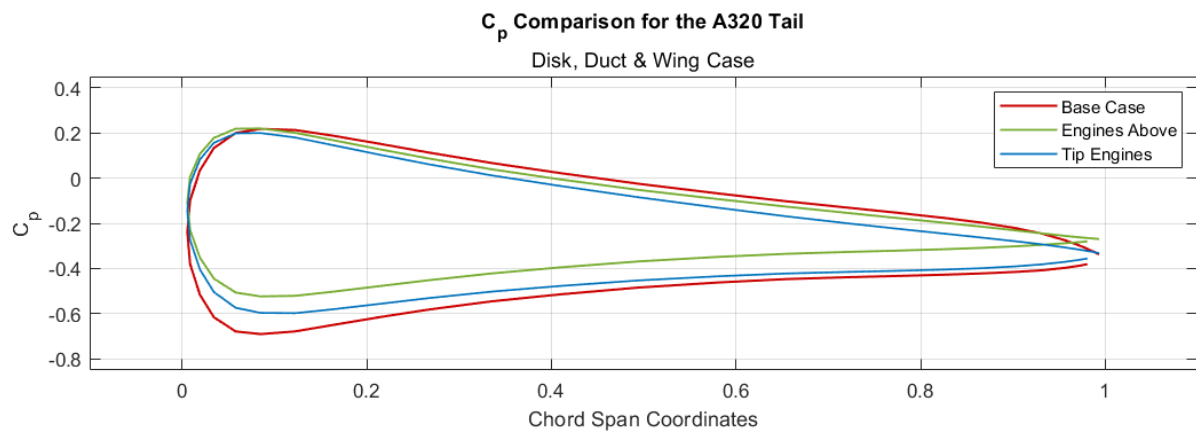


Figure 5.65 Graphical representation of the pressure coefficient tail results of the Best Results for the disks, ducts & wing case.

Aerodynamic Results

In Figures 5.66 and 5.67, it can be observed how having the engines at the wingtips affects the tail. It's noticeable that the interaction between both is minimal since they are significantly separated, resulting in the distortion of the wing's wakes generated by the disks and ducts barely affecting the tail area in both cases.

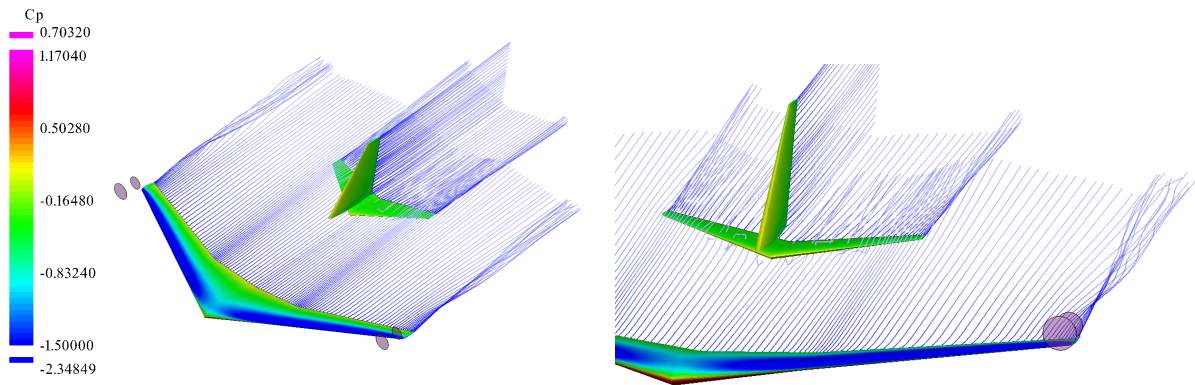


Figure 5.66 Engines above the tips and tail aerodynamic results for the disks & wing case.

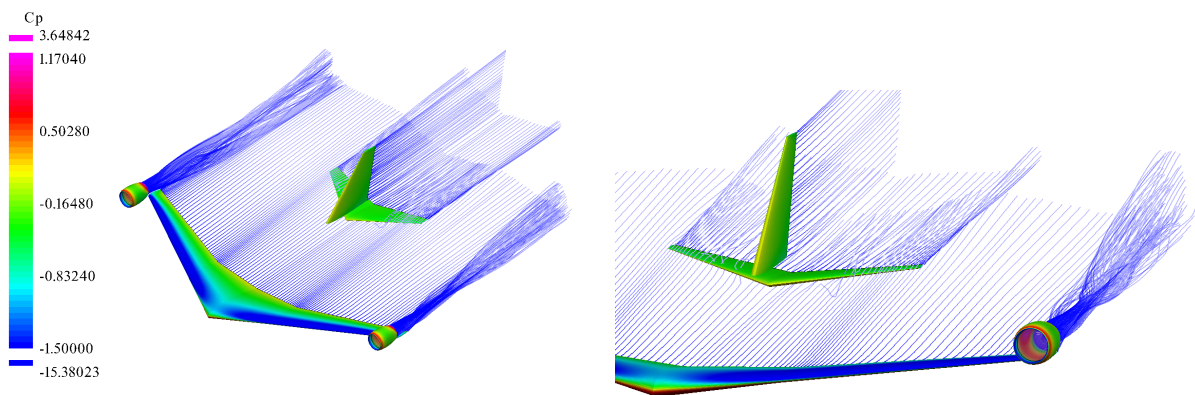


Figure 5.67 Engines above the tips and tail aerodynamic results for the disks, ducts & wing case.

However, when analyzing the results for the case with engines above the wing in Figures 5.68 and 5.69, a clear influence on the tail can be observed, especially in the case where the ducts are considered. Here, the previous results of the pressure changes can be clearly observed.

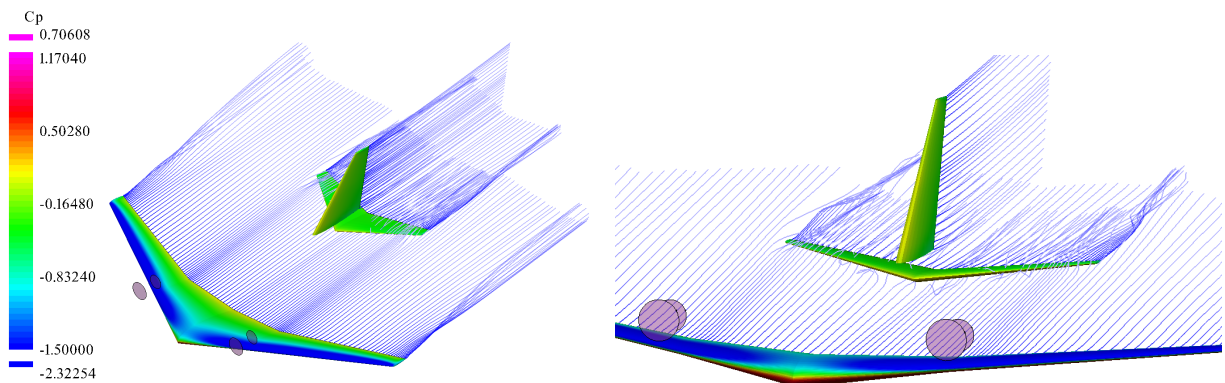


Figure 5.68 Engines above and tail aerodynamic results for the disks & wing case.

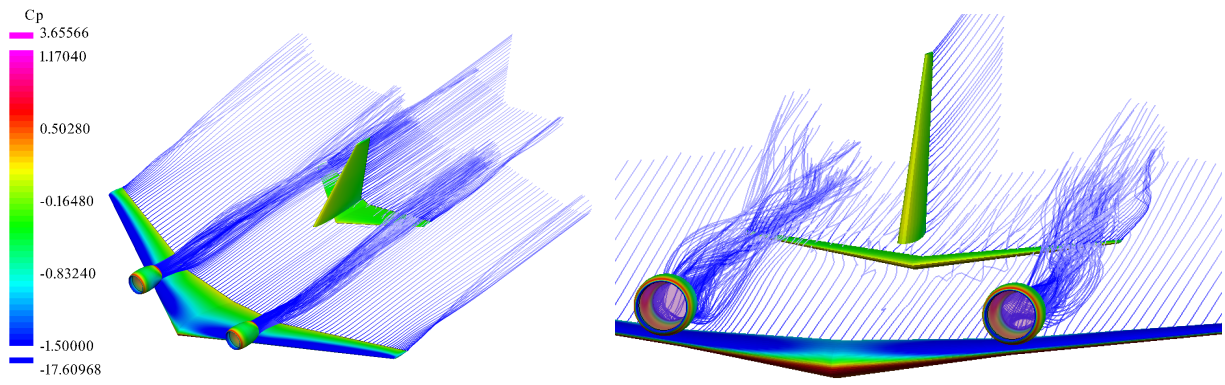


Figure 5.69 Engines above and tail aerodynamic results for the disks, ducts & wing case.

6 Discussion

Following the analysis of the results obtained in the simulations of Chapter 5, we will proceed to conduct an evaluation in order to determine the most viable option among the chosen distributions in terms of aerodynamic performance.

Starting with the wing's performance, which will be considered the most relevant as it is responsible for generating the majority of the aircraft's lift, it's observed that in the results of the drag coefficient distribution the base case yields the poorest results. On the other hand, both placing the engines at the wingtips and above offer different advantages, whether we use only disks or disks and ducts. However, when analyzing the lift coefficient distribution, it becomes evident that the wing configuration with engines at the wingtips offers the best results. This not only translates to higher lift but also more consistent values across the span of the wing.

Moving on to the tail's performance, unlike the wing performance, the base case generally yields the best results. However, since the results for wing performance are considerably worse, it will be definitively excluded from this analysis. With this in mind, among the remaining two configurations, when considering the drag coefficient, the distribution with engines above offers the minimum drag values, but it also presents the least uniform results. This is considered a problem since the primary function of an aircraft's tail is to stabilize, and a less uniform drag distribution can make its performance harder to control. Regarding the lift coefficient distribution, when only disks are used, the results are quite similar. However, when ducts are added, the performance of the tip engines is considerably better across the entire span of the wing. A similar phenomenon occurs with the pressure coefficient distribution over the tail.

Finally, when we observe the aerodynamic results, it's clear that the engines on the wingtips have significantly less influence on the tail aerodynamics compared to the engines above. It's for this reason, along with the points mentioned earlier, that the configuration with engines on the wingtips has been chosen as the best option for the Airbus A320 model.

7 Summary and Conclusions

7.1 Summary

In the initial chapters, the motivations and objectives that were intended to be covered in this thesis have been discussed. Furthermore, an introduction to the VSPAero software was provided, explaining its history, applications, features, and tools.

Following this, we have deepened into the theory upon which the program is based for conducting calculations, with a primary focus on the concepts related to actuator disks and the panel method.

After that, the explanation and process of the preliminary steps have been explained. We discussed the geometries used, their characteristics, and provided a detailed explanation of creating ducts using the software. Furthermore, a refinement analysis was performed on these geometries to find the optimal point where a balance between result quality and simulation time was obtained.

Another analysis conducted is the one relative to the actuator disks. We examined their operation, characteristics, and how they are defined in the program. Additionally, a study was made on their performance when used with the ducts to determine which scenario was the closest to a real engine. The most realistic and favorable case was selected.

All the before mentioned steps have been carried out to conduct simulations of various engine placement configurations on the wing of the Airbus A320. This includes an analysis of the original Airbus A320 configuration, one with engines above the wings, two cases with additional engines, and three more cases with engines positioned at different heights on the wingtips. In these simulations, the results of the C_L , C_D and C_p distributions and its aerodynamics have been analyzed.

Finally, the two best results have been compared to the A320's original configuration, taking into account the effects on the tail. This comparison has led to the identification of an engine configuration that apparently gives better results compared to the original one, particularly at high angles of attack.

7.2 Conclusions

After analyzing the performance of the actuator disks, it can be concluded that when they are used to create only the jump conditions of the fluid, it's challenging to assess the accuracy of their results when compared to a real case because they do not consider the influence of the actual engine geometry. When ducts are added, a behavior closer to reality can be observed since the influence of the engine geometry becomes apparent. However, other characteristics related to engine performance, such as noise, efficiency, weight, fuel consumption, etc. cannot be analyzed using VSPAero.

This is one of the primary reasons why this software is primarily employed for preliminary studies and not for more detailed analyses. Nonetheless, it has been concluded that VSPAero is a very useful and powerful tool for preliminary analysis because it provides results that are realistic enough for initial assessments.

It has also been concluded, after evaluating the preliminary analysis of different engine placements on the overall wing and tail of the Airbus A320, that a new design of the A320 with better aerodynamic characteristics than the original could potentially be implemented, at least when high angles of attack are studied.

8 Recommendations

To expand the information in this work, a wide range of activities can be done. For example, analyzing whether using wingtips on the wing, as in the real case of the Airbus A320, would still make the chosen configuration the most optimal in terms of aerodynamics or not.

Another option would be to conduct the same analysis but modifying the geometry of the engines, or in other words, the disks and ducts, so that the final result is closer to that of the IAE V2500 engine used in the Airbus A320.

List of References

- AIRBUS, 2005. *A320. Aircraft Characteristics - Airport and Maintenance Planning*.
 Open Access at: <http://bit.ly/48oeLUE>
 Archived at: <https://perma.cc/N7JS-2A4U>
- ANDERSON, John D., 1984. *Fundamentals of aerodynamics*. Second Edition. University of Maryland, Maryland, USA: McGraw-Hill.
 Open Access at: <https://bit.ly/3EIIfin>
 Archived at: <https://perma.cc/2KBQ-9E4F>
- BOLSUNOVSKI, A. L., BRAGIN, N. N., BUZOVERYA, N. P., PERCHENKOV, E. S., CHERNYSHEV, I. L., SKOMOROKHOV, S. I., 2023. *Computational and Experimental Studies of a Low-Noise Aircraft with a Laminar Wing and Engines above the Trailing Edge of the Wing*. In: *Mathematical Models and Computer Simulations*, vol. 15, no. 1., pp. 79-91. Pleiades Publishing Ltd.
 Available from: <https://doi.org/10.1134/s2070048223010039>
 Open Access at: <https://bit.ly/46ksb2n>
 Archived at: <https://perma.cc/DVU3-EWUM>
- BOLSUNOVSKI, A. L., BUZOVERYA, N. P., CHERNYSHEV, I. L., CHERNY, K. I., PUSHCHIN, N. A., 2019. *The numerical and experimental studies on the over-wing-engine configurations aerodynamics*. Madrid, Spain: Proceedings of the 8th European Conference for Aeronautics and Space Sciences. Pleiades Publishing Ltd.
 Open Access at: <https://www.eucass.eu/doi/EUCASS2019-0329.pdf>
 Archived at: <https://perma.cc/5KGX-V7FR>
- CHATTOT, Jean-Jacques, 2014. *Actuator Disk Theory - Steady and Unsteady Models*. In: *Journal of Solar Energy Engineering*, vol. 136, no. 3. ASME International.
 Available from: <https://doi.org/10.1115/1.4026947>
 Open Access at: <https://bit.ly/48jxH79>
 Archived at: <https://perma.cc/PE58-737W>
- CUPA, 2023a. *Flow*. Cambridge University Press & Assessment.
 Available from: <https://dictionary.cambridge.org/dictionary/english/flow>
 Archived at: <https://perma.cc/77MR-A7GP>
- CUPA, 2023b. *Tool*. Cambridge University Press & Assessment.
 Available from: <https://dictionary.cambridge.org/dictionary/english/tool>
 Archived at: <https://perma.cc/ES9L-5ZU6>
- CUPA, 2023c. *Visualization*. Cambridge University Press & Assessment.
 Available from: <https://dictionary.cambridge.org/dictionary/english/visualization>
 Archived at: <https://perma.cc/ZE4G-FH98>

- ERICKSON, Larry L., 1990. *Panel Methods: An introduction*. Technical Publication. National Aeronautics and Space Administration.
Available from: <https://ntrs.nasa.gov/citations/19910009745>
Open Access at: <https://go.nasa.gov/3rkxiAE>
- GLOUDEMANS, James, DAVIS, Paul, GELHAUSEN, Paul, 1996. *A rapid geometry modeler for conceptual aircraft*. 34th Aerospace Sciences Meeting and Exhibit. American Institute of Aeronautics and Astronautics.
Available from: <https://doi.org/10.2514/6.1996-52> (Closed Access)
- HAHN, Andrew S., 2010. *Vehicle Sketch Pad: A Parametric Geometry Modeler for Conceptual Aircraft Design*. 48th AIAA Aerospace Sciences Meeting Including the New Horizons Forum and Aerospace Exposition. Aerospace Research Central.
Available from: <https://doi.org/10.2514/6.2010-657> (Closed Access)
- JONNISON, Alexander, 2000. *Muk Air VFW-614*.
Available from: <https://bit.ly/469OJTk>
Archived at: <https://perma.cc/Y9WL-RDWV>
- LITHERLAND, Brandon, 2023. *OpenVSP Google Group*.
Available from: <https://bit.ly/451PjBo>
Archived at: <https://perma.cc/PN43-FFJV>
- LITHERLAND, Brandon, 2021. *Modeling Best-Practices for VSPAERO*. In: OpenVSP Workshop 2021. National Aeronautics and Space Administration.
Available from: <https://openvsp.org/wiki/doku.php?id=workshop2021>
Open Access at: <https://bit.ly/48jsMTJ>
Archived at: <https://perma.cc/6ZWP-HKW3>
- LIU, Chao, 2007. *Wake Vortex Encounter Analysis with Different Wake Vortex Models Using Vortex-Lattice Method*. Master Thesis. Delft, Netherlands: Delft University of Technology.
Available from: <https://bit.ly/450H3BU>
Open Access at: <https://bit.ly/45Z7bOJ>
- MARIËN, Floris, 2021. *Software Testing: VSPAERO*. Master Thesis. Hamburg, Germany: Hamburg University of Applied Sciences.
Available from: <https://bit.ly/3sWd4NX>
Open Access at: <https://www.fzt.haw-hamburg.de/pers/Scholz/arbeiten/TextMarien.pdf>
- MASON, W. H., 1998. Chapter 8: Introduction to Computational Fluid Dynamics. In: *Applied Computational Fluid Dynamics*, vol. 2. Cambridge University Press.
Available from: <https://bit.ly/3LucqxE>
Open Access at: <https://bit.ly/4612Ria>
Archived at: <https://bit.ly/4612Ria>

- MCDONALD, Robert A., GLOUDEMANS, James R., 2021. *Open Vehicle Sketch Pad: An Open Source Parametric Geometry and Analysis Tool for Conceptual Aircraft Design*. AIAA SCITECH 2022 Forum. American Institute of Aeronautics and Astronautics.
Available from: <https://arc.aiaa.org/doi/epdf/10.2514/6.2022-0004> (Closed Access)
- MODLA, Christian, 2023. *A Lufthansa Airbus A380 aircraft approaching Leipzig/Halle Airport*.
Available from: <https://bit.ly/3RtOOwR>
Archived at: <https://perma.cc/LQ2S-HNE8>
- NOSA. *NASA Open Source Agreement*. National Aeronautics and Space Administration.
Available from: <https://openvsp.org/license.shtml>
Archived at: <https://perma.cc/K7BB-5U97>
- OPENVSPa. *OpenVSP Ground School*. National Aeronautics and Space Administration.
Available from: <https://vspu.larc.nasa.gov/>
Archived at: <https://perma.cc/XA84-URFM>
- OPENVSPb. *VSP Google Group*. National Aeronautics and Space Administration.
Available from: <https://groups.google.com/g/openvsp>
Archived at: <https://perma.cc/ZHB3-2R97>
- OPENVSPc. *VSP Hangar*. National Aeronautics and Space Administration.
Available from: <https://hangar.openvsp.org/>
Archived at: <https://perma.cc/BFG2-6H6Q>
- OPENVSP, 2022a. *OpenVSP*. National Aeronautics and Space Administration.
Available from: <https://openvsp.org/wiki/doku.php?id=start>
Archived at: <https://perma.cc/W5SP-UHRU>
- OPENVSP, 2022b. *OpenVSP Representations*. National Aeronautics and Space Administration.
Available from: <https://openvsp.org/wiki/doku.php?id=representations>
Archived at: <https://perma.cc/K4HH-ALBR>
- OPENVSP, 2015. *VSPAero*. National Aeronautics and Space Administration.
Available from: <https://openvsp.org/wiki/doku.php?id=vspaerotutorial>
Archived at: <https://perma.cc/DG6Q-SJFW>
- SCHOLZ, Dieter, 2020. *OpenVSP - Connect Hangar*. Hamburg, Germany: Hamburg University of Applied Sciences.
Available from: <https://www.fzt.haw-hamburg.de/pers/Scholz/OpenVSP/A320.html>
Archived at: <https://perma.cc/W8AE-TSQM>

SINNIGE, Tomas, van ARNHEM, Nando, STOKKERMANS, Tom C. A., EITELBERG, Georg, VELDHUIS, Leo L. M., 2019. *Wingtip-Mounted Propellers: Aerodynamic Analysis of Interaction Effects and Comparison with Conventional Layout*. Delft, Netherlands: Delft University of Technology. Journal Article. Journal of Aircraft, vol. 56, no. 1., pp. 295-312.

Available from: <https://arc.aiaa.org/doi/epdf/10.2514/1.C034978> (Closed Access)

SPALART, Philippe R., 2003. *On the simple actuator disk*. Cambridge University Press. Journal Article. Journal of Fluid Mechanics, vol. 494, pp. 399-405.

Available from: <https://doi.org/10.1017/s0022112003006128> (Closed Access)

STEVEN, Mark, 2012. *Antonov An-225*.

Available from: <https://bit.ly/44Z8NXx>

Archived at: <https://perma.cc/4D9A-QDRG>

TURNER, Roland, 2012. *The first prototype of the SO.9000 Trident I on display in the Musée de l'Air et de l'Espace, Paris*.

Available from: <https://bit.ly/3PIGiJi>

Archived at: <https://perma.cc/Q2HS-BFH7>

VELDHUIS, L. L. M., 2004. *Review of Propeller-Wing Aerodynamic Interference*. Delft, Netherlands: Delft University of Technology.

Open Access at: http://icas.org/ICAS_ARCHIVE/ICAS2004/PAPERS/065.PDF

Archived at: <https://perma.cc/GPS7-DCGC>

de VRIES, Reynard, van ARNHEM, Nando, SINNIGE, Tomas, ROELOF, Vos, VELDHUIS, Leo L. M., 2021. *Aerodynamic interaction between propellers of a distributed-propulsion system in forward flight*. Aerospace Science and Technology. Elsevier (BV).

Available from: <https://doi.org/10.1016/j.ast.2021.107009>

Open Access at: <https://bit.ly/3t3EOR2>

WIKIPEDIA, 2023a. *Airbus A380*.

Available from: https://en.wikipedia.org/wiki/Airbus_A380

Archived at: <https://perma.cc/JV6D-FLCK>

WIKIPEDIA, 2023b. *Antonov An-225 Mriya*.

Available from: https://en.wikipedia.org/wiki/Antonov_An-225_Mriya

Archived at: <https://perma.cc/6YXJ-6XHY>

WIKIPEDIA, 2023c. *Beriev Be-200*.

Available from: https://en.wikipedia.org/wiki/Beriev_Be-200

Archived at: <https://perma.cc/9Z42-AC5F>

WIKIPEDIA, 2023d. *CFD*.

Available from: https://en.wikipedia.org/wiki/Computational_fluid_dynamics

Archived at: <https://perma.cc/PPJ8-SJ5R>

WIKIPEDIA, 2023e. *Drag (physics)*.

Available from: [https://en.wikipedia.org/wiki/Drag_\(physics\)](https://en.wikipedia.org/wiki/Drag_(physics))

Archived at: <https://perma.cc/WJ6J-LG7Q>

WIKIPEDIA, 2023f. *Honda HA-420 HondaJet*.

Available from: https://en.wikipedia.org/wiki/Honda_HA-420_HondaJet

Archived at: <https://perma.cc/SVX2-KGUP>

WIKIPEDIA, 2023g. *IAE V2500*.

Available from: https://en.wikipedia.org/wiki/IAE_V2500

Archived at: <https://perma.cc/9QFP-W357>

WIKIPEDIA, 2023h. *Lift (force)*.

Available from: [https://en.wikipedia.org/wiki/Lift_\(force\)](https://en.wikipedia.org/wiki/Lift_(force))

Archived at: <https://perma.cc/V7CR-6XAX>

WIKIPEDIA, 2023i. *Myasishchev M-50*.

Available from: https://en.wikipedia.org/wiki/Myasishchev_M-50

Archived at: <https://perma.cc/FK3F-WG4Y>

WIKIPEDIA, 2023j. *OpenVSP*.

Available from: <https://en.wikipedia.org/wiki/OpenVSP>

Archived at: <https://perma.cc/GR24-NCSS>

WIKIPEDIA, 2023k. *Reynolds Number*.

Available from: https://en.wikipedia.org/wiki/Reynolds_number

Archived at: <https://perma.cc/45NA-7ZBV>

WIKIPEDIA, 2023l. *SNCASO Trident*.

Available from: https://en.wikipedia.org/wiki/SNCASO_Trident

Archived at: <https://perma.cc/WR9T-HK33>

WIKIPEDIA, 2023m. *VFW-Fokker 614*.

Available from: https://en.wikipedia.org/wiki/VFW-Fokker_614

Archived at: <https://perma.cc/QKX4-VBYZ>

WIKIPEDIA, 2021. *Tsybin RSR*.

Available from: https://en.wikipedia.org/wiki/Tsybin_RSR

Archived at: <https://perma.cc/6W4Q-KQCJ>

WIKIPEDIA, 2009. *Myasishchev M-50 on display at Monino Aviation Museum*.

Available from: <https://bit.ly/3PIbXKK>

Archived at: <https://perma.cc/Z5MT-9UWU>

Appendix A – Graphical representations of the non-interpolated results

Base Case

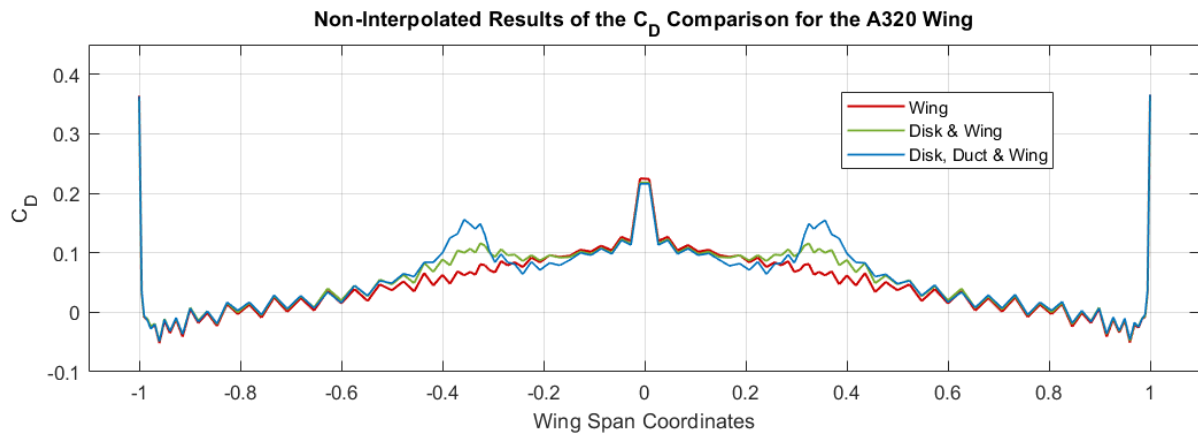


Figure A.1 Graphical representation of the non-interpolated drag coefficient results of the Base Case.

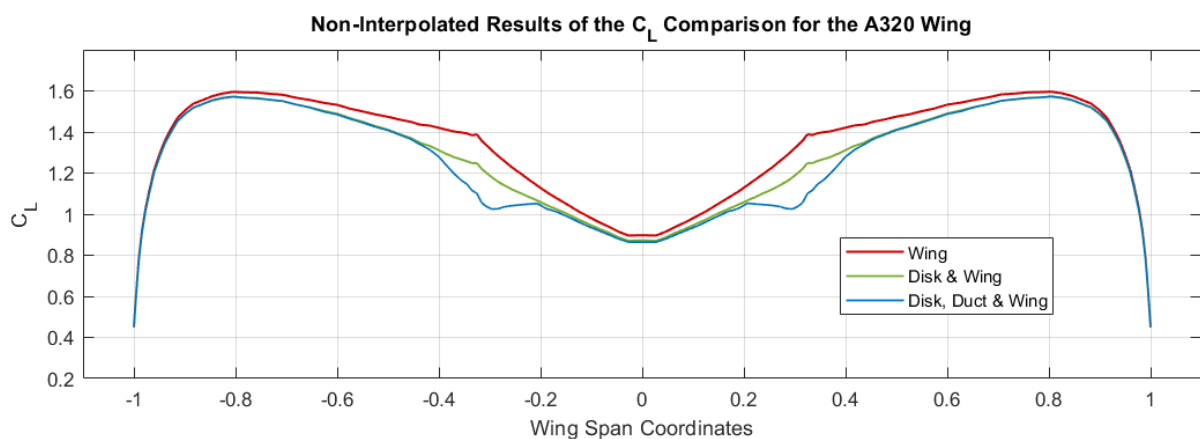


Figure A.2 Graphical representation of the non-interpolated lift coefficient results of the Base Case.

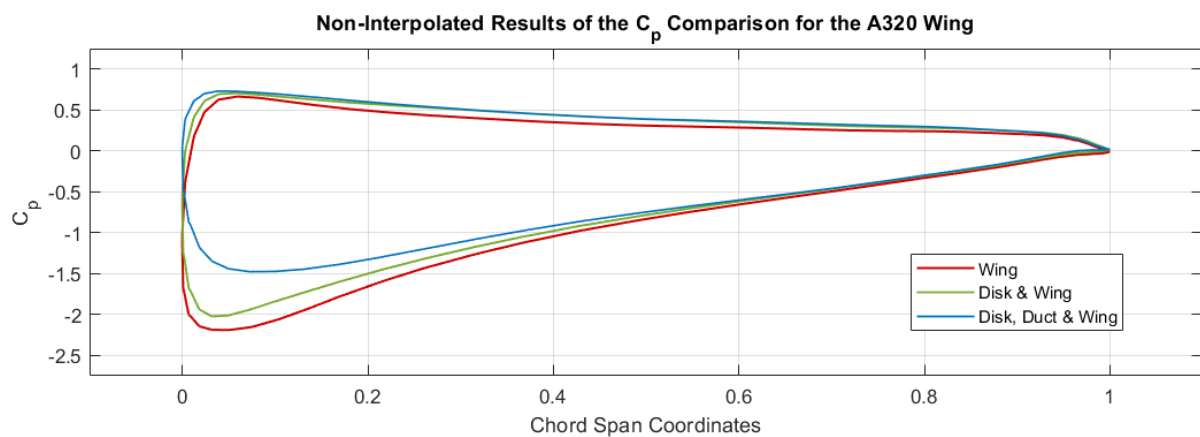


Figure A.3 Graphical representation of the non-interpolated pressure coefficient results of the Base Case.

Engines Above

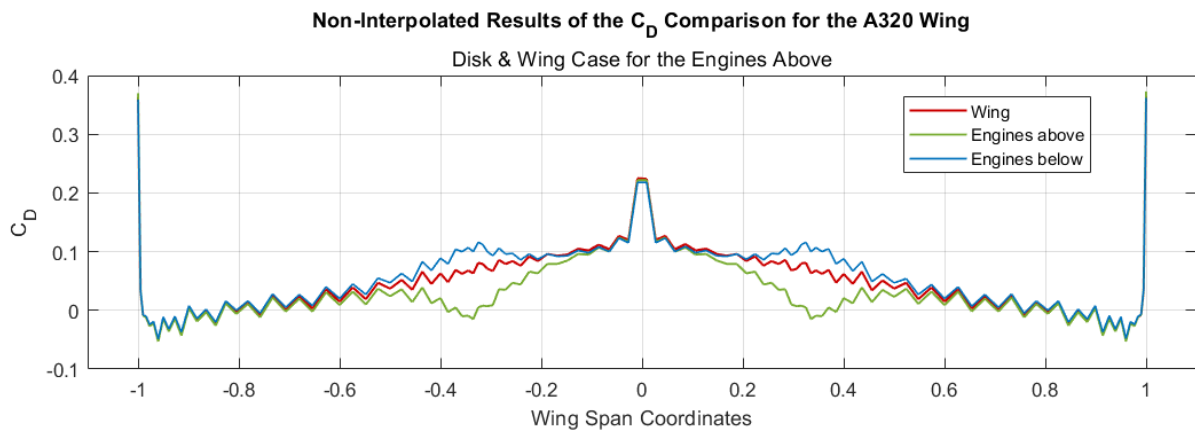


Figure A.4 Graphical representation of the non-interpolated drag coefficient results of the Engines Above for the disks & wing case.

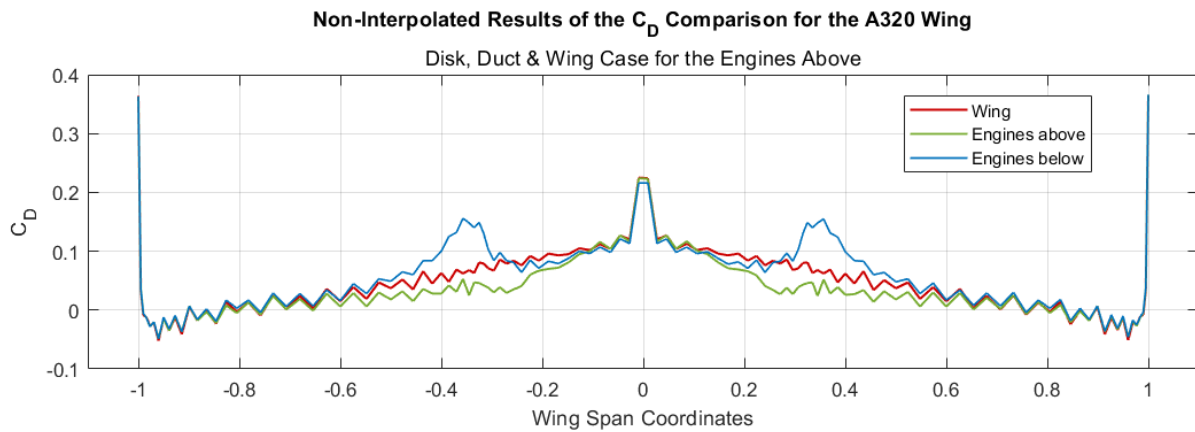


Figure A.5 Graphical representation of the non-interpolated drag coefficient results of the Engines Above for the disks, ducts & wing case.

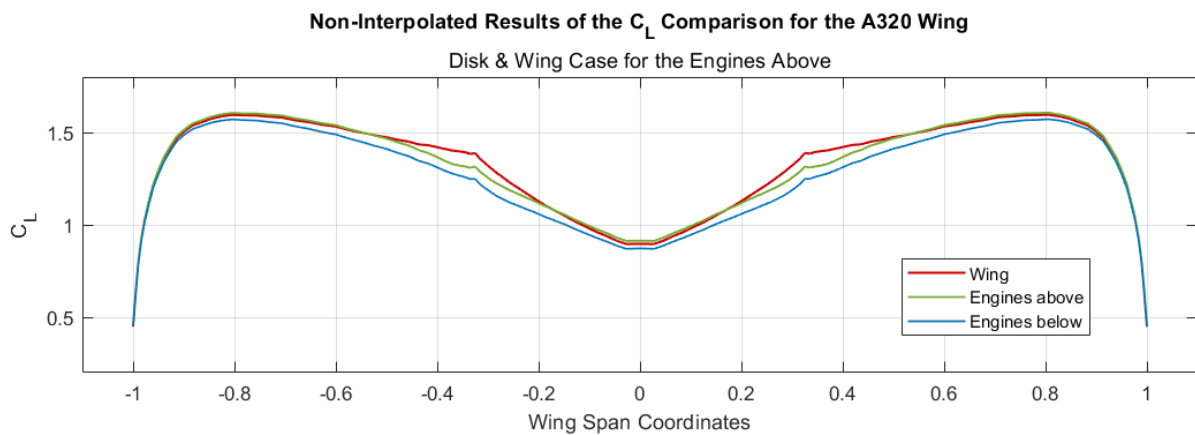


Figure A.6 Graphical representation of the non-interpolated lift coefficient results of the Engines Above for the disks & wing case.

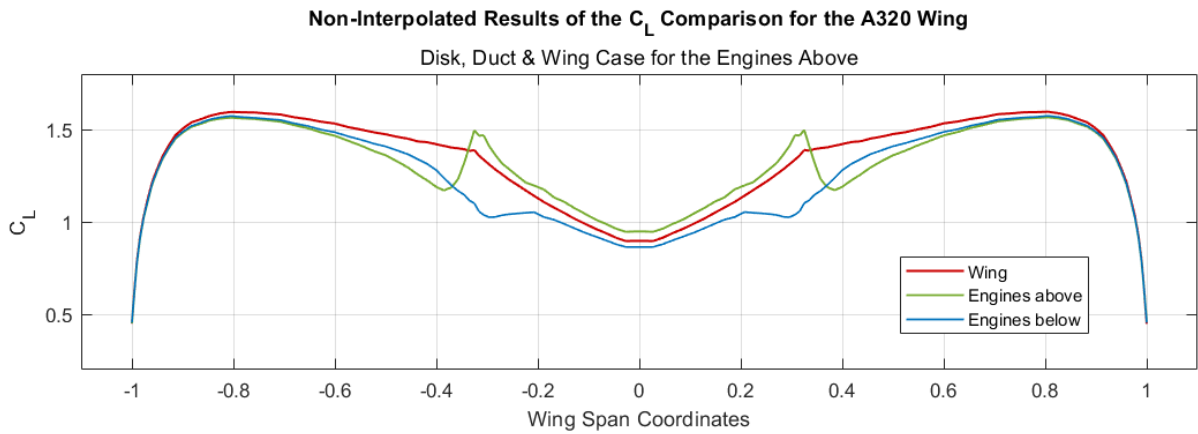


Figure A.7 Graphical representation of the non-interpolated lift coefficient results of the Engines Above for the disks, ducts & wing case.

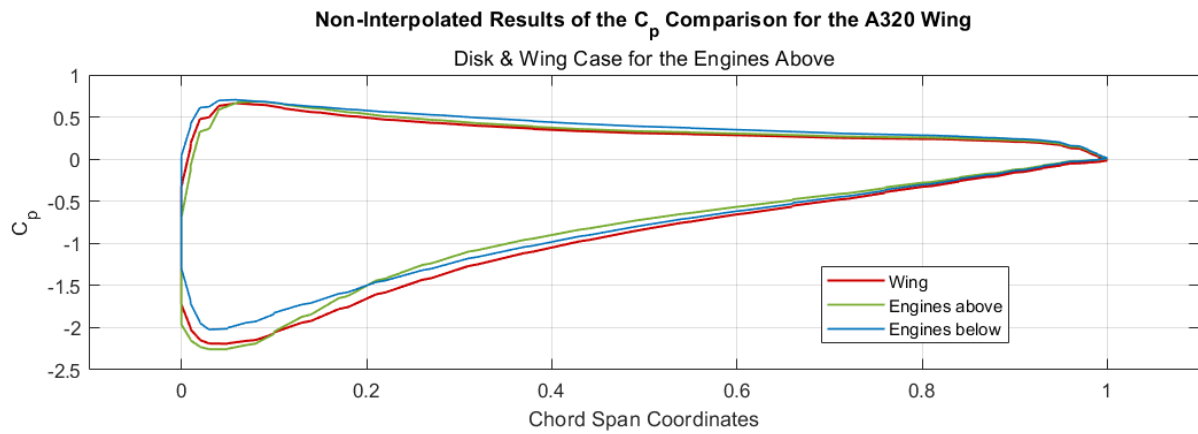


Figure A.8 Graphical representation of the non-interpolated pressure coefficient results of the Engines Above for the disks & wing case.

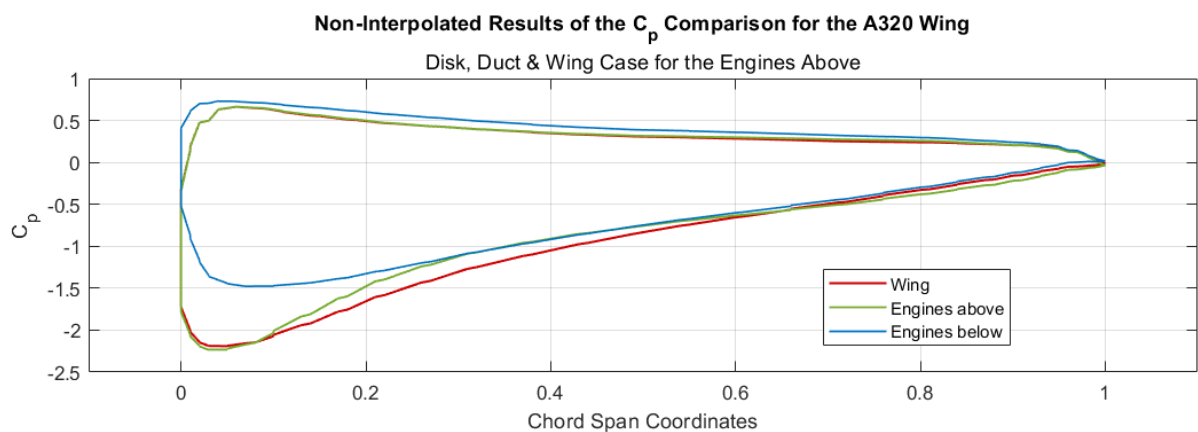


Figure A.9 Graphical representation of the non-interpolated pressure coefficient results of the Engines Above for the disks, ducts & wing case.

More Engines

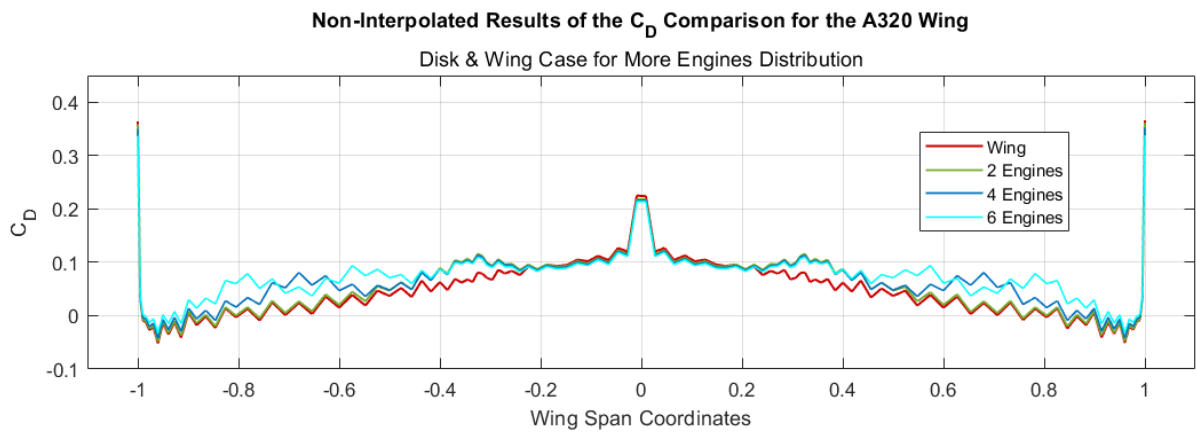


Figure A.10 Graphical representation of the non-interpolated drag coefficient results of the More Engines distributions for the disks & wing case.

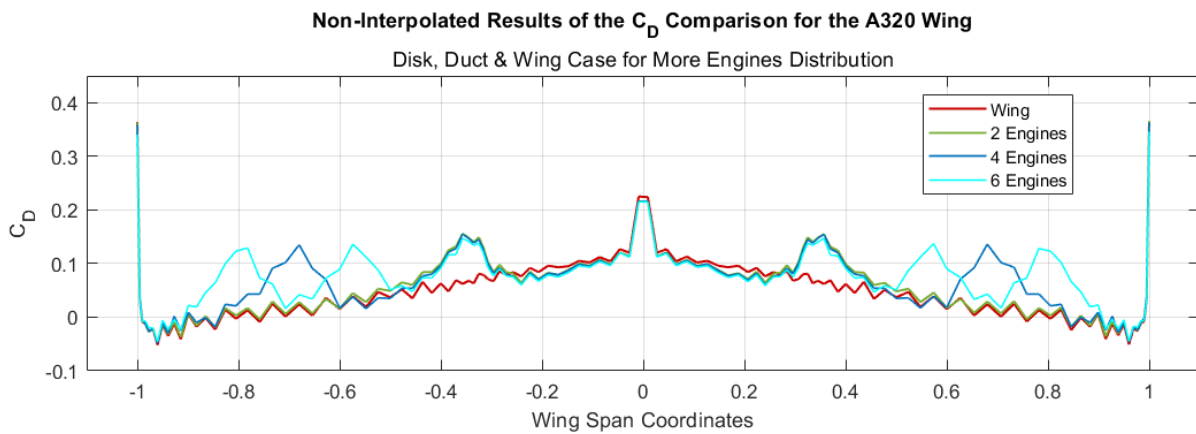


Figure A.11 Graphical representation of the non-interpolated drag coefficient results of the More Engines distributions for the disks, ducts & wing case.

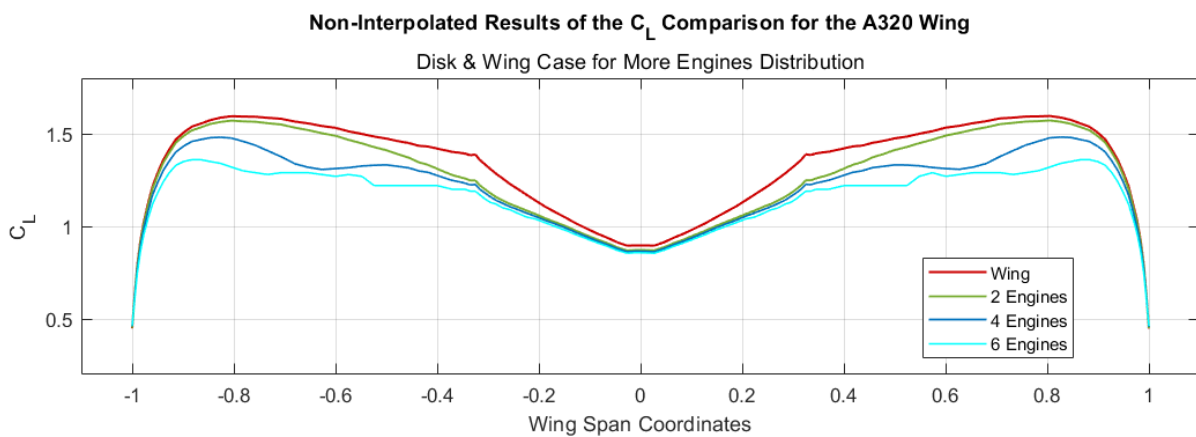


Figure A.12 Graphical representation of the non-interpolated lift coefficient results of the More Engines distributions for the disks & wing case.

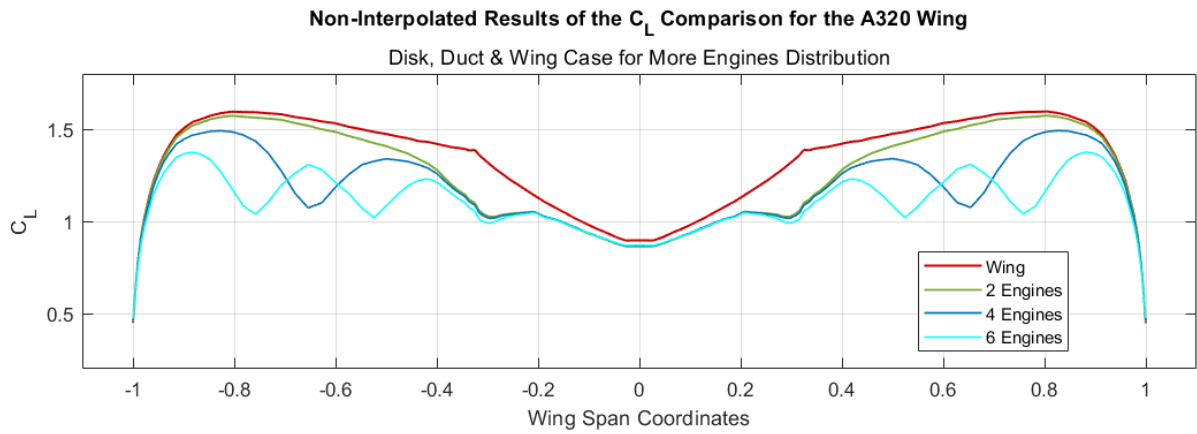


Figure A.13 Graphical representation of the non-interpolated lift coefficient results of the More Engines distributions for the disks, ducts & wing case.

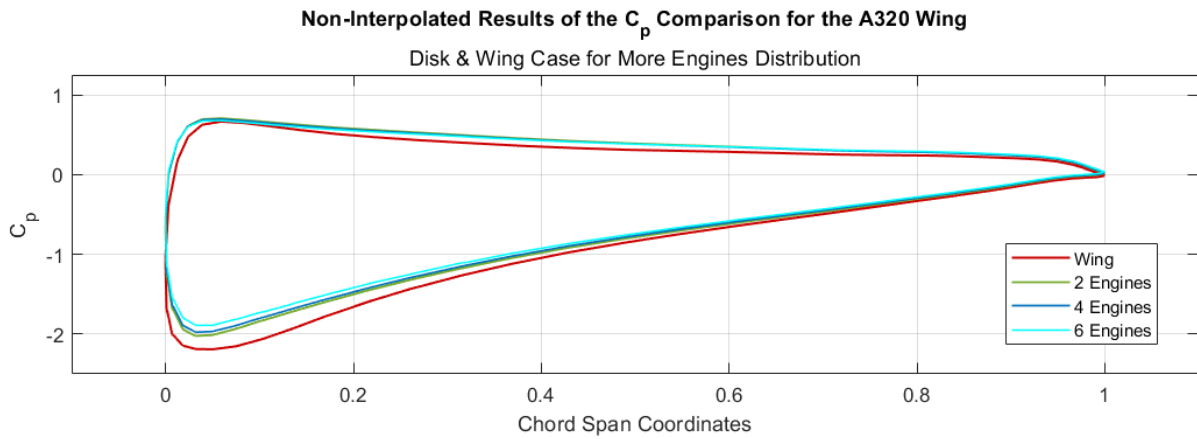


Figure A.14 Graphical representation of the non-interpolated pressure coefficient results of the More Engines distributions for the disks & wing case.

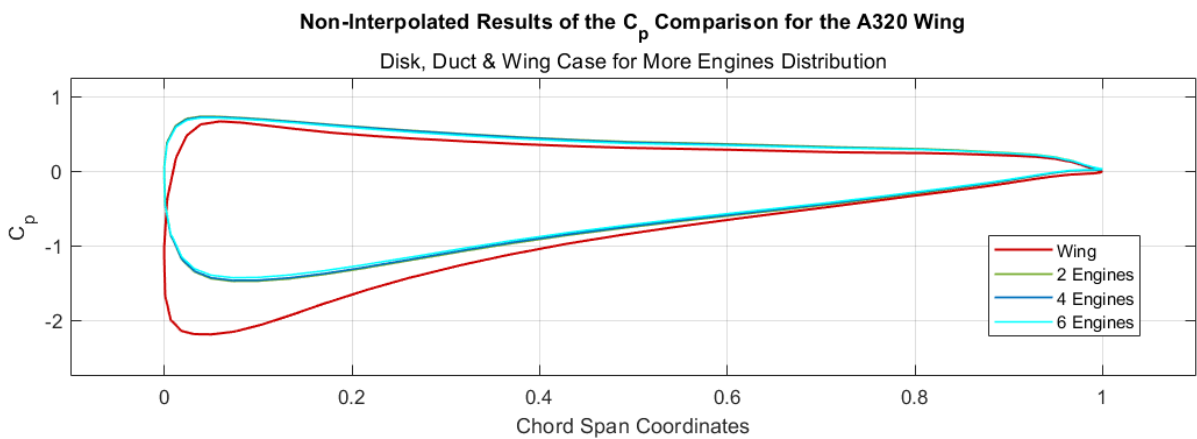


Figure A.15 Graphical representation of the non-interpolated pressure coefficient results of the More Engines distributions for the disks, ducts & wing case.

Tip Engines

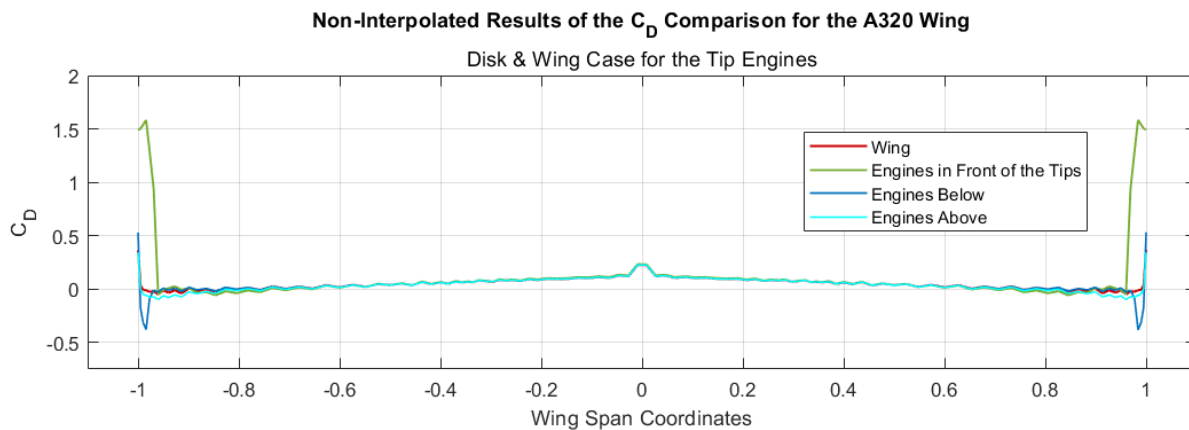


Figure A.16 Graphical representation of the non-interpolated drag coefficient results of the Tip Engines distributions for the disks & wing case.

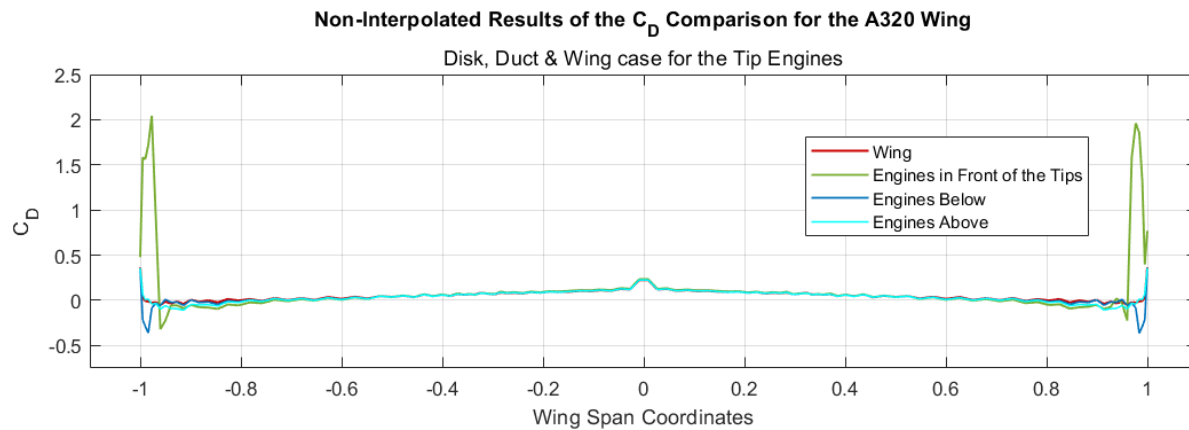


Figure A.17 Graphical representation of the non-interpolated drag coefficient results of the Tip Engines distributions for the disks, ducts & wing case.

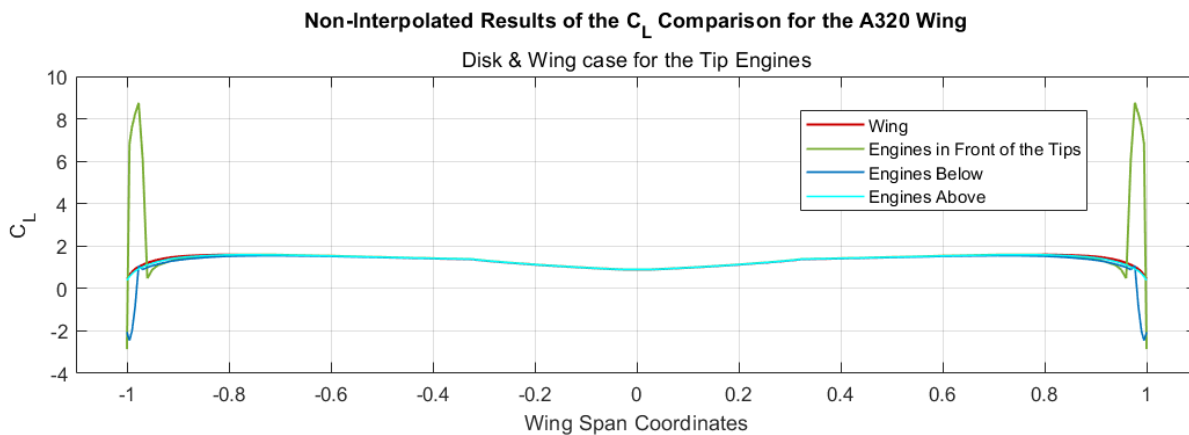


Figure A.18 Graphical representation of the non-interpolated lift coefficient results of the Tip Engines distributions for the disks & wing case.

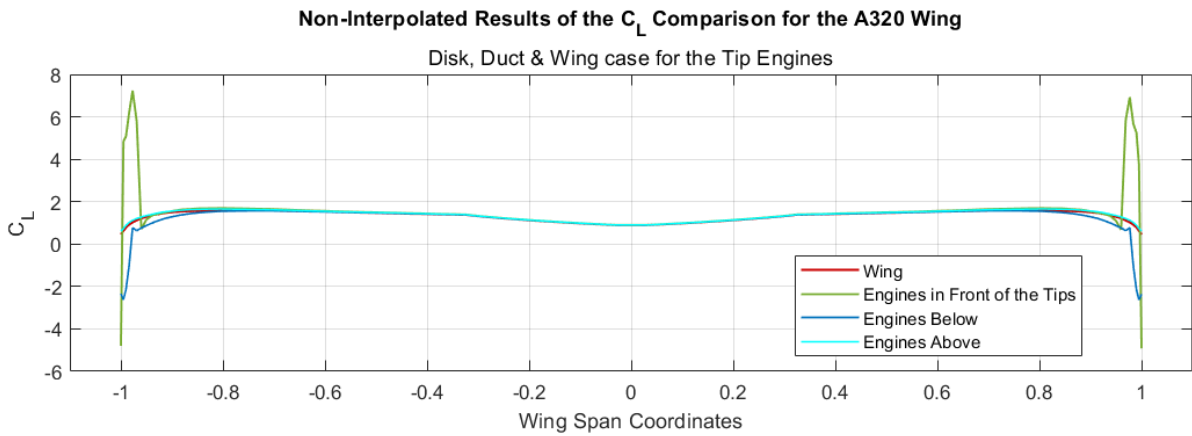


Figure A.19 Graphical representation of the non-interpolated lift coefficient results of the Tip Engines distributions for the disks, ducts & wing case.

A320

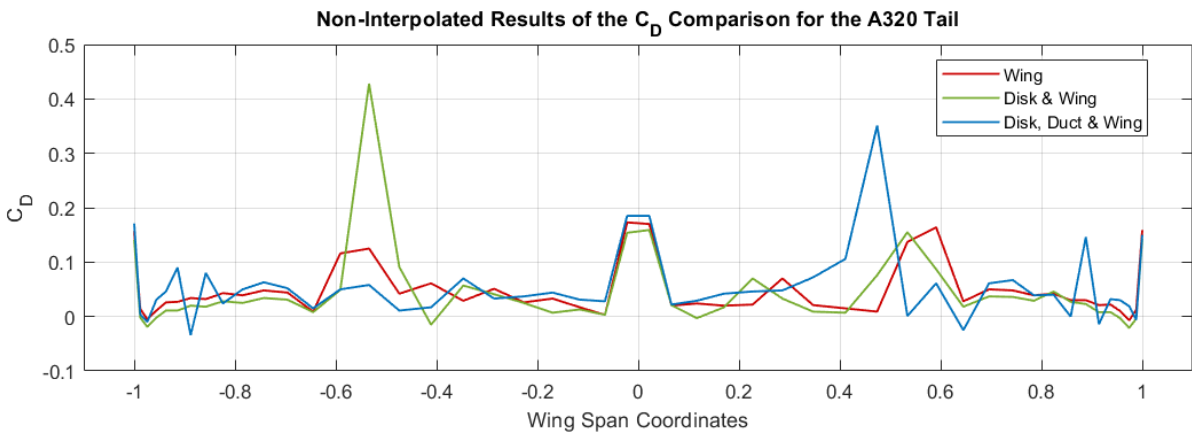


Figure A.20 Graphical representation of the non-interpolated drag coefficient results of the tail.

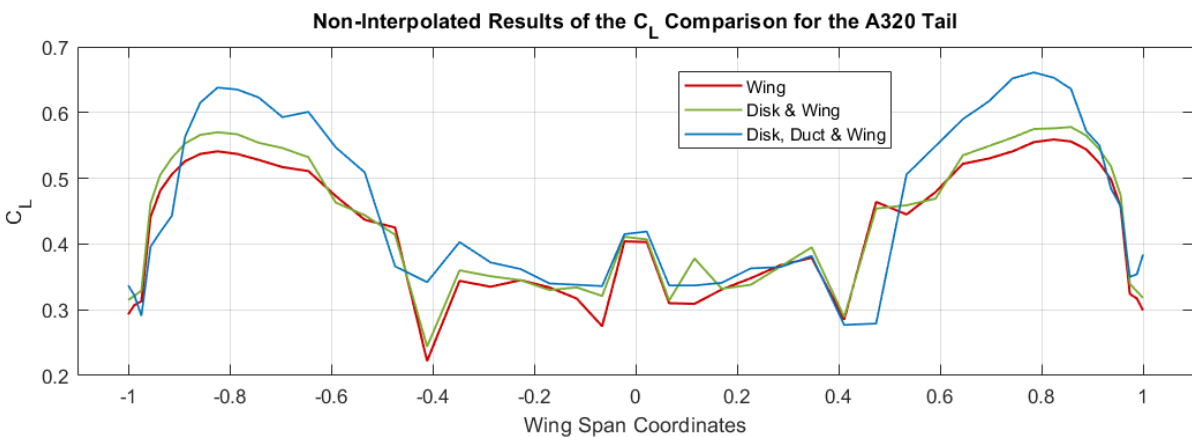


Figure A.21 Graphical representation of the non-interpolated lift coefficient results of the tail.

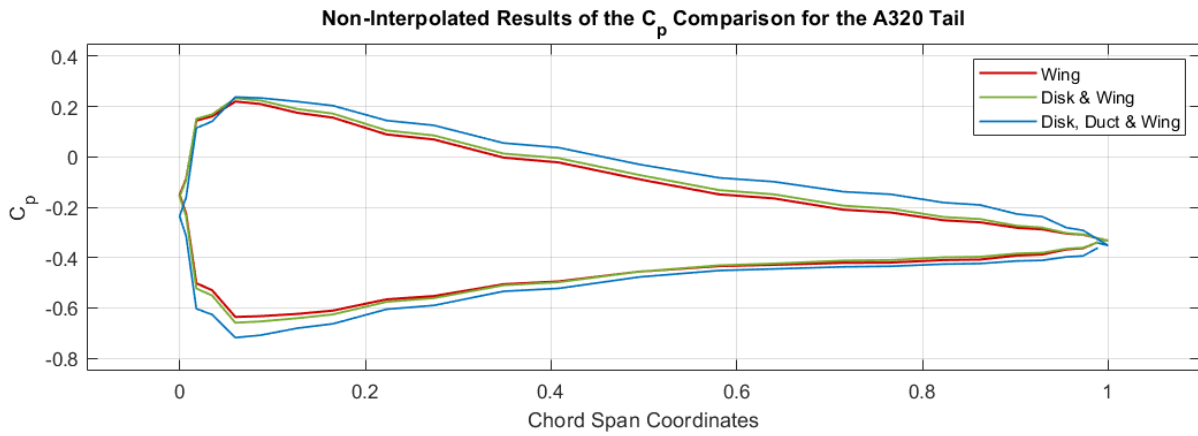


Figure A.22 Graphical representation of the non-interpolated pressure coefficient results of the tail.

Best Distribution - Wing Results

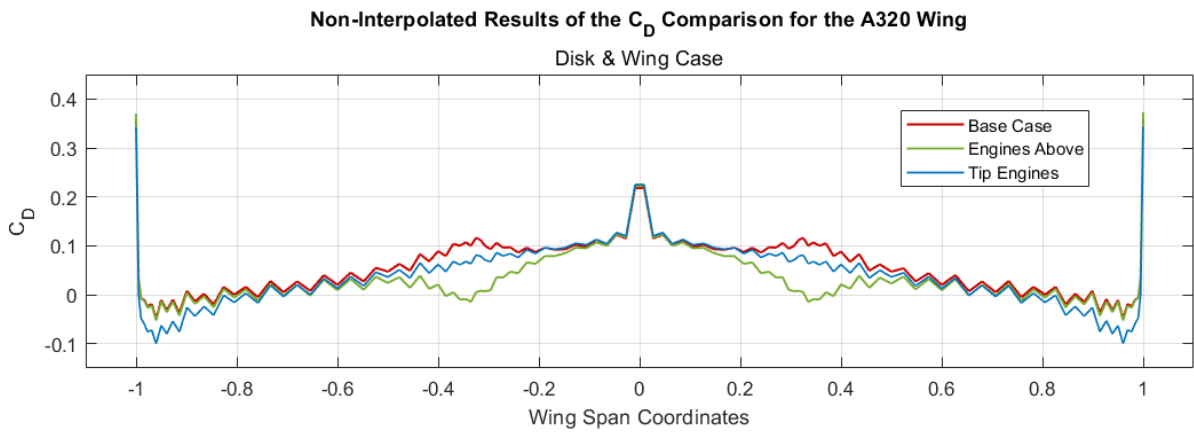


Figure A.23 Graphical representation of the non-interpolated drag coefficient wing results of the Best Results for the disks & wing case.

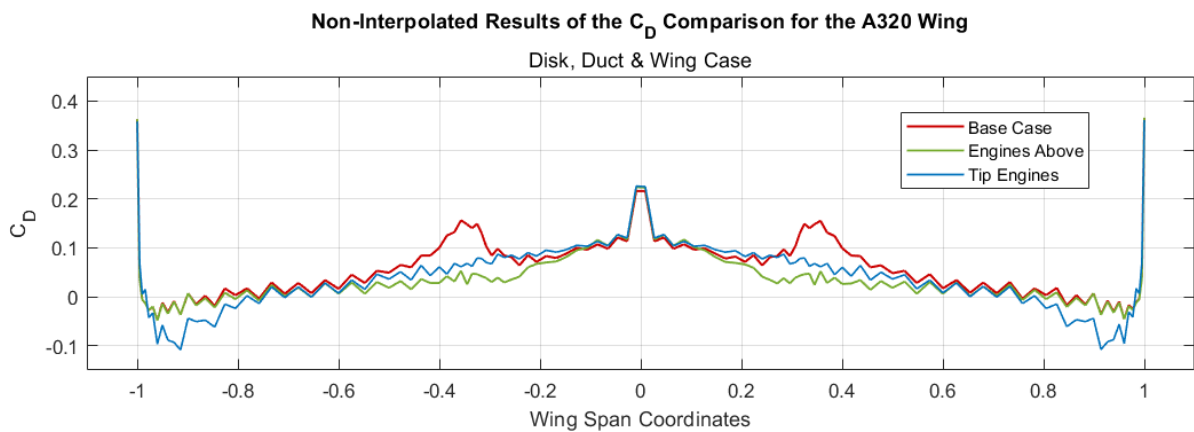


Figure A.24 Graphical representation of the non-interpolated drag coefficient wing results of the Best Results for the disks, ducts & wing case.

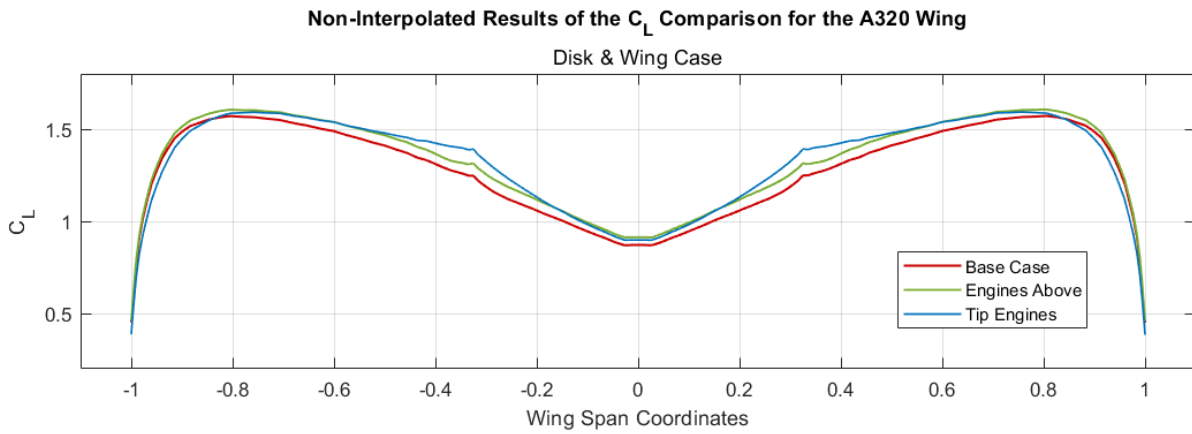


Figure A.25 Graphical representation of the non-interpolated lift coefficient wing results of the Best Results for the disks & wing case.

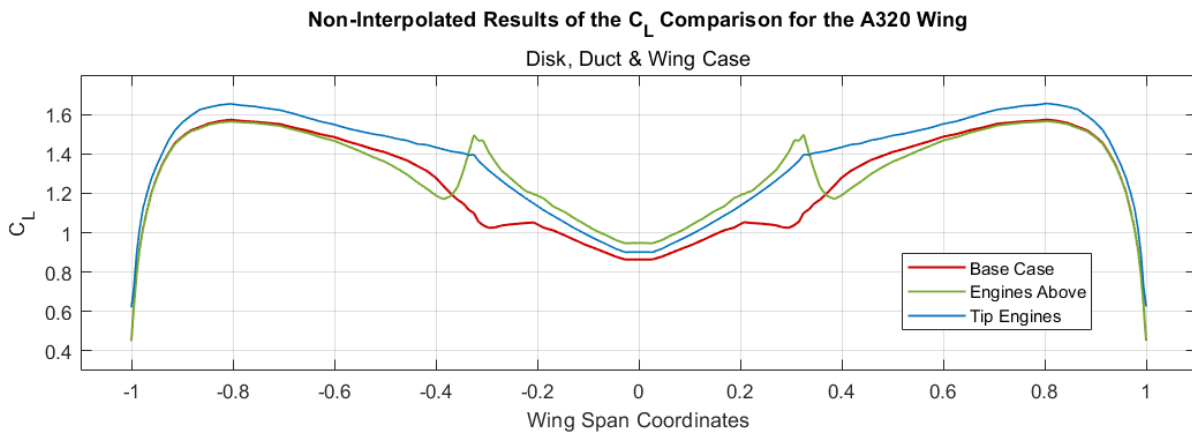


Figure A.26 Graphical representation of the non-interpolated lift coefficient wing results of the Best Results for the disks, ducts & wing case.

Best Distribution - Tail Results

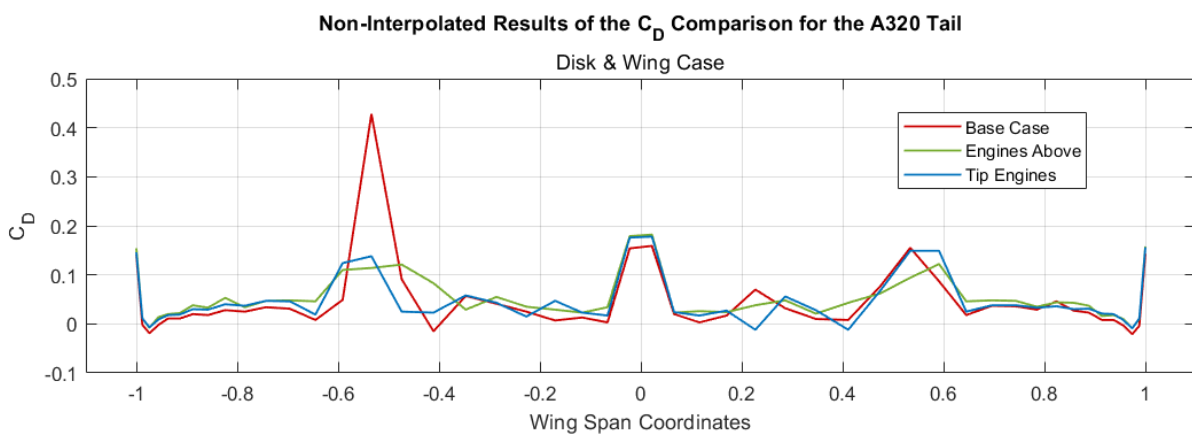


Figure A.27 Graphical representation of the non-interpolated drag coefficient tail results of the Best Results for the disks & wing case.

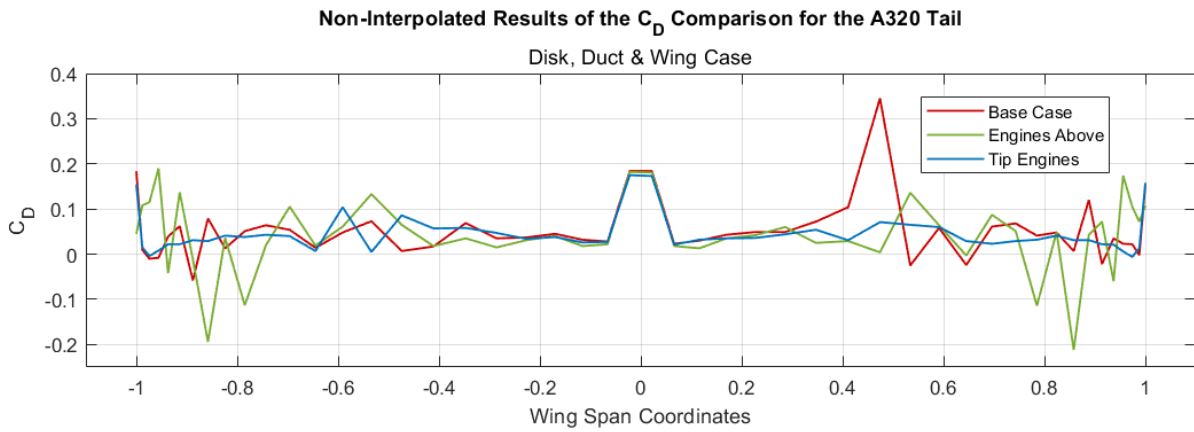


Figure A.28 Graphical representation of the non-interpolated drag coefficient tail results of the Best Results for the disks, ducts & wing case.

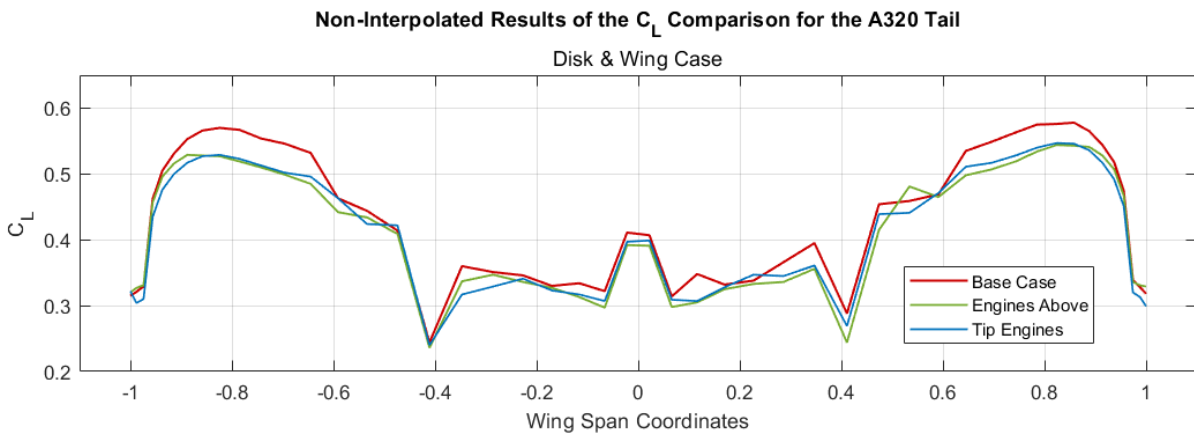


Figure A.29 Graphical representation of the non-interpolated lift coefficient tail results of the Best Results for the disks & wing case.

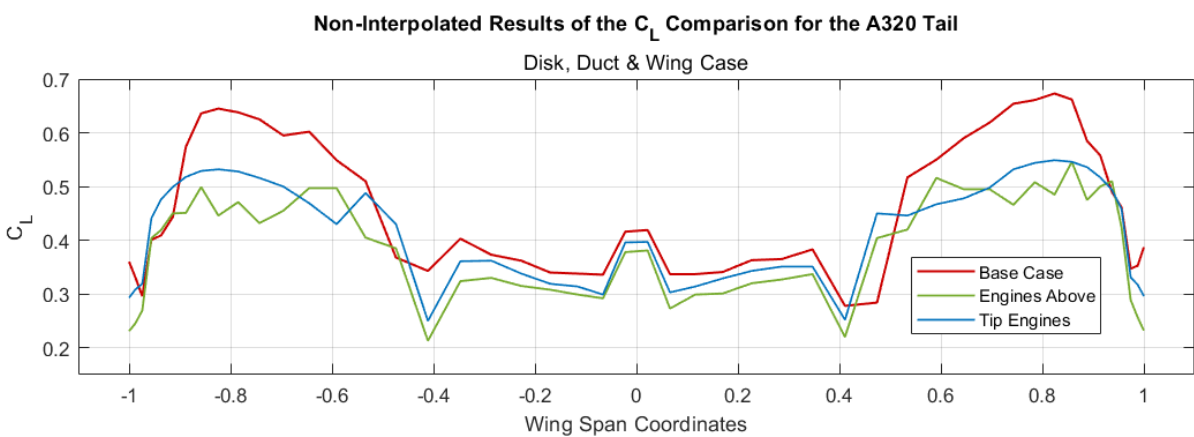


Figure A.30 Graphical representation of the non-interpolated lift coefficient tail results of the Best Results for the disks, ducts & wing case.

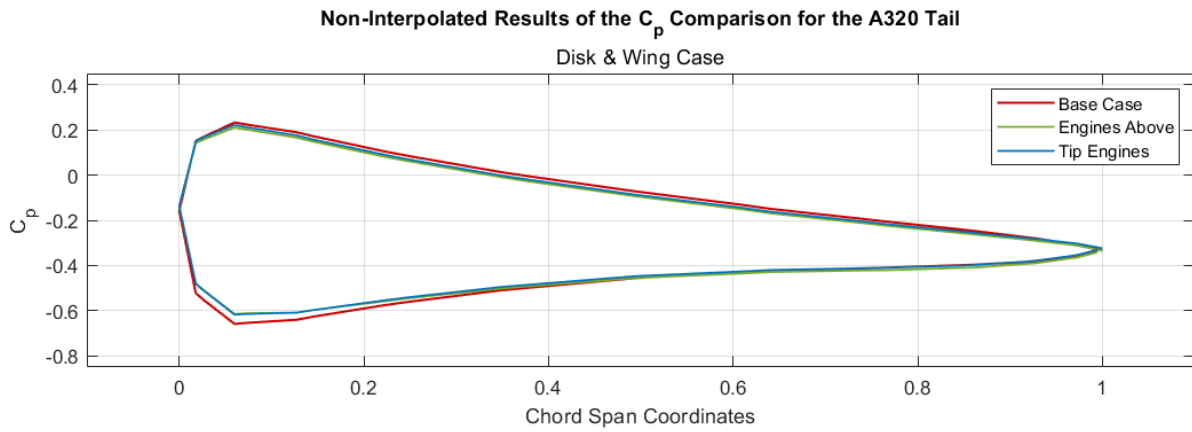


Figure A.31 Graphical representation of the non-interpolated pressure coefficient tail results of the Best Results for the disks & wing case.

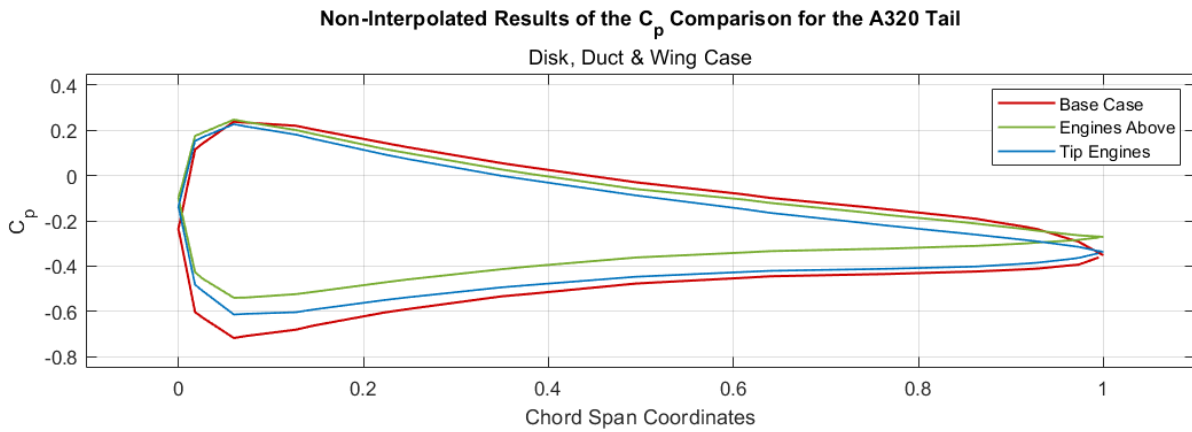


Figure A.32 Graphical representation of the non-interpolated pressure coefficient tail results of the Best Results for the disks, ducts & wing case.